Biophysical Characterization of Protein-Protein Interactions with Mass Photometry



Fabian Soltermann

Lincoln College

University of Oxford

A thesis submitted for the degree of

Doctor of Philosophy in Physical and Theoretical Chemistry

4th November, 2020

Acknowledgements

Three exciting years in Oxford were an amazing time thanks to the many wonderful, supportive, and inspiring people who accompanied me on this journey. Thank you to all of you.

The people I am indebted the most I would like to thank specifically.

First and foremost, I thank Carol and Philipp. Carol, for giving me the great opportunity to come to Oxford and become part of her group, for her endless and kind support and for guiding my development as scientist. Philipp for making it possible to get involved in his exciting research, for his inspiring guidance and support, and his amazing BBQs. The three years in his lab fundamentally changed my view on proteins and made me feel like having gotten access to a new dimension of the world.

A great thank you goes to Weston for working closely together with me for 3 years, for teaching me a lot about biology, antibodies, and viruses and for his "can-do" attitude. This enabled many things, including joining the ASMS conference in San Diego (a life-long memory) in my first year of PhD, with a last-minute abstract jointly written during the night, after a long night out. I would also like to thank Joe, Idi and Di for their advice and support in science and non-science questions, Gavin for teaching me how mass photometry works and both PK and CVR groups for shared interest in exciting research.

Thank you to the drinking, board gaming and sports buddies in the Robinson, Benesch, Baldwin and Kukura Group for making the lab a great place to be, especially Daniel, Denis, Dom, Francesco, Leo, Shane and Joe.

Beyond the lab life, Oxford had to offer a seemingly endless source of unique and bustling events. I am very grateful that I got the chance to experience this and thank the Berrow Foundation and the Lord Florey Scholarship for offering me a place here in Oxford. Furthermore, I thank the Lincoln College, its rector Prof. Henry Woudhuysen FBA and the Lincoln College community for a warm welcome in Oxford and an amazing three years in this college. A special thanks to my Lincoln drinking buddies, housemates and rowing squad (especially Nick, Caspar, Sofie, Nicolas, Chen, Ben, James, Marcel) for great friendship.

I also thank all the committee members of the Oxford University Swiss Society, who I was fortunate to work with during my presidency of the society. I am grateful for their hard work and commitment next to their degree, which made it possible to hold a series of unique events, including hosting the president of the Swiss Confederation, Alain Berset.

Back in Switzerland, I am very grateful to call Domi, Römi, Dimi, Kröbel, Chregu, Boki, Monti and Klenke my best mates. I thank them for putting in a lot of effort to keep our friendship intact, including visiting me in Oxford several times and always making time in when I am back home.

I also present my sincere thankfulness to my family, Mami, Papi, Stefan, Yves, Andrea and their partners for being a solid base to always come back to and my goddaughter, Emilie for her heart-warming welcomes in Oberkulm.

Finally, I express my deepest gratitude to Siyun for standing by me in any situation, always offering support, encouragement, and new perspectives. Thank you for the time we have spent and for the years to come.

Statement of Originality

The research described in this thesis was carried out by the author between October 2017 and October 2020 and includes nothing which is the outcome of work done in collaboration, except where specifically indicated in the text. The use of the first person plural is strictly a matter of style in keeping with standard scientific convention.

List of Publications

The work carried out by the author between October 2017 and October 2020 led to the following publications:

1. F. Soltermann, E. D. B. Foley, V. Pagnoni, M. Galpin, J. L. P. Benesch, P. Kukura and W. B. Struwe, Quantifying Protein–Protein Interactions by Molecular Counting with Mass Photometry, *Angewandte Chemie International Edition*, 2020, **59**, 10774-10779.

2. H. C. Tjondro, J. Ugonotti, R. Kawahara, S. Chatterjee, I. Loke, S.Chen, F. Soltermann, H. Hinneburg, B. L. Parker, V. Venkatakrishnan, R. Dieckmann, O. C. Grant, J. Bylund, A. Rodger, R. J. Woods, A. Karlsson-Bengtsson, W. B. Struwe, M. Thaysen-Andersen, Hyper-Truncated Glycans Augment the Activity of Neutrophil Granule Myeloperoxidase, *Journal of Biological Chemistry*, 2020, reviewed.

3. F. Soltermann, W. B. Struwe, P. Kukura, Biophysical Optical Methods for Label-free Quantification of Protein-protein Interactions, *Physical Chemistry Chemical Physics*, in preparation.

4. F. Soltermann, S. Chen, P. Kukura, W. B. Struwe, Quantifying the Effect of Assembly and Glycosylation of HIV-1 Env on Broadly Neutralising Antibody Binding at the Single-Molecule Level, in preparation.

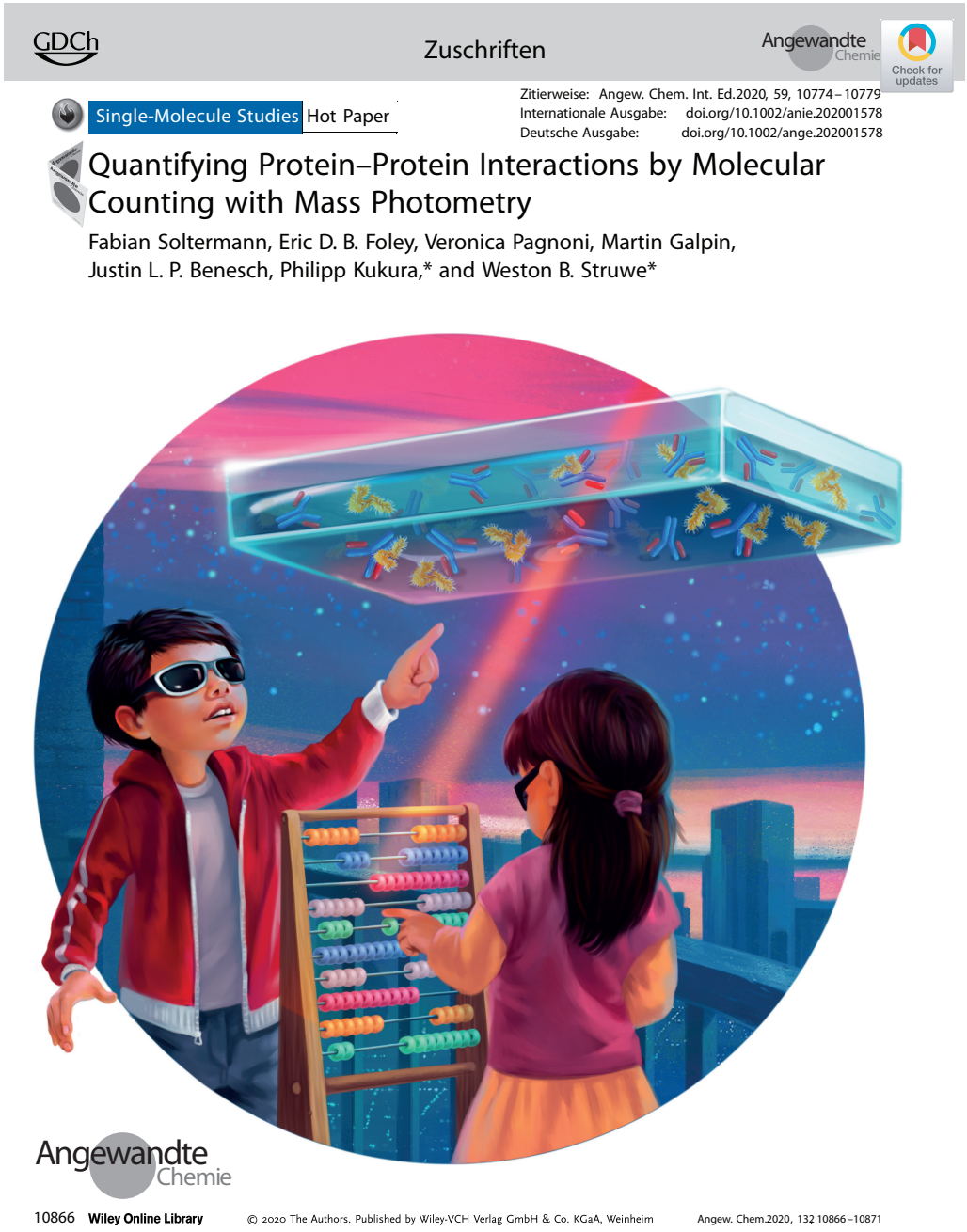


Figure 1: Cover illustration Angewandte Chemie. Like these two kids we continue to be amazed by new discoveries and exploring the unknown with mass photometry. Published with "F. Soltermann, E. D. B. Foley, V. Pagnoni, M. Galpin, J. L. P. Benesch, P. Kukura and W. B. Struwe, Quantifying Protein–Protein Interactions by Molecular Counting with Mass Photometry, *Angewandte Chemie International Edition*, 2020, **59**, 10774-10779."

Abstract

Interactions between biomolecules control the processes of life in health and their malfunction in disease, making their characterization and quantification essential. We first explore the capabilities of established methods for binding affinity measurements of protein-protein interactions and present mass photometry in this context. We explain that immobilization- and label-free analytical techniques are desirable because of their simplicity and minimal invasiveness, but that they struggle with quantifying tight interactions and resolving co-existing species.

After a bench-marking process we show that mass photometry can accurately count different unlabelled biomolecules at the single-molecule level, distinguishing them by molecular mass, thereby revealing the relative abundances of different oliogomeric states and stoichiometries of complexes *in vitro*. We develop and characterize a single-shot measurement method to determine binding affinities over four orders of magnitude at equilibrium for both simple and complex stoichiometries, as well as the associated kinetics in experiments with minimal sample consumption (fmol) and efficient experimental procedures ($<$ few minutes per sample).

We then present applications of this method for protein-protein interactions quantification of biotherapeutics and glycoproteins in the field of cancer, autoimmune disease, HIV and SARS-CoV-2 research.

These results introduce mass photometry as a rapid, simple and label-free method for studying sub-μM binding affinities, with potential to become a universal approach for characterizing wide range of biomolecular interactions.

Contents

List of Figures **v**

List of Abbreviations **ix**

1 Introduction **1**

2 Theoretical Background and Overview **5**

2.1 Biophysical Optical Methods for Quantification of Protein-protein Interactions *In-vitro* 5

2.1.1 Introduction 5

2.1.2 Immobilization-based Methods 10

2.1.3 Separation-based Methods 19

2.1.4 Solution-based Methods 28

2.1.5 Conclusion and Summary 40

2.2 Mass Photometry 41

2.2.1 Principle 41

2.2.2 History and Prior Work 51

2.2.3 Open Questions 59

2.3 Quantitative Analysis of Protein-Protein Interactions 60

2.3.1 Thermodynamics and Kinetics of Protein-Protein Interactions in Solution 61

3 Development of MP Based Biophysical Characterization Methods 67

3.1 Introduction 67

3.2 Results and Discussion 69

3.2.1 Stoichiometry and Relative Abundances 69

3.2.2 Working at sub-μM Concentrations 77

3.2.3 Data Quality Control 79

3.2.4 Binding Affinity and Kinetic Measurements 81

3.3 Summary and Outlook 91

3.4 Methods 92

3.4.1 Synopsis 92

3.4.2 Materials and Sample Preparation 93

3.4.3 MP Data Acquisition 97

3.4.4 Data Analysis 99

3.4.5 Non-specific Adsorption: Challenges and Solutions . . . 103

3.4.6 Surface Plasmon Resonance 106

3.4.7 Native Mass Spectrometry 106

3.4.8 Equations 107

4 Investigating protein-protein interactions in HIV with MP 113

4.1 Introduction 113

4.2 Results and Discussion 117

4.3 Conclusion and Outlook 131

4.4 Methods 132

4.4.1 Sample preparation 132

4.4.2 MP experiments 132

5 Characterization of Glycoproteins and their Interactions by MP **135**

5.1 Introduction 135

5.2 Results and Discussion 139

5.3 Conclusion and Outlook 148

5.4 Methods 149

5.4.1 Materials 149

5.4.2 Native Mass Spectrometry 150

5.4.3 Mass photometry 151

6 Glycoprotein Interactions in SARS-CoV-2 **153**

6.1 Introduction 154

6.2 Results and Discussion 157

6.3 Summary and Outlook 165

6.4 Methods 167

6.4.1 Materials 167

6.4.2 Mass photometry 167

7 Summary and Outlook **169**

References **177**

List of Figures

1 Cover illustration Angewandte Chemie. 8

2.1 Overview of optical methods for protein-protein interaction quantification *in-vitro*. 8

2.2 Immobilization-based methods for PPI quantification. 11

2.3 Experimental data of surface plasmon resonance. 13

2.4 Experimental data of bio-layer interferometry. 15

2.5 Experimental data of SwitchSense. 19

2.6 Separation-based methods for PPI quantification. 20

2.7 Experimental data of capillary electrophoresis. 23

2.8 Experimental data of analytical ultracentrifugation. 25

2.9 Experimental data of SEC-MALS. 28

2.10 Solution-based methods for PPI quantification. 29

2.11 Experimental data of CG-MALS. 31

2.12 Experimental data of microscale thermophoresis. 33

2.13 Experimental data of microfluidic diffusional sizing. 35

2.14 Mass photometry for PPI quantification. 37

2.15 Experimental data of mass photometry. 38

2.16 Signal detection in interferometric scattering microscopy. . . . 42

2.17 Architecture of an iSCAT microscope for mass photometry. . . 43

2.18 Ratiometric iSCAT imaging of single proteins. 46

2.19 Principle of single-molecule landing detection. 47

2.20 Characterization of mass accuracy, precision, and dependence on molecular shape and identity. 49
2.21 One-dimensional distributions of refractive index and specific volume for different proteins. 50
2.22 Principle of single-molecule counting by mass photometry. . . . 51
2.23 Schematic of dark-field microscopy of GNPs. 53
2.24 Schematic of interferometric scattering experiment. 54
2.25 Interferometric scattering microscopy of myosin. 55
2.26 Label-free single-molecule imaging with iSCAT. 57
2.27 Concept of mass photometry (MP). 59

3.1 Principle of single-molecule counting by mass photometry. . . 70
3.2 Data analysis approaches for 2G12 monomer/dimer ratios using gaskets. 73
3.3 Dynamic range estimation, sample carriers and diffusion correction. 76
3.4 Non-specific adsorption and sample tube passivation. 78
3.5 Screening method for the quantification of impurities, stoichiometry, binding affinities and kinetics of protein-protein interactions with MP. 82
3.6 Single-shot K_d of IgG-FcγRIa interactions. 82
3.7 K_d screening of deglycosylated IgG-FcγRIa. 83
3.8 K_d screening of IgG-FcγIa complexes. 85
3.9 Screening of trastuzumab-HER2 interaction. 86
3.10 Principle of dissociation and association measurements. 87
3.11 Kinetic measurements of FcγRIa binding to intact and deglycosylated IgG. 88
3.12 Correlation of published K_d vs k_{off} values. 89
3.13 Schematic of interactions in MP and SPR. 89

3.14 Binding stoichiometry and affinity of the IgG-FcRn interaction as a function of pH. 90
3.15 Size exclusion chromatography of 2G12. 94
3.16 SDS-PAGE of SEC purified 2G12. 95
3.17 Native mass spectrometry of 2G12 and contrast calibration. . 100
3.18 Assignment of FcγRIa molecular mass. 101
3.19 Native MS experiments to confirm IgG deglycosylation. 107

4.1 Structure, conformational dynamics and epitope targeting on HIV Env trimers. 115
4.2 Fraction selection of SOSIP SEC-purification. 118
4.3 Screening of gp120 interaction with glycan targeting bnAbs. . 119
4.4 Control experiments of gp120 interaction with Env targeting bnAbs. 122
4.5 Screening of SOSIP interaction with glycan targeting bnAbs. . 124
4.6 Screening of SOSIP interaction with Env targeting bnAbs. . . . 127
4.7 Screening of bsAb interaction with gp120-WT and Her2. . . . 130

5.1 Glycoprotein overview. 137
5.2 Glycoprotein molecular weight of MP vs. native MS. 140
5.3 Comparison of glycoprotein mass measurements with MP, native MS and literature. 142
5.4 Influence of glycosylation on t-PA oligomeric states. 143
5.5 Interaction study of etanercept and TNF-α. 146
5.6 MP analysis of neutrophil granule myeloperoxidase. 148

6.1 Overview of PPI studies in SARS-CoV-2 host cell entry by MP. 155
6.2 MP analysis of mACE2 and ACE2. 157
6.3 MP analysis of RBD interaction with mACE2 and ACE2. . . . 159

6.4 MP analysis of S1 protein interaction with mACE2 and ACE2. . 161

6.5 MP analysis of S protein interaction with mACE2 and ACE2. 163

List of Abbreviations

Acronyms

K_{d}	Dissociation Constant
k_{off}	Dissociation Rate Constant
k_{on}	Association Rate Constant
Ab	Antibody
AOD	Acoustic-Optical-Deflector
bnAb	Broadly Neutralizing Antibody
BSA	Bovine Serum Albumin
bsAb	Bispecific Antibody
CMOS	Complementary Metal Oxide Semiconductor
Env	Viral Spike Envelope Glycoprotein
FOV	Field of View
HIV	Human Immunodeficiency Virus
iSCAT	Interferometric Scattering Microscopy
ITC	Isothermal Calorimetry
mAb	Monoclonal Antibody
MP	Mass Photometry
MPER	Membrane Proximal External Region
MW	Molecular Weight
PDF	Probability Density Function
PPI	Protein-Protein Interaction

PSF	Point Spread Function
SEC	Size-Exclusion-Chromatography
SNR	Signal-to-Noise-Ratio
SPR	Surface Plasmon Resonance

Chapter 1

Introduction

The complexity and multifaceted nature of proteins and their interactions make them an incredibly exciting field to work in. Generations of scientists have been dedicating their creativity and careers to tackle the seemingly endless flow of questions and opportunities coming from this class of molecules.

Its source can be dated back to the summer of 1838 when Jöns Jacob Berzelius coined the term "protein" in a letter to his colleague Gerardus Johannes Mulder to describe a new class of substances.[1] With the modified Greek word "proteios", which means primary, they described their findings that these compounds seem to build the primitive and principal basis of nutrition and animals. Amazingly, we still strongly associate terms like diet, muscles and health to the word "protein".

Since the 1840s we made advances in understanding why these molecules are so essential for us and how they achieve their function. Proteins can be seen as long chains of covalently bound amino acids. These specific amino acid sequences and the involved intra- and intermolecular forces lead to the formation of structures which can execute functions with high specificity and precision. The correct folding and assembly of these structures is essential for the functionality of the protein. With their presence in virtually every cellular process, proteins are responsible for both health and disease. Probably the most

famous example is the human protein haemoglobin. With its four sub-units and tightly associated iron-ions via haem groups, it serves as an oxygen transporter in our blood. Its structure and function show that proteins are often composed of several non-covalently bound parts and operate in a dynamic environment. This often requires ability to perform reversible processes and interact with many other species, similar to haemoglobin's uptake and release of oxygen in different cellular compartments, such as lungs and muscles.

Given the vital role of proteins in our body it seems sensible that about 80 % of all proteins do not operate independently but in cooperation with other proteins and substances.[2] Therefore, proteins have to be seen as being part of a complex network of interactions, where changes of one part can induce a cascade of changes in another part of the network. Identifying and understanding the individual protein interactions helps to break down the problem into more manageable pieces and to understand these complex mechanisms.

A general approach has been to first identify interacting proteins in their native environment, the living cell, i.e. *in vivo*. After interaction partners are identified, the proteins are recombinantly expressed in order to produce them in large quantities, isolate and transfer them from a living cell into a test tube, i.e. *in vitro*. *In vitro* biophysical characterization techniques can then be used to confirm binding and to determine and understand the extent with which the protein is interacting with other molecules.

Although there has been a revolution in available biophysical characterization techniques and data analysis over the past 3 decades, many important shortcomings still exist. With existing gold-standard techniques the general user experiences limitations such as high sample consumption, long measurement times, low throughput and complicated experimental procedures and data analysis. Furthermore, most techniques cannot resolve co-existing species and

lack the sensitivity to quantify tight interactions. This often limits the broad applicability to 1:1 interactions and prevents quantification of tight interactions such as antibody-antigen complexes. Some of the techniques also require immobilization or labelling of analytes, which alters the measured interactions.

Overcoming these challenges and limitations is essential to accelerate and improve research in the life sciences. Ultimately, this will contribute to higher success rates in drug development in pharmaceutical research and therefore impact the lives of people around the globe.

Recent advances in single-molecule microscopy lead to the development of a particularly promising technique for the biophysical characterization of biomolecules. The technique, termed mass photometry, is based on interferometric light scattering microscopy and allows for *in vitro*, label-free detection of single biomolecules.[3,4]

In this work we explore the suitability of mass photometry to address the challenges faced in biophysical characterization of protein interactions. We describe the method development and present the resulting applications. Specifically, we show how to measure aggregation, purity, stoichiometry, binding affinity and kinetics of protein complexes. Applications focus on protein interaction measurements of biotherapeutical proteins and glycoproteins in cancer, autoimmune disease, HIV and SARS-CoV-2 research and highlight the relevance of this method for drug development.

Chapter 2 introduces the reader to biophysical characterization of protein-protein interactions. We also give the historical and theoretical background of mass photometry and explain the thermodynamic and kinetic parameters in protein interaction measurements.

In Chapter 3 we describe the mass photometry method development for characterizing protein-protein interactions in detail. We show at the example of

monoclonal antibodies and receptors how mass photometry can measure purity, stoichiometry, binding affinity and kinetics of these interactions. Additionally, we draw the reader's attention to potential pitfalls and good mass photometry practice.

Chapter 4 looks at applications in HIV research and shows that a mass photometry assay based on broadly neutralizing antibodies can be used to probe various epitopes on HIV-1 Env with high specificity, revealing different structures and states of the Env protein. Ultimately, this will help to get further insight into the host-cell entry mechanisms of HIV.

In Chapter 5, we extend the application to a breadth of examples related to glycoproteins. Specifically, we benchmark mass photometry of glycoproteins and combine it with glycosidase digests to identify glycoproteins and determine types of glycans. Moreover, we look at the impact of glycosylation on the affinity of protein-protein interactions.

In Chapter 6, we combine the herein learned lessons to contribute to COVID-19 research, Specifically, we look at protein interactions present during host-cell entry of SARS-Cov-2.

Chapter 7 summarizes the contents of this thesis and provides an outlook on mass photometry, expected technical developments and impact on future research.

Chapter 2

Theoretical Background and Overview

2.1 Biophysical Optical Methods for Quantification of Protein-protein Interactions *In-vitro*

2.1.1 Introduction

The subject of this literature review is the comparison of widely applied optical methods for *in-vitro* measurements of affinities and kinetics of protein-protein interactions. We aim to provide a comprehensive overview and comparison of the techniques and their principles. We also discuss advantages, limitations, and recent applications of each method.

In this process we review surface plasmon resonance (SPR), bio-layer interferometry (BLI), analytical ultracentrifugation (AUC), capillary electrophoresis (CE), size-exclusion-chromatography multi-angle-light-scattering (SEC-MALS), composition-gradient multi-angle-light-scattering (CG-MALS) and present emerging methods, such as SwitchSense, microscale thermophoresis and microfluidic diffusional sizing.

Finally, we present mass photometry (MP) through a few recently published applications and highlight its potential as an universal tool for studying protein-

protein interactions and dynamics with minute sample consumption (<pmol) in a rapid and label-free fashion.

Before a protein-protein interaction can be analyzed in-depth with biophysical methods the putative binding partners have to be identified. This often involves *in-vivo* screening, i.e. in the living cell, for example when looking for potential tumor suppressors or oncogenes in cancer research.[5] With these methods it is believed that 30–60% false positive and 40–80% false negatives must be expected. Therefore, it is important to increase reliability by using a combination of several techniques.[2]

For the initial *in-vivo* screening the introduction of affinity tags and two-hybrid screens are two commonly used methods to capture multi-protein complexes. With advances in mass spectrometry instrumentation, quantitative proteomics and native mass spectrometry became valuable tools to increase sensitivity of detection protocols.

In the case of affinity-tag methods, the protein of interest is expressed with a genetically fused sequence with specific affinity to another compound. Common affinity tags are His6 with affinity to Nickel in Ni-NTA resins or protein A columns for IgGs. During purification, the tagged protein (bait), together with bound proteins, is captured with ligands linked to a solid support. After washing of all non-interacting proteins from the cell lysate, the bait protein with its bound proteins is eluted and identified by mass spectrometry. Although this method allows for high throughput, it is often biased towards interactions with high affinities and slow kinetics.

More laborious, but more reliable are two-hybrid screens, e.g. yeast two-hybrid system.[6] In this method, Protein 1 is fused to a DNA-binding domain and protein 2 to a transcription activation domain. Proteins binding to each other induce a detectable expression of a reporter gene.[5]

Identified binding partners are then often recombinantly expressed in order to obtain sufficient sample for an in-depth characterization of the protein and its interaction. In this process, purity, integrity, and activity are iteratively checked with methods including chromatography (e.g. SEC), SDS-PAGE or ELISA.

Performing the biophysical characterization *in-vitro* helps to reduce complexity, increase throughput and simplify interpretation of data. Typical experiments include testing different mutations, ligands or conditions.

To determine if and to what extent a protein is interacting with the identified binding partners, a range of biophysical characterization methods can be applied.[5] In Figure 2.1 we show an overview of commonly used opitcal methods, including immobilization-based methods (SPR, BLI and SwitchSense), separation-based methods (CE, AUC and SEC-MALS) and solution-based methods (MST, MDS, CG-MALS and MP). Other methods, such as native mass spectrometry or isothermal calorimetry are beyond the scope of this review and are discussed elsewhere.[7,8]

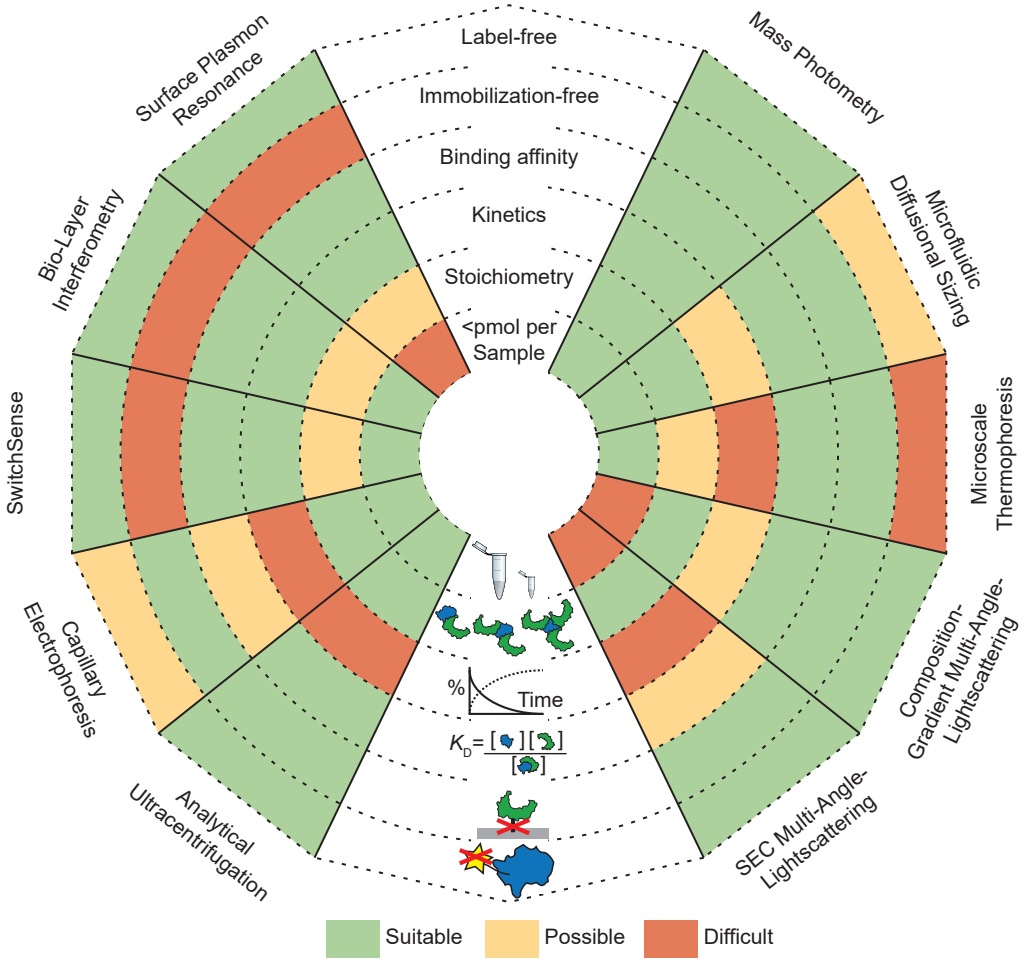


Figure 2.1: Overview of optical methods for protein-protein interaction quantification *in-vitro*. SPR, BLI, SwitchSense, CE, AUC, SEC-MALS, CG-MALS, MST, MDS and MP are discussed (anti-clockwise from to left to top right). Each "ray" of the spider-diagram represents one method and is divided into a selection of criteria (label-free, immobilization-free, binding affinity, kinetics, stoichiometry, $< pmole$ per sample). The method's performance for each criterion are compared by a color code. This code indicates to which degree a method fulfils a criterion (suitable (green), possible (yellow) and difficult (orange)).

In this figure, we look at a selection of criteria and compare performance of each method by using a color code (green: method fulfils criterion/is suitable for this experiment, yellow: method partially fulfills criterion, i.e. is suitable for this experiment with constraints, orange: method does not fulfil criterion, i.e. challenging to use in this experiment).

Label-free and immobilization-free techniques are highly sought after, be-

cause labelling or immobilizing analytes/ligands alter the measured binding interaction and require an additional step in the experimental procedure.

Although quantifying binding affinities can be perceived as a trivial task, it can be challenging in the case of protein-protein interactions, especially when it goes beyond simple yes/no answers. Weak interactions are difficult because they usually have fast off-rates, can easily fall apart and require high concentrations to contain a detectable amount of complex. In contrast, strong interactions (sub-μM) require high sensitivity to quantify the low abundance of unbound species or need to be able to measure at concentrations around the K_{d} value, e.g, nM or pM.

In many cases, kinetics measurements can be seen as the advanced version of binding affinity measurements because abundance of bound and unbound species have to be quantified at different time points. Here, the temporal resolution limits the accessible on- and off-rates, which can cover time scales from milli-seconds to hours or even days. Following reactions with high sensitivity over a long time is demanding because noise and baselines must be reproducible or at least subtractable.

An additional layer of complexity is added when working with multi-valent or oligomeric proteins, i.e. molecules which have more than one binding site. Here, bound and unbound states can consist of complexes with different stoichiometries. Interpretatation of this binding data often requires fitting procedures where different binding models are compared to the experimental data to deduce the stoichiometry.

A parameter that is often underestimated, but important to consider when selecting a method, is the required amount of sample to perform the experiment. This can often be the limiting factor and encouraged the development of miniaturized or chip-based methods working at sub-μM concentrations with

only μl of sample. Having standardized or even automated protocols helps to make sample consumption and success-rate of an experiment more predictable.

Beyond the above discussed criteria, the versatility of the method (e.g. applicability to different classes of biomolecules, buffers or complex samples such as cell-lysates), automation of measurements and data analysis as well as high throughput are further factors to consider when selecting a method.

Solving a complex biological question requires careful selection of the method and a good understanding of its strengths and limitations. Below, we aim to discuss the performance of each method under these points of view and explain the principles, advantages, limitations and recent applications, starting with immobilization-based methods (SPR, BLI and SwitchSense).

2.1.2 Immobilization-based Methods

Surface Plasmon Resonance

SPR has seen an incredible growth since its commercialization by Biacore (Uppsala, Sweden) in the 1990s.[9–11] Its importance as a biosensor is evident from the number of publications featuring "surface plasmon resonance" and "protein-protein interaction" (>10'000, advanced search Google Scholar, 2020). The all optical-based method quantifies in real-time and label-free protein-ligand affinities and kinetics.[2,12]

In a SPR instrument the ligand is immobilized to a sensor surface, usually a thin gold layer on a glass support (Figure 2.2a). The sensor surface is then illuminated with polarized light in an angle that generates total internal reflection, known as the SPR angle. Small changes in the refractive index of the sensor surface (e.g. by molecules which are binding to the surface) will affect the SPR angle and the detected light intensity.

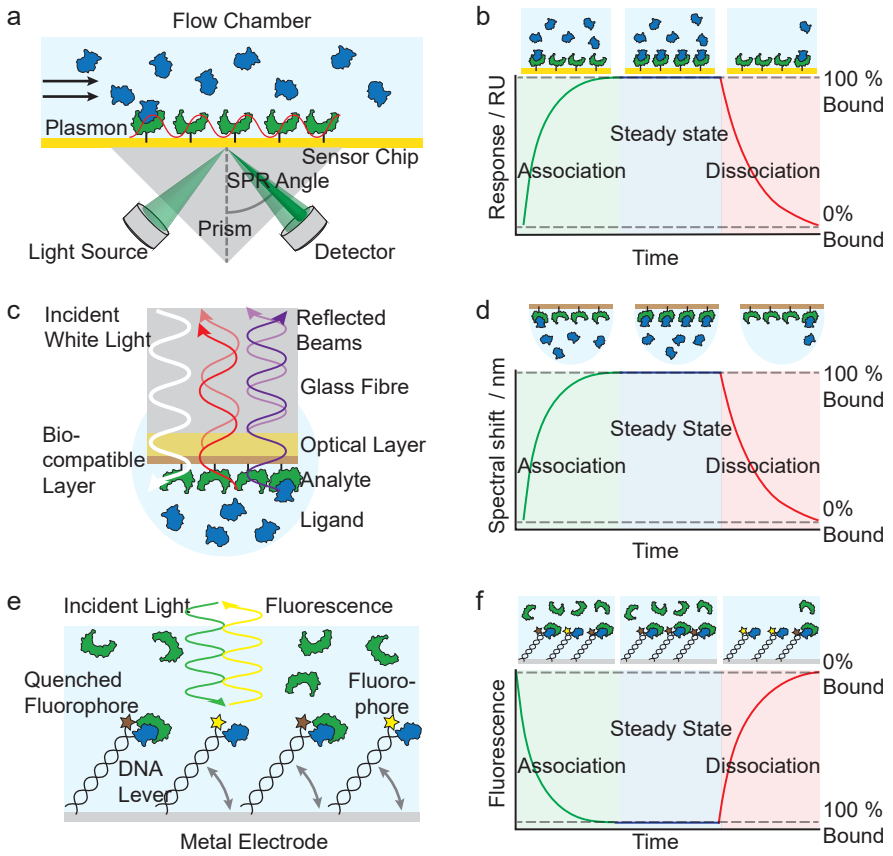


Figure 2.2: Immobilization-based methods for PPI quantification. Principles of surface plasmon resonance (a, b), bio-layer interferometry (c, d) and SwitchSense (e, f) are shown. Analyte (green) or ligand (blue) are immobilized onto a surface and then exposed to a solution containing ligand or analyte of known concentration. The formation of complex can then be followed overtime to extract on- and off-rates of interactions as well as the binding affinity and stoichiometry.

The SPR based biosensor instrument records this signal change in response units (RU). The RUs are directly proportional to the mass of analyte binding to the ligand on the sensor surface. Combined with the absolute concentration of molecules in solution, the RUs and their time-dependence are a measure for the binding affinity and kinetics of the interaction.

In a typical experiment the immobilized ligand is exposed to a continuous flow of analyte to measure the association reaction, in terms of RU (Figure 2.2b). Once the signal is constant, all binding sites on the surface are occupied, and the analyte solution is replaced by blank buffer. From here, the dissociation

reaction is followed. Fitting the binding curves, based on the Langmuir theory, provides k_{on} and k_{off} and consequently also the K_{d}. Measurements beyond 1:1 interactions are less straight forward to analyze for the inexperienced user.

However, the large dynamic range for K_{d} measurements (sub-nM to low mM) and small sample amounts (several μg per sensor chip)[13] combined with little sample requirements make it broadly applicable. Experimental conditions are compatible with various buffers, although care should be taken when using detergents, chelating or denaturing agents. Measurements are fully automated and require only minimal sample preparation.

Despite the high degree of automation, it remains low throughput because several runs are needed and occupy the instrument for several hours. Further limiting factors are the requirement of immobilization of ligand to the sensor surface which is expected to alter the measured binding affinities[13], mass transport effects, which limit the upper limit of accessible kinetic processes ($k_{\mathrm{off}} < 10^{-1}$ s^{-1}) and sensitivity to non-specific interactions between sensor surface and analyte.[14]

These limitations are clearly outweighed by its user-friendliness and broad applicability which is evident from more than 1000 publications featuring topics related to SPR and PPI in 2019 and 2020. Given the large number of publications, we refer here to reviews showcasing recent developments in SPR applications for protein-protein interaction quantification[15–17], including high-throughput developments on SPR imaging sensors (SPRi)[18], sensitivity and detection speed[19,20], influence of capture surfaces[21], as well as overcoming challenges with multi-valent binding.[22,23]

In the review of Mamer et al. they show SPR's convergence to cell-based protein-protein interaction measurements.[24] Recent research focusing on SARS-CoV-2 protein interactions highlights the applicability of SPR, as shown in

Figure 2.3, where Wrapp et al. quantify the binding affinity of the SARS-CoV-2 spike protein binding to ACE2.[25]

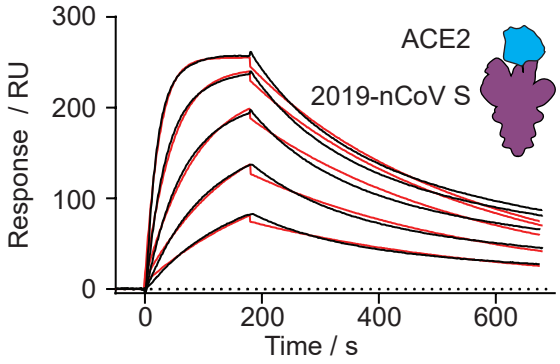


Figure 2.3: Experimental data of surface plasmon resonance. Binding of ACE2 (blue) to immobilized SARS-CoV-2 S protein (violet) is measured, with experimental data in black and fit in red. SPR shows binding kinetics for human ACE2 and immobilized S protein with k_{off}= 2.76 x 10^{-3} s^{-1} and k_{on}= 1.88 x 10^{5} M^{-1} s^{-1}. This results in a K_{d} of 14.7 nM. Adapted from reference 3 with permission from AAAS.

In general, SPR is often used as the final method to quantify binding affinities, after biophysical characterization (e.g. purity, stoichiometry, aggregation) of involved proteins by complementary techniques, such as mass spectrometry, AUC, SEC-MALS[26,27] and many others.

Future work is directed towards making SPR based biosensing with high sensitivity, specificity and high-throughput even more applicable in a wide range of biomedical research.

Bio-layer Interferometry

Bio-layer interferometry (BLI) is an efficient tool to characterize molecular interactions between various classes of biomolecules and is often seen as the high-throughput alternative to SPR. Commercially introduced 15 years ago by Fortebio (Fremont, US) its application as biosensor technology has rapidly increased, allowing for determination of kinetic rate constants and binding affinities of molecular interactions in real-time and label-free.[28]

It is similar to SPR in the sense that it requires immobilization of a ligand on a sensor surface to which binding of analyte is detected with an all-optical method (Figure 2.2c). In BLI white light is directed through an optical fiber to a biocompatible layer on the fiber surface. Once ligand molecules are immobilized on this biolayer, the fiber becomes a probe which can be dipped into analyte solution.

Binding of analyte changes the refractive index of the biocompatible layer, which is measured as change in interference pattern and proportional to the amount of bound analyte. The interference arises from the small path difference between light back reflected from the fiber surface/biolayer interface and the biolayer/solution interface.[29]

In contrast to SPR, where the binding surface is exposed to a continuous flow, the BLI sensor tip is dipped in static solutions for each binding step. The use of orbital agitation of the sample holder at high speed ensures sufficient mixing to avoid re-binding of dissociated analyte to the immobilized ligands. With this, association and dissociation of analyte and binding partner can be followed over time to extract k_{on} and k_{off} (Figure 2.2d). In this way, binding affinities in the range of 10 pM to 1 mM are accessible. In many cases a 1:1 interaction model is applied to fit the model to experimental data.[30,31]

Given that experiments can be performed in micro well plates, no maintenance intensive microfluidics are needed and setups can be combined with disposable sensor tips which enables coupling to 96- or even 384-well high-throughput formats.[32,33] However, the advantage of higher-throughput comes with inferior reproducibility and lower sensitivity to low MW analytes, and cross-validation with SPR is generally recommended.[32]

Similar to SPR, limitations such as mass transfer and immobilization effects remain.[28] These immobilization effects have also been addressed in the work

of Kamat et al. for their binding kinetic assay to quantify antigen-antibody interactions.[34] Advances in data analysis should further help to go beyond the often assumed 1:1 interaction models.[35,36]

Among recent applications since 2019 are several studies focusing on SARS-CoV and MERS-CoV interactions. In Figure 2.4 Yi et al. use BLI to compare binding affinities of human ACE2 to the receptor binding domain (RBD) of SARS-CoV-2 and determine on- and off-rates as well as K_ds for a 1:1 binding model.[37]

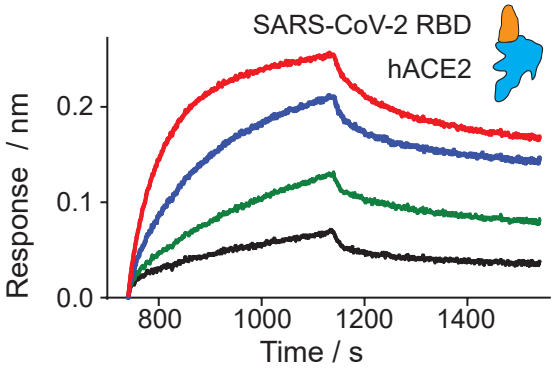


Figure 2.4: Experimental data of bio-layer interferometry. BLI binding profiles of the SARS-CoV-2 RBD (orange) to the soluble hACE2 receptor (blue), measured on an Octet RED96 instrument at different concentrations (1.85 nM (black), 5.56 nM (green), 16.67 nM (blue), 50 nM (red)). Binding kinetics were evaluated with a 1:1 Langmuir binding model by ForteBio Data Analsyis 9.0 software and yielded k_{on}=2.65 x 10^5 M^{-1} s^{-1} k_{off}=1.35 x 10^{-3} s^{-1} and K_d= 5.1 nM. Adapted from[37] with permission from Springer Nature.

In similar studies, BLI is used to look at the spike glycoprotein (HIV-1, SARS-CoV-2, MERS-CoV) and its binding to receptors and antibodies[25,38–42], including antibody competition assays for humoral protection.[43,44] BLI has also been used to quantify cross-reactivity of antibodies for Nipah virus (NiV) and Hendra virus (HeV), against which no vaccines or licensed therapeutics exist yet.[45] In the work of Li et al. they made use of the concentration dependent on-rates of antigens binding to immobilized antibodies to quantify antigen levels in a high-throughput manner in CHO cell line development and compared

sensitivity and throughput to standard assay formats, such as ELISA.[46] A similar approach was used by Wallner et al. to quantify glycosylation of Fc-glycosylated IgGs via immobilized lectins as measure for product quality.[47] Loomis and Steward-Jones et al. used BLI for evaluation of antigenicty of their candidate vaccines in structure-based design of Nipha virus vaccines.[48]

In summary, BLI is used as standard tool for binding affinity and kinetics measurements of protein-protein interactions and is increasingly applied as complementary method to SPR, while offering lower reproducibility, but higher throughput.

SwitchSense

SwitchSense is similar to BLI and SPR in that it uses immobilized ligands on a surface to capture analyte molecules. The label-free detection of proteins with SwitchSense is based on ligands immobilized to fluorescently labeled DNA oligonucleotides attached to a gold surface. Upon binding of analyte to the ligand, the fluoresence signal is quenched and serve as a measure for binding affinity and kinetics.[49] The SwitchSense technique has emerged within the past 10 years and was commercialized by Dynamic Biosensors GmbH, Germany. With this technique not only typical protein interactions parameters, i.e. affinity, kinetics can be obtained, but also additional information such as size, shape, bending, flexibility and elasticity of the protein complexes, at quantities of less than 10^{-18} mol on the sensor surface.[49,50]

In more detail, a fluorescent marker (e.g. Cy3 dye) is attached to a double-stranded DNA oligonucleotide which is tethered to a gold surface (Figure 2.2e). A ligand (e.g. antigen) is then immobilized at the solution-exposed end of the DNA tether, in proximity to the fluorescent marker. Binding of analyte to the ligand quenches the fluorescence and is detected as fluorescence signal change. Exposing the immobilized ligand to a continuous flow of analyte solution leads

to a continuous decrease of fluorescence intensity (association curve) until a steady-state is reached, where all ligand molecules are saturated and the fluoresecence signal reaches its minimum (Figure 2.2F). Switching to a blank buffer solution leads to dissociation of analytes until the initial fluoerscence signal is restored. Fitting of kinetic models to the experimental data yields on- and off-rates as well as binding affinities.

Beside binding affinity and kinetic measurements, experiments can be configured to use the DNA tether as a sensitive indicator for size, shape, bending, flexibility and elasticity of the protein complexes.[49] More specifically, the switching between horizontal to vertical conformation of the negatively charged DNA tether can be induced by alternating electric fields (a few 100 mV in the kHz range, with spatial extension of only a few nanometers). These fields are applied to the gold surface covered with a low-density ds DNA monolayer. In the "standing" position fluorescence is detectable, whereas it is quenched in the "lying" conformation by nonradiative energy transfer from the dye to surface plasmons in the gold surface. The type of charged polymer (e.g. DNA), the grafting density, as well as composition and ionic strength of buffer solution play an important role in the switching behavior. As mentioned before, variable parameters such as charge, size, shape, conformation, bending flexibility, internal elasticity alter the switching behavior.[51] Together with changes in fluorescence properties due to proximity of marker and bait protein, they influence the fluorescence signal.[50] These contributions must be carefully dissected when interpreting the signal. For further discussion of the experiments we refer to the work of Rant et. al..[50]

Moreover, we highlight that SwitchSense can also be used for interactions involving small-molecules, or DNA/RNA interactions, but do not further discuss it herein.[52,53]

Focusing on PPIs, early binding affinity experiments, in 2009, by Rant et al.[49], demonstrated that they can clearly detect changes in the switching amplitudes when exposing immobilized sheep IgG to a protein G solution. In a control experiment, no changes where observed when exposing goat Fab2, which lacks the Fc region, to a protein G sample. They also showed that the sensitivity was sufficient to work in the low fM concentration range with sample quantities of bound protein as little as 0.3 amol, compared to a minimum of 20 amol for SPR.[49]

A recently reported measurement of binding affinities and kinetics of protein-protein interactions was performed in 2017 by Franz-Oberdorf et al.[54] They looked at interactions of strawberry fruit allergens (Fra a 1.01E, Fra a 1.02 and Fra a 1.03) with a putative binding partner FaAP, which they identified with the help of yeast 2-hybrid screen and sequence matching. With their interaction study they could confirm the putative binding and revealed nM affinities for all systems, with rate constants varying by 2 orders of magnitude.

In 2018, Crowe et al. applied SwitchSense in the preclinical development of a novel, orally-administered anti-TNF-α domain antibody for the treatment of inflammatory bowel disease. Their antibody candidate, V565, and the clinical comparator antibody adalimumab showed both picomolar affinity for human sTNF-α.[55]

In a further study by Daub et al. in 2020, the stability of intrinsic multivalent complexes formed by TNFα-trimers bound to TNFα-scavengers (IgGs and Fab fragments) was investigated (Figure 2.5).[56]

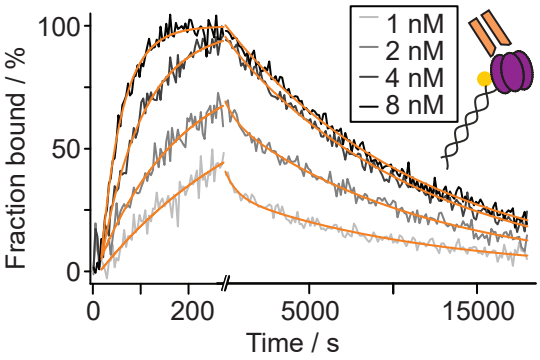


Figure 2.5: Experimental data of SwitchSense. TNF-α (violet)-Adalimumab Fab (orange) interaction. Interaction was recorded in reversed assay orientation (immobilized TNF-α). Solutions of Adalimumab Fab diluted in running buffer (1, 2, 4, 8 nM) were injected for 260 s (association), followed by injection of running buffer for 18,000 s (dissociation). Solid light grey to black lines represent normalized data. Solid orange lines represent global fit data. Kinetic rates and affinities were as follows: k_{on}= 2.82 x 10^6 M^{-1} s^{-1}, k_{off}= 8.52 x 10^{-5} s^{-1} and K_d= 30.2 pM. Adapted from[56] with permission from Springer Nature.

They used SwitchSense to determine binding affinities and kinetics of the complexes and provided insight into the kinetics of the monomer-trimer equilibrium of TNF-α. Their real-time assessment of monomerization could help to better TNF-α's bioactivity and its role in regulation inflammation.

These experiments show that SwitchSense is able to provide comparable insights to SPR and BLI. Although still young, it offers new avenues to accelerate these measurements because it is chip-based, and could be parallelized and adapted to high-throughput microarrays.[51]

2.1.3 Separation-based Methods

Capillary Electrophoresis

Capillary electrophoresis separates molecules based on differences in their electrophoretic mobility and quantifies relative abundances with optical detectors. A microfluidic version of CE (MCE) is commercialized for interaction screenings as LabChip instrument by PerkinElmer.[57] CE is a powerful screening tool in

drug discovery because of minimal sample consumption (nanoliters or less) and low sample requirements, as well as ease of automation, high through-put and fast measurement times (below 1 s were achieved).[57,58]

In more detail, CE separates proteins based on differences in migration velocity in a separation channel under an applied electric field (Figure 2.6a).The electrophoretic mobility is dependent on charge and size, which allows for separation based on either property.

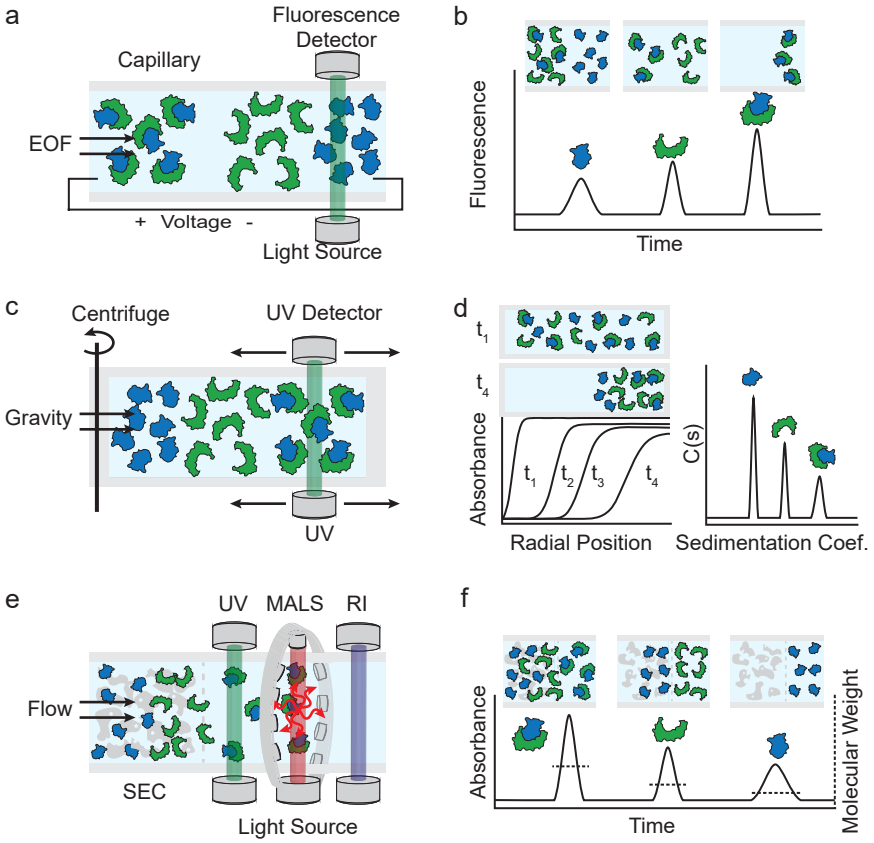


Figure 2.6: Separation-based methods for PPI quantification. Principles of capillary electrophoresis (a, b), analytical ultracentrifugation (c, d) and size-exclusion-chromatography multi-angle-light-scattering (e, f) are shown. Analyte (green), ligand (blue) and complex are separated while total concentration is monitored with UV or fluorescence. In MALS a refractive index detector and multi-angle-light-scattering detector are added to determine the average molecular weight of species present in solution. The abundance of unbound and bound species can be either determined directly from the peak areas or via modelling and deconvolution of peak shapes.

CE is highly sensitive to changes in buffer composition, as this changes the electroosmotic flow and electrophoretic mobility of the protein. Eluted proteins are typically detected online with mass spectrometry or optical methods such as UV absorbance or laser-induced fluorescence.[59] The more sensitive fluorescence detection may be required because of low concentrations or thin channel diameters of microfluidic devices.[60]

In the context of PPI measurements CE has mostly been applied to yes/no questions, i.e. does an interaction occur or not, using presence or absence of peaks in the elution profile as an indicator (Figure 2.6b). The simplicity of this approach is ideal for large scale inhibition assays with small molecule drugs.

Binding affinities for PPI were also quantified, such as in Rauch et al. where the binding affinity of labeled Hsp70 to Bag3 for a 1:1 binding model a K_{d} of 23 $\pm$ 8 nM was determined.[61] Comparison to SPR and ITC measurements showed excellent agreement. They also showed in a competition experiment that addition of unlabeled Hsp70 leads to a decrease of the complex and resulted in an IC50 of 0.24 μM, which highlights its suitability as an inhibition assay.

Earlier examples include K_{d} determination for Gc-globulin G-actin, lectin glycoprotein and antibody antigen interactions.[62,63] Various antibody-antigen binding affinities and stoichiometries have been investigated by CE-methods and upon comparison with standard methods shown to be accurate and precise.[20,58] A good summary thereof can be found in the review of Moser et al..[58]

In another example, Lassen et al.[64] could not determine a valid binding constant of the C4-mAb interaction and attributed this to various reasons, such as C4 adsorbance to the inner wall of the capillary, which decreased electroendosmotic flow at high C4-concentrations as well as the multi-valency of the interaction.

Besides the general limitation of protein adsorption to the inner wall of

the capillary[57,65,66], the difficulty of maintaining protein complexes while still allowing separation with sufficient resolution poses a major limitation.[65] It was shown that this can be addressed with protein cross-linking. Cross-linked proteins can be exposed to harsher conditions and longer separation times, while still maintaining the initial interaction.

Ouimet et al. used protein cross-linking electrophoresis (PXCE) to determine the K_{d} of various interactions, which were all in agreement with other methods, e.g. lysozyme-antilysozyme (24 ± 3 nM, compared to 17 ± 2 nM from ITC) immunocomplex, Hsp70-Bag3 heterodimer (25 ± 5 nM, compared to 23 ± 8 nM from CE), and Hsp90 homodimers (2.6 ± 0.3 nM, compared to 60 ± 12 nM).[67]

The same group further developed this method with an accelerated cross-linking method and increased throughput to 1 min per sample and showed its validity at the example of 5 PPIs.[68] For the Hsp70-HOP interaction they obtained an elution profile (Figure 2.7), which showed that they are able to separate impurities from the proteins of interest and quantify the abundance of bound and unbound states. This yielded a binding affinity of 3.8 ± 0.7 μM for the HSP70-HOP complex. With this method even low affinity interactions can be quantified and the sensitivity is sufficient for use in competition or inhibition essays.[65]

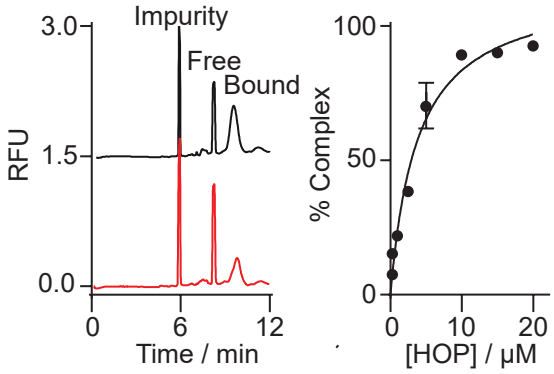


Figure 2.7: Experimental data of capillary electrophoresis. Electropherogram (left) and saturation binding curve (right) for HSP70-HOP complex by 10 s glutaraldehyde cross-linking PXCE. Saturation binding curves were fit by nonlinear regression to find a K_d= 3.8 ± 0.7 μM . The first peak in the electropherogram corresponds to a low molecular weight impurity. Adapted from[68] with permission of RSC.

Further advances were made to make CE more attractive for screening and discovery of PPI inhibitors, namely coupling of chemical cross-linking methods to CE for high-throughput screening of cell lysates[69] and coupling to 96-well plates.[61] Recent, commercially available CE systems are extended to multiple channels and can also be coupled to high throughput formats.[57] Ouimet et al. show that they can further increase throughput with a novel droplet sample introduction system which interfaces the multi-well plate and the microchip gel electrophoresis in a more efficient way, resulting in overall run time of 10 s per sample.[70] This kind of microfluidic approaches combined with high-throughput compatibility, i.e. coupling to plate readers and robotic automation will pave the way for a broader application.[71]

Although recent CE literature reporting binding affinity measurements of PPI is limited, CE's potential reportedly lies in fast yes/no answers making it a powerful method for high-throughput screening of small molecule inhibitors of PPI under physiological conditions.[70,72,73] Overall, affinity assays to screen for protein-protein interactions are still in need of further research.[57]

Analytical Ultracentrifugation

Analytical ultracentrifugation (AUC) has been around since the 1920s and experienced a renaissance in the 1990s, with the introduction of new instrumentation and major advances in data analysis.[74] In its most applied form, the sedimentation velocity experiment, it is used to quantify protein aggregation, but is also capable of accessing stoichiometries and binding affinities of protein-protein interactions.[13,75]

In AUC, the protein sample is placed in a high-speed centrifuge and exposed to a high centrifugal field upon which proteins are separated according to their molecular weight (Figure 2.6c). With UV or fluorescence detectors the spatial concentration distribution within the centrifugal cell can be measured over time.[76,77]

The obtained spectroscopy signal is a superposition of individual sedimenting species (Figure 2.6d). The temporal and spatial evolution of the concentration distribution is then fitted with numerical solutions of the Lamm equations to extract individual protein concentrations and sedimentation coefficients.[78] The sedimentation coefficients are used as a measure for molecular size. In order to achieve good fits the samples have to be extraordinarily pure (>95%).[79] With this, K_{d}s in the range of 100 nM to mM are accessible, and can be extended to the pM range with dye-labeled proteins.[80–82]

For interactions in the mM range accordingly higher concentrations are required, which increases sample consumption.[83] In exceptional cases it is possible to follow the time dependencies of interactions, but only for single kinetic rate constants in the order of 10^{-4} to 10^{-3} s^{-1}, which falls into the typical time scale of the sedimentation speed experiment.

General advantages of AUC are the large range of accessible molecular weights and the broad range of buffer conditions, such as complex formulation

buffers used in drug development.[76] However, the combination of limited molecular weight resolution and dependence on sedimentation speed is not suitable to study proteins with very similar or very different molecular weights.

Among recent applications is the work of Chaturvedi et al. in 2018 where they developed a method to quantify macromolecular interactions at high concentrations (mM) while accounting for colloidal hydrodynamic interactions and thermodynamic non-ideality.[84] In 2019, they applied their method to examine ultra-weak self-association of proteins.[85] Firstly they looked at the monomer-dimer equilibrium of hen egg lysozyme, with its well-known ionic strength-dependence (K_d=24 mM at 300 mM NaCl, $K_d > 53$ mM at 100 mM NaCl). After this bench-marking step they used their method to quantify the monomer-dimer equilibrium of chicken γS-crystallin, which yielded a K_d of 27 mM (Figure 2.8). In 2020, their work resulted in the publication of several protocols for quantitative analysis of protein self-association.[86]

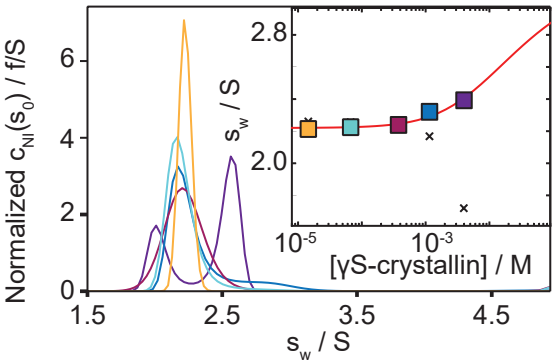


Figure 2.8: Experimental data of analytical ultracentrifugation. Sedimentation coefficient distributions $c_{NI}(s_0)$ of chicken γS-crystallin from 15 μM to 4 mM (curves in different colors for different concentrations). The inset shows weight-average sedimentation coefficient s-values as a function of concentration (circles in different colors for different concentrations) and the best-fit isotherm for a monomer-dimer self-association model (red line) resulting in an estimated K_d of 27 (16-81) mM. For comparison, the conventional analysis not accounting for non-ideality leads to weight-averaged s_w-values shown as crosses. Adapted from[85] with permission of ACS.

On the other extreme of the concentration range, recent developments in

fluorescence detected sedimentation velocity AUC enabled measurements at low pM concentrations and of pM K_ds, such as antibody-antigen interactions[80] and homo-dimerization of glutamate receptor GluA2 amino terminal domain[81]. The recent work of Zhao et al. on homo-and heterodimerization of AMPA and kainite receptor ATD shows the strength of AUC to access binding affinities over several orders of magnitude from pM to µM.[87] AUC has also been used in studies to assess binding affinities of homodimer complexes of tumor suppressor neurofibromin, which highlights AUC's important contributions to biochemical research.[88]

SEC-MALS

Light scattering techniques for protein-protein interaction measurements include static (SLS) and multi-angle (MALS) light scattering, as well as dynamic light scattering (DLS). Given the broad availability of commercial SEC-MALS systems we focus herein on applications of the MALS technique. Instruments were commercialized by Wyatt Technology, US. SEC-MALS couples UV and multi-angle-light-scattering detectors to the effluent of gel filtration columns to quantify abundance, molecular weights, stoichiometry, estimated binding affinities and aggregation of protein-protein complexes.[89–93]

Size-exclusion chromatography (SEC) allows to split the sample in its different components according to the shape/size of the molecule and reduces the complexity of the sample (Figure 2.6e). After the SEC column, the UV detector quantifies absolute concentrations and the combination of MALS and RI detectors allows for quantification of average molecular weights of biomolecules.

In MALS a monochromatic light source (e.g. laser) is directed on a sample volume, in a glass cuvette or directly within the SEC system. Detection of scattered light occurs at multiple angels and can be performed simultaneously.

The light scattering signal of macromolecules in solution is used to derive their hydrodynamic radius and molecular weight distribution.[94,95] Compared to SLS, which detects scattered light at one, fixed angle, MALS yields results with higher confidence.

In theory the averaged scattered light intensity can be calibrated against a simple reference standard (e.g. toluene). In practice a calibration with a molecular weight standard is recommended because it allows for calibration of all detectors at the same time and can be easily repeated.[89] After calibration of the UV, RI and MALS detectors and measurements at different angles a molecular weight distribution is obtained (Figure 2.6f).[96,97]

In combination with absolute concentration measurements the obtained molecular weight and size distribution of biomolecules are used to determine the abundance of bound and unbound species and with that the binding affinity of protein-protein interactions.[96]

Because of the ongoing dilution and separation within the SEC column true equilibrium is only achieved under carefully chosen conditions, where kinetics are very rapid or very slow on the time scale of the separation.[98] Therefore, binding affinities obtained under the assumption of fast or slow equilibration should be considered as estimates.[99]

Equilibrium methods, such as the Hummel-Dreyer method or large-zone equilibrium gel-filtration have only received limited attention due to high sample consumption.[5] For binding affinities of self-associating proteins, SEC-MALS is proposed as a simple alternative to AUC.[100,101] In 2010, Kapoor et al. showed that the multidomain calcium-binding protein Nucleobindin 1 (NUCB1) exists as a dimer and quantified the monomer-dimer dissociation constant with SEC-MALS (Figure 2.9).

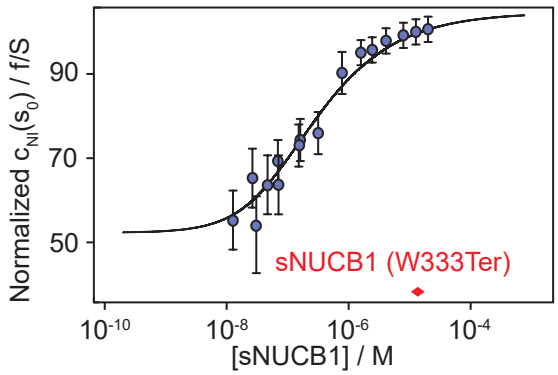


Figure 2.9: Experimental data of size-exclusion-chromatography multi-angle-light-scattering. SEC-MALS study of the monomer-dimer equilibrium of sNUCB1 fractions with increasing protein concentration in 50 mM Tris-HCl, pH 8.0, 150 mM NaCl. The weight average molecular weight of the complex at a given protein concentration was determined from a nonlinear least square fit of a collection of values determined for the apex fractions of each eluting peak. A monomer-dimer association model of the values as a function of sNUCB1 concentration gave an apparent K_d of 0.26 ± 0.12 μM. The error bars indicate the extent of variation in molecular mass determination originating from the light scattering measurement. The molecular weight of a truncated mutant sNUCB1(W333Ter), where the structural motif for dimerization was removed, is shown in red. Adapted from [102] with permission of ASBMB.

Although used in the past to quantify binding affinities of proteins [13,89] publications from 2017 on suggest that SEC-MALS is mostly used for purity, molecular weight, stoichiometry [103] and aggregation determination. In these publications SEC-MALS is then complemented by techniques such as SPR [26,27,104], MST [26], ITC [105–107], AUC [88], fluorescence spectroscopy [108] and flow cytometry [109] to measure binding affinities.

2.1.4 Solution-based Methods

CG-MALS

Composition-gradient multi-angle-light-scattering (CG-MALS) has an identical detection principle to the above described SEC-MALS technique, but allows for protein-protein interaction measurements at equilibrium. CG-MALS commercially introduced in 2010 can measure molecular weight distributions, binding

affinities (pM to mM) and kinetics (seconds to hours) for biomolecules with molecular weights ranging from 10^3 to 10^9 Da. Commercial instruments use a composition gradient system, where up to 3 components can be mixed in different ratios and total concentrations before being injected into a stop-flow cell (Figure 2.10a).

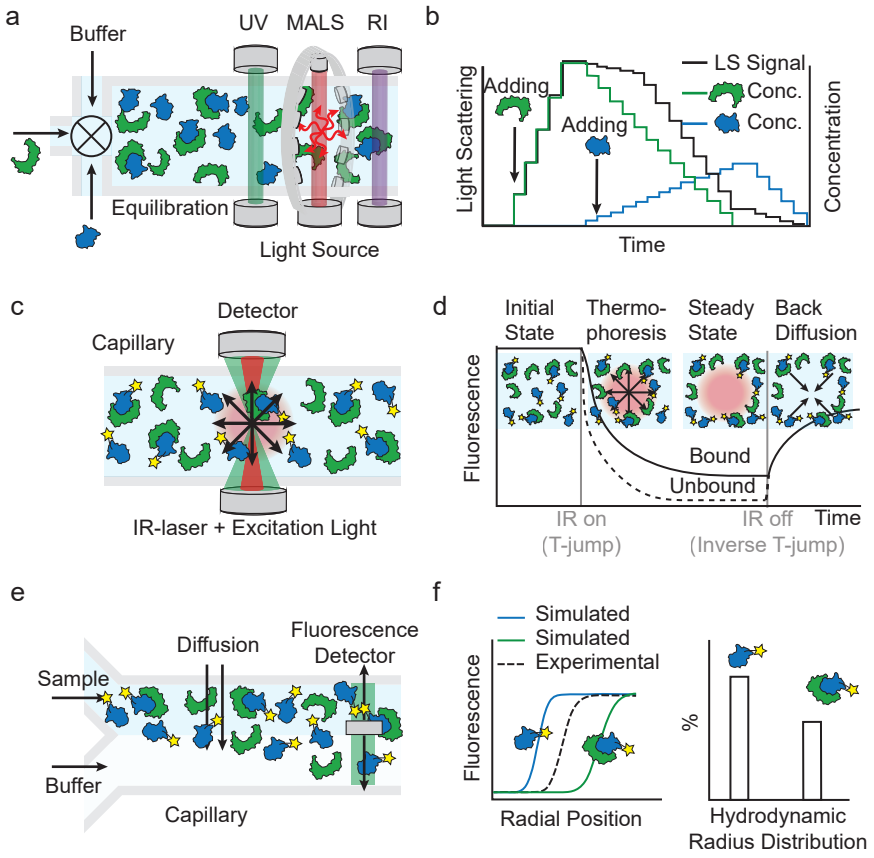


Figure 2.10: Solution-based methods for PPI quantification. Principles of composition-gradient multi-angle-light-scattering (a, b), microscale thermophoresis (c, d) and microfluidic diffusional sizing (e, f) are shown.

Like SEC-MALS the flow cell is monitored by a UV, RI and MALS detector to measure total concentration and average molecular weight of the macromolecule mixture in a time-resolved manner. Data is acquired for a series of different sample concentrations or compositions (Figure 2.10b). The average molecular weight, quantified with the MALS detector, serves as a measure for

the stoichiometry of the complex and most importantly the ratio of bound and unbound species. Fitting a binding model to the concentration dependent average size of the specie and the absolute concentration allows to extract the binding affinity values. Typical experiments have an unattended duration of ca. 3 hrs and software is available for analysis of the binding data.[110]

Advantages of CG-MALS are label-free measurements, minimal sample preparation and broad buffer compatibility. Compared to other methods, they often come with a relatively large sample consumption of several hundred μg per experiment. Moreover, the limited mass precision of MALS often requires further conformation via alternative methods and the limited mass resolution makes experiments where small molecular weight differences are involved challenging.[94]

Alternative approaches with CG-DLS described in literature, suggest that low sample consumption (few μl of nM to mM per data point) can be achieved.[94,111,112] High-throughput has also been described in literature, but is not yet available on commercial instruments.[113]

Recent applications focused on guiding mAb discovery and formulation by quantifying self-association binding affinities and oligomerization.[114–118] Pallesen et al. used CG-MALS to complement BLI studies of Ebola virus GP and antibodies.[119] In 2019, Hastie et al. applied CG-MALS to confirm binding affinities of Lassa virus surface glycoprotein (GPC) and antibodies (Figure 2.11).[110] In their work, they showed that the obtained K_{d}s in the nM range were in good agreement with their BLI experiments.

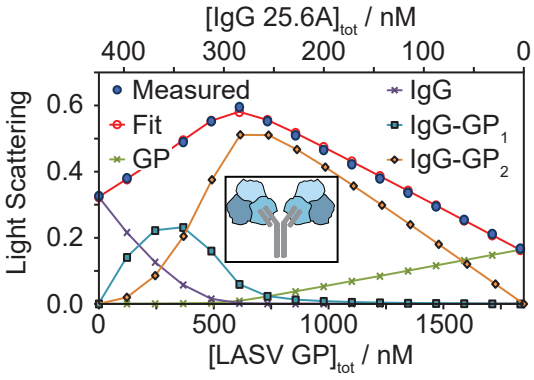


Figure 2.11: Experimental data of CG-MALS. Representative CG-MALS analysis of LASV GPCysR4 and GPC-B IgG 25.6A. Data displayed is the light scattering intensity as a function of composition. Blue circles indicate the measured light scattering intensity for each gradient plateau; Red circles indicate the fit to a model of up two GPC monomers bound to one IgG with a K_d of 9.8 ± 1 nM. The contribution from each species (GPC, IgG and GPC-IgG complexes) to the total intensity of light scattered is shown according to the legends. Adapted from[110] with permission of Elsevier.

These experiments show that CG-MALS accurately measures binding affinities, stoichiometries and molecular weight of biomolecules. Although measurements can be run unattended and data analysis is supported appropriate software, future efforts could help to further improve throughput and decrease sample consumption.

Microscale Thermophoresis

In microscale thermophoresis (MST) the directed movement of molecules in a temperature gradient is detected, using fluorescent tags or intrinsic fluorescence of the molecules. Commercialized in 2008 by NanoTemper, Germany, the technique has been applied for measuring binding affinities and stoichiometries of biomolecular interactions, enzyme kinetics and protein unfolding.[120]

In MST an infrared laser generates a local and steep temperature gradient in the focal volume of a glass capillary, containing the biomolecule sample (Figure 2.10c). The local temperature increase leads to thermophoretic movement of the sample molecules. This movement is proportional to the temperature

change but also dependent on physical properties of the sample molecule, such as size, charge or solvation entropy (Figure 2.10d).[121] This makes MST sensitive to changes in these properties, which are then detectable by fluorescence.

Fluorescence of biomolecules (intrinsic fluorescence or from the tag) is induced by an UV-LED and will change depending on thermophoretic movement.[121] In other words, a fluorescent protein will generate a different signal when it is bound to a ligand because its size and charge changed (Figure 2.10d). Similarly, a fluorescent protein which does not bind to a ligand, will always give the same signal, independent of added ligand concentration. Performing a titration series allows then to quantify the change in fluorescence intensity as function of ligand concentration. With that the binding affinity of the interaction can be quantified.

Compared to common methods (e.g. SPR or ITC) MST offers advantages such as fast experimental times (15 minutes or less), low sample consumption (μls of pM to mM), large dynamic mass range (10 Da to 10 MDa), immobilization-free measurements, compatibility with a wide range of buffers, and in case of fluorescently tagged biomolecules even detection in complex samples, such a pure mammalian cell lysates.[120,122]

Comparing manufacturer information (Nanotemper NT.115, NanoTemper Technologies GmbH, Germany), experimental data and simulations, a recent study suggest however that reported dynamic ranges in instrument specifications (experimental times, concentrations, binding affinities and kinetics) are considerably narrower.[123] Due to the contribution of different factors (size, charge, solvation entropy, conformational changes) to the change in fluorescence intensity, it can be challenging to disentangle the different contribution during data analysis.[121]

From 2017 to 2020, MST with fluorescently labeled proteins has been

applied to numerous protein-protein[26,124–129], protein-small molecule[126,130–138] and protein-DNA[139] interaction studies as well as high-throughput screening.[140] In 2019, Ridley et al. measured the binding affinity of fluorescently labeled N-terminal dimerization domain of MUC5B (NT5B) to the C-terminal construct of MUC5B (CT5B) (Figure2.12).[26] With their work they elucidated a potentially new role for the C-terminal dimerization domain of MUC5B.

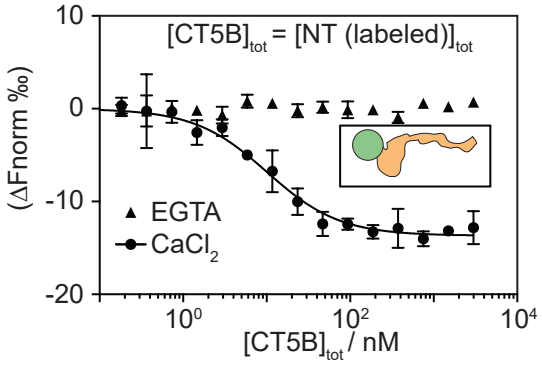


Figure 2.12: Experimental data of microscale thermophoresis. MST analysis of heterotypic interaction of MUC5B dimerization and multimerization domains. A serial dilution of CT5B protein was mixed with an equal volume of fluorescently labeled NT5B recombinant protein and interactions were measured by fluorescence using MST. Samples were prepared in HBS buffer containing 0.05% Tween 20 and either 5 mM $CaCl_2$ (circles) or 5 mM EGTA (triangles) at pH 7.4. Error bars represent the mean ± S.E. Experiments were repeated at least twice. Adapted from[26] with permission of ASBMB.

In 2012, Seidel et al. introduced a label-free MST method to quantify protein-ligand affinities based on intrinsic fluorescence.[141,142] This label-free method has been applied in a few protein-ligand studies from 2017 to 2020.[126,143,144]

Despite MST's potential, we could not find any study reporting a label-free protein-protein interaction quantification, since its introduction in 2012. We suspect that this is because label-free protein-protein interaction measurements with MST are limited to cases where only one of the two proteins shows intrinsic fluorescence. As most proteins have aromatic residues and intrinsic fluorescence

this is a limiting factor and could only be overcome with appropriate background subtraction for the signal contribution from the titrated protein.[121,141]

However, simple labelling and experimental procedures combined minute sample consumption and software supported data analysis make microscale thermophoresis a promising tool among emerging biophysical characterization techniques for PPI quantification measurements.

Microfluidic Diffusional Sizing

Microfluidic diffusional sizing (MDS) is a microfluidic platform, which measures hydrodynamic radii of biomolecules in solution.[145] In 2019, this technique has been made available by Fluidic Analytics, United Kingdom to quantify size distributions, aggregation, stoichiometries, binding affinities and kinetics of biomolecule interactions under native conditions. The miniaturised assays allow for analysis of protein-protein interactions with minimal sample consumption, short measurement times, low costs and the potential for high throughput.[71]

In MDS, two parallel solution streams are passed next to each other through the same microfluidic channel and are only separated by the laminar flow condition (Figure 2.10e). The microfluidic chip design allows to load one stream with the biomolecule sample and the second stream, called auxiliary stream, with blank buffer. In this setup, diffusion is the only mean of mass transport between the two streams. In this way, the degree to which sample is diffusing into the auxiliary stream is solely dependent on the diffusion coefficient, i.e. hydrodynamic radii, of the biomolecules.

UV or fluorescence-based detection of the diffusion profile in space and time, combined with global analysis allows to deconvolute the diffusion profiles and extract hydrodynamic radii and concentrations of involved species (Figure 2.10f). A titration series can then be performed to extract dissociation constants from the binding curves.[145]

Typical run times range between 15-60 s and therefore offer a time resolution relevant to many biological systems.[145] For studies with fluorescently labeled proteins, dissociation constants from nM to mM are accessible.

Recent studies featuring binding affinity measurements looked at binding of membrane protein aquaporin to the regulatory protein calmodulin[146], insulin to the small molecule Thioflavin-T[147], self-assembly of HSP70 sub domains[148], PIP2-binding peptides of TRPA1 with SMALPS[149] and α-synuclein to DOPS-lipid vesicles[150]. In 2019, Scheidt et al. used an in-house version of MDS to measure equilibrium constants of the Clusterin-Aβ(M1-42) complex (Figure 2.13).[151] Their work demonstrates that Clusterin's ability to inhibit the elongation of Aβ fibrils originates from interactions of clusterin with fibril ends with high affinity.

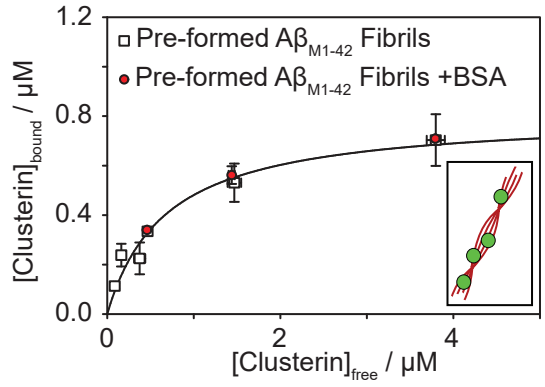


Figure 2.13: Experimental data of microfluidic diffusional sizing. Binding curve of clusterin to 17.5 mM Aβ(M1-42) fibrils in 20 mM sodium phosphate at pH 8.0 and 21 °C measured by the microfluidic diffusion technique. In a first set of experiments (squares), different concentrations of clusterin were incubated with previously generated Aβ(M1-42) fibrils and size distributions were measured after 48 hours of incubation to ensure equilibrium conditions. In a second set of experiments (circles), different concentrations of clusterin were incubated with 17.5 mM Aβ(M1-42) fibrils and BSA at equimolar concentrations to clusterin. Each point represents the mean and SD of at least two independent repetitions. The regression line (black) represents the best fit to the nonlinear Langmuir binding isotherm with K_d of 0.67 $\pm$ 0.19 mM and M = 0.80 $\pm$ 0.08 mM (corresponding to one clusterin molecule per 21 Aβ(M1-42) monomers), with R^2 = 0.97. Adapted from[151] with permission from AAAS.

The herein presented studies so far used fluorescently labeled molecules to quantify binding affinities, due to higher sensitivity and commercial availability of methods. However, recent efforts were directed towards label-free measurements of protein-protein interactions. In these experiments the intrinsic fluorescence of unlabeled proteins (from aromatic amino acids) is used for detection, which generally brings challenges related to lower signal-to-noise ratio.

In 2018, Challa et al. showed the potential at the example of protein self-association of αB-Crystallin, where they managed to determine formation of higher-order oligomers.[152] An alternative approach was proposed earlier by Yates et al. where separation of unlabeled molecules was performed before latent labelling and detection.[153]

Looking at the fast development and progress made in this field within a short time, first label-free binding affinity measurements of protein-protein interactions could be a next step. Similar to challenges faced in microscale thermophoresis, developing a procedure to disentangle intrinsic fluorescence contributions from analyte protein and titrated protein could be one way of achieving this.[141]

Mass Photometry

Mass photometry is a label-free optical method to quantify molecular weights of biomolecules at the single-molecule level by detecting interferometric light scattering. Commercialized in 2018 by Refeyn Ltd, it is applied for in-vitro quantification of molecular weight distributions, purity, aggregation, stoichiometry, binding affinities and kinetics of biomolecules and their complexes.

In MP, a biomolecule sample is injected onto a glass substrate (e.g. microscope coverslip). Illumination of the glass surface by a laser generates reflected

and back-scattered light from the glass-water interface, which is detected by a detector (CMOS camera) (Figure 2.14a).[3]

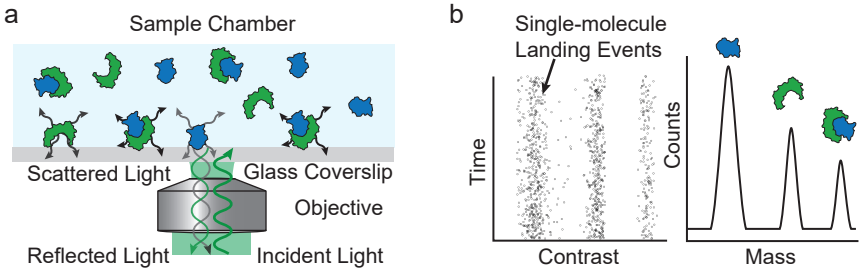


Figure 2.14: Mass photometry for PPI quantification. (a) Label-free analyte (green), ligand (blue) and complexes are detected by imaging the interference of scattered and reflected light arising from individual protein landing events at a glass-water interface over time. (b) Scatter plot of single-molecule contrasts and resulting mass distribution for a three-component system.

Small scatterers (compared to the wavelength of light) landing on the glass-water interface lead to a change in local refractivity and generate a light scattering signal. In case of single biomolecules it was shown that they bind irreversibly and non-specifically to this glass surface and generate a light scattering signal which is proportional to their molecular weight.[4,154] This phenomenon allows for label-free detection of biomolecules at the single-molecule level.

After calibration with molecular weight standards, the light scattering signals of hundreds to thousands detected biomolecules (depending on experimental conditions) can be converted to molecular weight and represented as molecular weight distribution (Figure 2.14b). MP reports molecular weight distributions with 2% mass accuracy, up to 19 kDa resolution, and 1 kDa precision.[4]

In 2020, Soltermann et al. showed that these molecular weight distributions accurately measure distributions of biomolecules in bulk solutions.[155] With this they were able to quantify binding affinities, kinetics and stoichiometries

of label-free protein-protein interactions. They showed that protein-protein interactions with binding affinities from low pM to 200 nM and kinetics in the minutes to hours scale can be quantified by MP. Their implementation of a microfluidic injection system also suggests accessibility of concentration ranges below pM.

As light scattering technique, MP has a unpreceded mass resolution, which allows to resolve even complex stoichiometries, such as the pH-dependent interaction of FcRN and IgG, involving 5 co-existing species (Figure 2.15).[155]

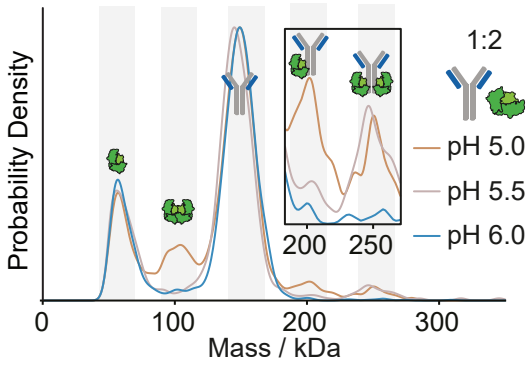


Figure 2.15: Experimental data of mass photometry. Binding affinity measurements of self-assembly of FcRn dimers and formation of IgG-FcRn complexes (1:2 mixture) at different pHs. Associated pH dependent binding affinities of interaction revealing cooperativity in FcRn binding. At pH 5.0 MP measured K_d values of 44 ± 9 nM (FcRN monomer-dimer), 59 ± 8 nM (FcRn-IgG) and 7 ± 1 nM (2 FcRn bound to one IgG), at pH 5.5 we obtained K_d values of 225 ± 20 nM (FcRN monomer-dimer), 117 ± 19 nM (FcRn-IgG) and 4 ± 2 nM (2 FcRn bound to one IgG). Adapted from[155] with permission from Wiley.

Beside these strengths, MP has practical advantages such as low sample consumption (a few μl of pM-nM sample per data point), compatibility with a wide range of physiological buffers, and user friendliness (minimal sample preparation and automated data analysis). Currently, detection of biomolecules is limited to molecules larger than 40 kDa (and >60 kDa for quantitative counting). Moreover, planning of binding experiments should take the above mentioned mass resolution into account.

A comparison of MP with established binding affinity measurement techniques by Wu et al. showed that MP binding affinity data of antibody-antigen interactions was in agreement with ITC and BLI measurements and superior in terms of stoichiometry determination.[156] Recently, MP has also been used to quantify binding affinities in the self-association of proteins (FOXP2 oligomerization[157], tubulin dimerization[158], CaMKIIα oligomerization[159]), qualitative assessment of affinities between serum haptoglobin protein and hemoglobin[160] and casposase and DNA[161].

Beyond PPI measurements, MP was used to reveal sample heterogeneity and guide purification processes for cryo-EM samples, as shown in the work of Sonn-Segev et al..[162] Other examples can be found in the purification process of first-time expression of fully post-translationally modified recombinant clusterin[163] or the assembly of ScRSU complex[164]. Recently, Li et al. and Olerinyova et al. showed that MP methods can be extended to other biomolecule classes, such as DNA[165] and membrane proteins[166]. Finally, the work of Lebedeva et al. is another indicator for the diversity of experiments which can be performed with MP. In their work they used MP to monitor formation and evolution of supramolecular assembly of amphiphiles into micelles and vesicles in real time.[167]

Future development of MP will likely focus on improvements in molecular weight range, mass resolution, concentration range and time resolution. Beyond advances in the MP technology, implementation of fully automated and high throughput instruments will help pave the way to establish MP as screening tool in drug development and gold-standard tool for purity, aggregation, stoichiometry, binding affinity and kinetic measurements.

2.1.5 Conclusion and Summary

In this literature review, we have seen that every technique comes with its advantage and limitations. If the term "ideal technique" existed, it would be applicable to various classes of biomolecules (e.g. DNA, proteins, glycans etc.), over several orders of magnitude in molecular weight, binding affinities and kinetics, while being label- and immobilization-free, as well as having low sample consumption, a high degree of automation combined with high reproducibility and high throughput.

Altering samples by inducing fluorescent tags or immobilization are limitations which can hardly be circumvented with existing techniques, especially when working with an analyte-ligand system where both parts are proteins or where sample amounts or binding affinities require measurements at sub-μM concentrations.

Moreover, most methods can only indirectly infer stoichiometries of interactions by finding "best-fit" models for the experimental data. This can result in misinterpretation of data or the requirement of highly trained users, both aspects are likely to hamper a broad applicability of a technique in the long-term.

The reasons for the dominance of certain techniques like SPR or BLI are severalfold. Firstly, they show outstanding performance for many of the afore mentioned criteria. Their experiments offer not only access to binding affinities but also kinetics and to a certain extent also stoichiometry over large dynamic ranges and with low sample consumption. Secondly, the combination of highly standardized experimental protocols and data analysis makes it accessible to a broad range of users. Thirdly, a high degree of automation reduces the required time-efforts to an absolute minimum.

Emerging techniques, such as CG-MALS, MST or MDS overcome limitations such as immobilization or labelling. Moreover, they can provide additional information such as molecular weight and stoichiometry of the interaction. Making these techniques accessible to a broader audience by offering commercial instrument is a first step of providing valuable alternatives to immobilization-based techniques like SPR and BLI. Further development in user-friendliness, throughput and reduced sample consumption will further help to establish these techniques.

It is also in these areas where we see the potential of mass photometry and the need to further explore its performance and capabilities to help establishing MP as a universal tool for studying biomolecular interactions and dynamics in a rapid and label-free fashion.

Having dedicated this thesis to the method development and applications of mass photometry for biophysical characterization of protein-protein interactions we would like to first provide the reader with a more detailed introduction to MP, its history, and theoretical concepts needed for binding affinity and kinetic measurements of PPIs.

2.2 Mass Photometry

2.2.1 Principle

Mass photometry (MP) is an all optical method based on interferometric scattering microscopy (iSCAT) which can differentiate and count single biomolecules based on their iSCAT contrast. This signal was shown to be proportional to the molecular weight of a biomolecule.[4] Ultimately, MP enables *in-vitro* measurements of biomolecule samples to determine purity and molecular weight distributions, as well as interactions and dynamics of biomolecules.[4]

In mass photometry, the aqueous sample is dropped onto a transparent substrate, e.g. a microscope coverslip glass. This coverslip is installed on top of a setup, which resembles an inverted microscope. More specifically, the coverslip is placed on an oil immersion lens objective, through which light (e.g. laser at 445 nm) is focused onto the glass-water interface (Figure 2.16). The majority of the incident light (E_I) is transmitted and not of interest. The small part of reflected (E_R) light, together with the even less intense scattered light from the glass surface and analyte molecules (E_S) is collected by the high numerical aperture objective and will serve as our signal when we come to the signal processing part later.

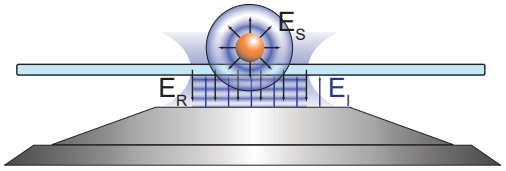


Figure 2.16: Signal detection in interferometric scattering microscopy. A microscope objective focuses incident light (E_I) onto the sample and collects the reflected light (E_R) at the glass coverslip interface and the light scattered by particles (E_S). This figure is adapted with permission from Fineberg, A., Interferometric scattering microscopy: from bacterial dynamics to molecular assembly, University of Oxford, PhD thesis.[168].

Looking at the architecture of the interferometric scattering microscope in more detail (Figure 2.17), we see that the incident light is generated by a diode laser (e.g. 445 nm). Given the $1/\lambda^2$ dependence of interferometric contrast, smaller wavelength lasers are preferred. After being collimated the beam is deflected by a set of two orthogonally oriented acoustic-optical deflectors (AODs), which will later on allow to scan the field of view.

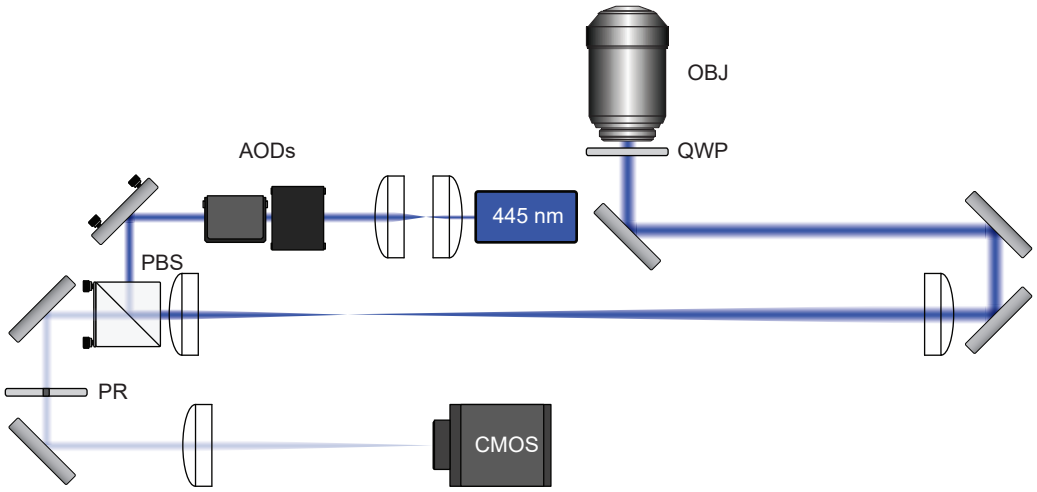


Figure 2.17: Architecture of an iSCAT microscope for mass photometry. This figure is adapted with permission from Fineberg, A., Interferometric scattering microscopy: from bacterial dynamics to molecular assembly, University of Oxford, PhD thesis.[168]

After the AODs the beam is passed through a polarizing beam splitter (PBS) and a quarter wave plate (QWR). The combination of PBS and QWR allow for efficient separation of incident and reflected light. Afterwards the oil immersion lens objective focuses the beam onto the glass-water interface between coverslip and aqueous sample. At this point, the deflection and rapid scanning of the beam, generated by the AODs (at ca. 100 kHz, i.e. 100x faster than the frame rate of the camera), lead to an even illumination profile in our field of view (FOV). The interaction between incident light and nanoscopic objects, described as Rayleigh scattering, is the basic principle of MP and iSCAT. In this theory, particles much smaller than the wavelength of light, can be excited due to their electric polarizability and are turned into radiating dipoles, emitting scattered light in all directions. In iSCAT reflection mode, the objective collects the back-scattered light from the glass surface and analyte molecules (E_S) together with the reflected (E_R) from the glass-water interface. In the back-focal plane of the objective, the light is passed through

the polarizing beam splitter, which separates incident from collected light. The detected intensity, I_{det}, is then given by,

$$I_{det} = I_{inc}[r^2 + |s|^2 + 2r|s|cos(\phi)], \tag{2.1}$$

where I_{inc} is the incident intensity, r^2 is the reflectivity of the glass-water interface, s is the scattering amplitude of the object of interest, and ϕ is the phase difference between the reflected and the scattered fields at the detector. According to Mie theory in equation 2.2, the scattering amplitude of a small scatterer, s, can be written as

$$s = \eta\epsilon_m\pi\frac{D^3}{2}\frac{\epsilon_p - \epsilon_m}{\epsilon_p + 2\epsilon_m}, \tag{2.2}$$

where $\epsilon_{m/p}$ are the dielectric functions of the surrounding medium/particle, respectively. D is the diameter of the spherical particle and η is a constant factor specific for the detection efficiency of the setup. From this equation we see that the scattering signal scales with polarizability of the small scatterer and is therefore a function of refractive index and proportional to the particle volume. It is this universal nature of light scattering, which eventually enables label-free detection of objects, as small as single biomolecules.

From these equations, we also understand that the pure scattering term $|s|^2$ in equation 2.1 drops quickly with object size. Furthermore, we conclude from equation 2.1 that the pure scattering term becomes negligible, when detecting weak scatterers, i.e. scatterers with dielectric constants similar to the medium and $r \gg |s|$. By distinguishing between light intensity in the presence, I_{det}, and absence, I_{bkg} of a scatterer we can define a direct measure for the interferometric scattering contrast c as,

$$c = \frac{I_{det}}{I_{bkg}} = 1 + \frac{2|s|cos\phi}{r}. \tag{2.3}$$

One approach to increase the measured contrast of a biomolecule is reducing the reflectivity of the interface r. According to the Fresnel reflectance (equation 2.4) matching the refractive indices of the sample solution with the glass substrate would help but comes at the expense of biological incompatibility when changing from water to another solvent.

$$R = \left| \frac{n_1 - n_2}{n_1 - n_2} \right|^2 \tag{2.4}$$

Alternatively, the substrate surface could be coated, although limitations such as residual reflections from lenses within the microscope objective and especially costs involved in coating substrates instead of using commercially available low-cost microscope coverslips make this approach impractical.[3]

A much more elegant approach is to make use of the different directionalities of reflected and scattered light in the Fourier-transformed space, as described by Cole et al..[3] Placing a partial reflector (PR, Figure 2.17) in the centre of the beam path and choosing an appropriate diameter and transparency, reflected light travelling in the centre of the beam can be selectively attenuated, while leaving the scattered light at the edges of the beam mostly unaffected. Ultimately, this enables detection of small scatterers with low-cost CMOS cameras, but itself is still insufficient to detect scatterers as small as single protein molecules.

To make the single biomolecules visible, a last step is required, which is performed outside of the microscope: background removal during image processing. As shown in Figure 2.18a consecutive blocks of raw images can be subtracted from or normalized to each other to remove background scattering from the static glass-surface. After background subtraction, we see, that the single proteins become visible as black dots (Figure 2.18b). Their intensity corresponds to their ratiometric contrast value (Eq. 2.3).

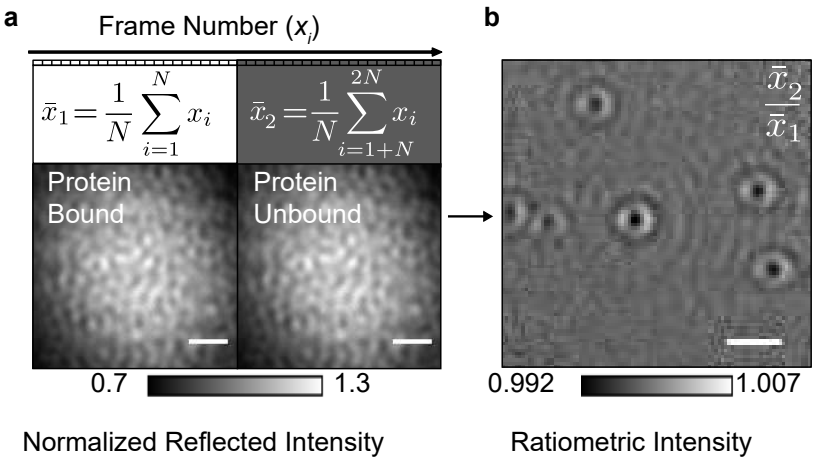


Figure 2.18: Ratiometric iSCAT imaging of single proteins. (a) Concept of iSCAT ratiometric imaging dividing averages of consecutively recorded images. (b) Resulting ratiometric image using N = 100, revealing the binding of HSP16.5 to a bare cover glass surface. Incident power density: 45 kW/cm^2; exposure time: 1.4 ms; frame rate: 700 Hz; 2 × 2 pixel binning; HSP16.5 monomer concentration: 240 nM; scale bar: 1 μm. This figure is adapted from D. Cole, et al., Label-Free Single-Molecule Imaging with Numerical-Aperture-Shaped Interferometric Scattering Microscopy, ACS Photonics, 2020, 4, 211-216.[3] Reprinted with permission from ACS.

In Figure 2.18 it was shown how one ratiometric image is generated from two consecutive blocks of averaged raw images. In Figure 2.19, we illustrate how this procedure can be applied to convert an entire movie of raw images into a movie of ratiometric images (a). It is important, and initially counter-intuitive, to understand why the signal of a landing event seems to first get stronger and then fade away (Figure 2.19), indicated by small arrow at different time points (-0.10 to 0.10 s).

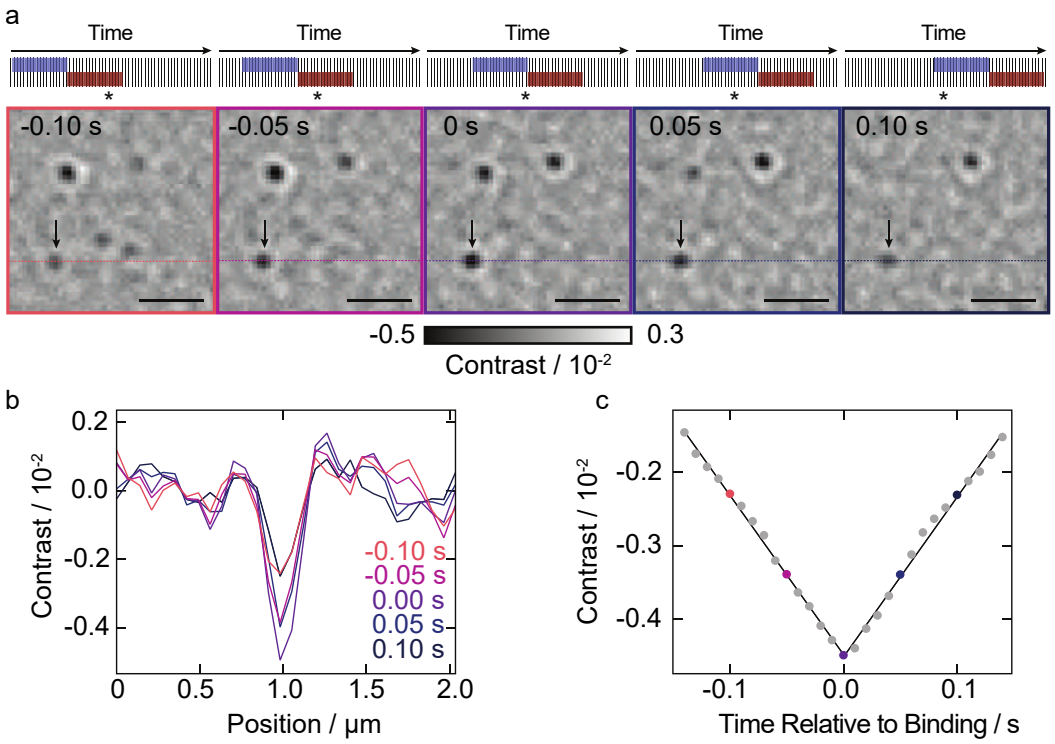


Figure 2.19: Principle of single-molecule landing detection shown as time-dependence of a protein binding signal subject to the sliding background ratiometric processing. (a) Illustration of the image averaging and ratiometric imaging approach. The asterisk marks a landing event. Individual images are averaged into two consecutive blocks (blue and red), which are normalized and divided to provide differential contrast. The mid-point is scanned in time, meaning that the signal from stochastic landing events grows and fades, as indicated by the black arrow. Scale bars: 1 μm. (b) Corresponding cross-sections for the particle highlighted in (a). (c) Corresponding signal magnitudes extracted by a fit to the PSF and fit (black). This figure is adapted with permission from Young, G., Mass Photometry: Weighing Single Molecules with Interferometric Scattering Microscopy, University of Oxford, PhD thesis.[169]

On the time scale of our camera frame rate, the protein landing is very fast and happens within the time span of one frame. The landed particle stays on the surface and eventually becomes part of the background. The scattering particle does not approach the surface, land and then take off again. The apparent appearing and disappearing of the signal is a result of the image processing.

In more detail, it is the averaging of consecutive blocks of raw images

which causes a gradual increase of measured contrast (Figure 2.19c), until the maximum value is reached, followed by a decrease until the signal apparently disappears. This maximum ratio between the two consecutive blocks is reached when all frames in the leading block already contain the signal of the landed particle, and all frames in the second block do not contain the landed particles yet. After reaching this value, the particle contrast decreases again, as particle becomes part of the second block. Extraction of the contrast values from the images is achieved by point spread function (PSF) fitting. A particle is confirmed as a "real" particle if it shows the expected behavior of increasing/decreasing contrast in the ratiometric movie and when pixels in the proximity of the putative particle follow a circular symmetry. The maximum contrast of the particle, as well as time point and position in the FOV is then written to an output file.

Being able to quantify the ratiometric contrast of single biomolecules becomes interesting when looking at equations 2.1 and 2.2 in more detail. For nano-objects with dimensions much smaller than the wavelength of light and with small differences in refractive indices and densities, the scattering signal should become proportional to molecular weight. Indeed, this could be shown in 2018 by Young and Hundt et al.[4] and two other groups[154,170] (Figure 2.20). In their work they characterize mass accuracy and precision of molecular weight measurements with mass photometry.

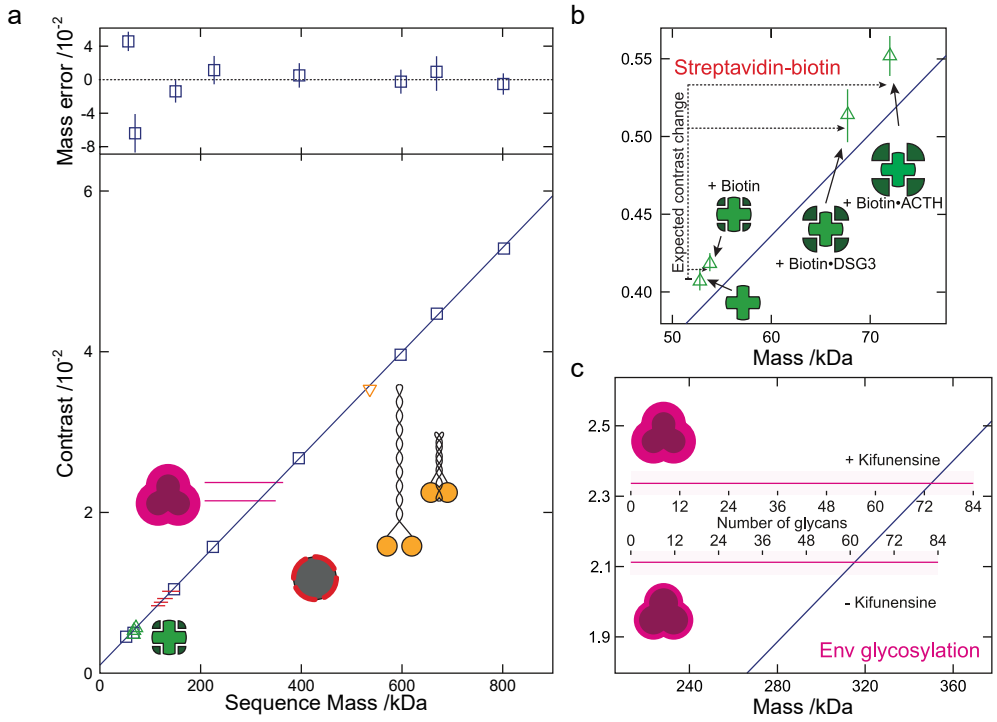


Figure 2.20: Characterization of mass accuracy, precision, and dependence on molecular shape and identity. (a) Contrast versus molecular mass, including proteins used for mass calibration (black), characterization of shape dependence (yellow), protein-ligand binding (green), lipid nanodiscs (red), and glycosylation (blue). Mass error (upper panel) is given as a percentage of the sequence mass relative to the given linear fit. (b) Nanodisc mass measurement for different lipid compositions and protein belts. Masses obtained by alternative methodologies for MSP1D1/DMPC are marked and extrapolated to the other compositions. The horizontal bars indicate the expected mass range as a function of characterization technique, with the thin bars indicating the contrast measured and the thick bars representing the measurement uncertainty. For each sample, the upper text denotes the membrane scaffold protein, and the lower text indicates the lipids composition. (c) Contrast for Env expressed in the presence or absence of kifunensine and associated mass ranges expected for different glycosylation levels. In (b, c) the line denotes the calibration obtained from (a). Errors are given as standard error of the mean (SEM) from repeated measurements. This figure is adapted with permission from G. Young, et al., Quantitative mass imaging of single biological macromolecules, Science, 2018, 360, 423-427.[4] Reprinted with permission from AAAS.

Young and Hundt et al. also found that refractive indices and specific volumes of amino acids vary by only ∼1 % (Figure 2.21), thus enabling molecular weight measurements of protein samples with high mass accuracy, label-free and on a single molecule level.

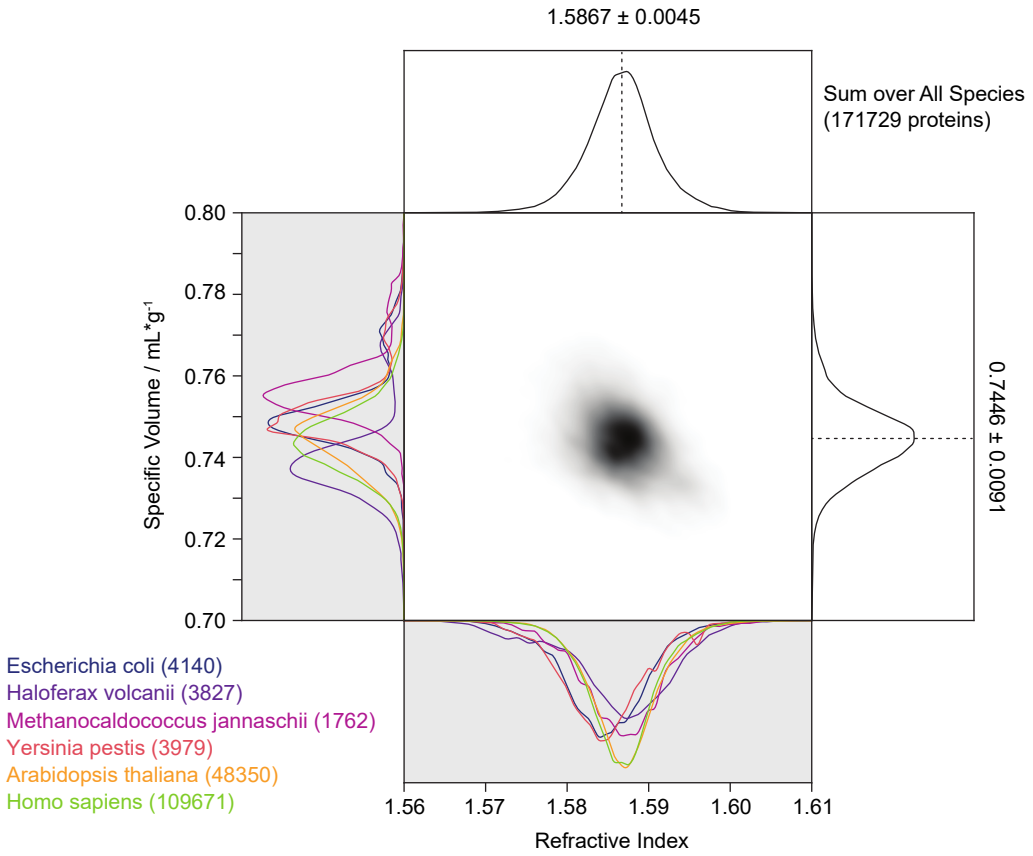


Figure 2.21: Distribution of refractive index and specific volume for different proteins. One-dimensional distributions of refractive index (top, bottom) and specific volume (left, right) for all proteins in six genomes, as calculated from the amino acid sequences, and the two-dimensional distribution of both quantities (middle). The top, right, and middle panels show the combined data from all genomes. The left and bottom panels show the respective distributions for the separate genomes, renormalized to have identical areas. This figure is adapted from G. Young, et al., Quantitative mass imaging of single biological macromolecules, Science, 2018, 360, 423-427.[4] Reprinted with permission from AAAS.

An overview of such a molecular weight measurement with MP is shown in Figure 2.22. We can see that injecting a 1:1 mixture of a monoclonal antibody monomer and a stable dimer, at nM concentration, results in images where black dots of different contrast values appear in the FOV (Figure 2.22a). Analyzing a 60 s video sequence of such an experiment reveals a molecular weight distribution with distinct peaks for the monomer and dimer at their respective molecular weights (148 and 296 kDa) (Figure 2.22b).

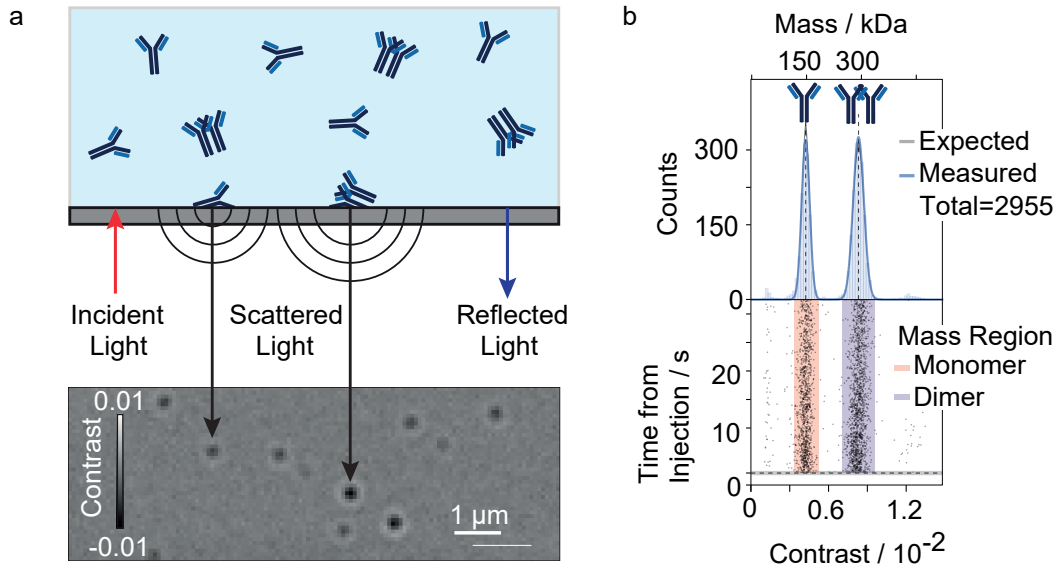


Figure 2.22: Principle of single-molecule counting by mass photometry. (a) Label-free single-molecule detection by imaging the interference of scattered and reflected light arising from individual protein landing events at a glass-water interface over time. (b) Scatter plot of single-molecule contrasts and resulting mass distribution for a 1:1 monomer/ dimer 2G12 mixture. This figure is adapted with permission from F. Soltermann, et al., Quantifying Protein–Protein Interactions by Molecular Counting with Mass Photometry, Angewandte Chemie International Edition, 2020, 59, 10774-10779.[155]. Reprinted with permission from Wiley.

2.2.2 History and Prior Work

Mass photometry has its roots in the early 1990, when Amos et al. managed to image subdiffraction objects with a reflected light microscope to study microtubule dynamics.[171]. In 2004 it was shown that the elastically scattered light of nanoparticles could be detected with an interferometric optical detection scheme described in[172]. They could detect single gold nanoparticles with diameters down to 5 nm in an immersion oil covered sample using white-light illumination. From here it took more than 15 years until the technique became a biophysical characterization tool with worldwide application in biological research in industry and academia. In this section we look at this transition period and give an overview of the most important developments. For readers with interest in specific technical details we refer to the review from Young et

al..[173]

Detecting, tracking, and imaging small objects, like gold nanoparticles or even single biomolecules, is extremely challenging due to the negligible signal from these minuscule objects compared to the background signal. However, this holds also true for light scattering experiments, where the scattering cross section is inversely proportional to the sixth power of the particle diameter.[174] In other words, reducing the object diameter by a factor 10, reduces the pure scattering signal by a factor of 10^6. Therefore, achieving the sensitivity to differentiate an object as small as a single biomolecule from background has been particularly challenging.

Fluorescence microscopy was a method which mastered the challenge of single biomolecule detection by maximizing the signal and minimizing the background. Over the past 20 years it has been the dominating method in single molecule microscopy. The main advantage was the unprecedented SNB background by 6 orders of magnitude while leaving the fluorescence signal mostly unaffected.[173] Unfortunately, fluorescence microscopy comes with significant limitations, such as photobleaching, blinking, need for fluorescent labeling and the limited response from a single emitter due to optical saturation. Photobleaching is a light induced damage of the fluorophore, where as photoblinking is a reversible switching between an on and off state. Both phenomena lead to a loss of fluorescence signal during imaging. A way to overcome these limitations are light-scattering-based techniques. They can be performed label-free and without photobleaching. This simplifies experimental procedures, makes measurement of unmodified and unlabeled protein possible and enables theoretically unlimited observation times due to the lack of photobleaching.

A way towards light scattering experiments with lower background is darkfield observation in scattering microscopy. Scattered light from the sample

and illumination light are captured in transmission and can be separated due to different spatial distributions.

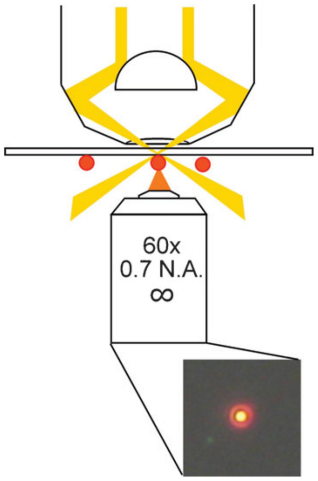


Figure 2.23: Schematic of dark-field microscopy of gold nanoparticles. Spatial separation of incident light (yellow) and scattered light (orange) from a goldnanoparticle (red) is illustrated. This figure is adapted from M. Hu, et al., Dark-field microscopy studies of single metal nanoparticles: understanding the factors that influence the linewidth of the localized surface plasmon resonance, Journal of Materials Chemistry, 2008, 18, 1949-1960.[175] Reprinted with permission from RCS.

Even though this background removal significantly improves the sensitivity, it does not sufficiently compensate the loss of signal intensity when going from gold-nanoparticles to single biomolecules. Here, reducing the particle size still leads to a decrease in scattering cross section which drops with the particle volume to the power of 2.[174] If we take the example shown in the paper of Young et al.[173], we see that the fluorescence signal difference between a microtubulus composed of 300 tubulin dimers or a single dimer changes the signal by a factor of 300. In pure scattering a 300-fold decrease of object size would cause a dramatic signal drop in the order of 10^5. Given that the background reduction with darkfield microscopy is not significant enough to go to object sizes as small as single biomolecules, we still need other avenues to detect scattering signals while keeping the background low.

In contrast to the square dependence of scattering signal on particle volume for pure scattering, interferometric scattering shows a linear dependence and is therefore more suitable for the down scaling of object size. Additionally, detecting interferometric scattering in reflection mode provides a reference field which can be used for background subtraction, as described in the work of Lindfors et al..[172] This alternative approach assumes that scattering by objects in the backward and forward directions is the same.

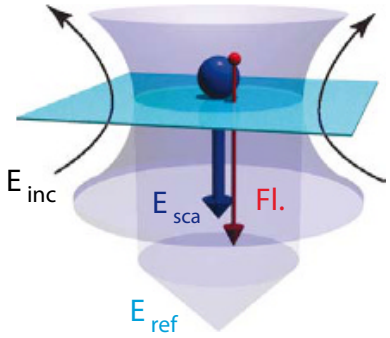


Figure 2.24: Schematic of interferometric scattering experiment. E_{inc}, incident light field; E_{sca}, scattered light field; E_{ref}, reflected light field; and not relevant here: Fl., QD fluorescence emission. This figure is adapted from P. Kukura et al., High-speed nanoscopic tracking of the position and orientation of a single virus, Nature Methods, 2009, 6, 923-927.[176]. Reprinted with permission from Springer Nature.

Compared to Lindfors et al., where gold nanoparticles were detected in immersion oil, Jacobsen et al. demonstrated that they can detect 5 nm sized nanoparticles with a similar interferometric microscope setup in aqueous solution.[177] This was important because it opened up a whole range of new possibilities, especially in terms of biological samples, at least in theory.

Indeed, it was only three years later, in 2009, when Kukura et al. resolved nanoscopic dynamics of individual biological nano-objects with the method termed interferometric scattering detection (iSCAT).[176] They combined scattering interferometry and single-molecule fluorescence microscopy to a co-localization method with which they could visualize position and orientation

of a virus particle labeled with a quantum dot.

By 2014, the detection and imaging of proteins as small as 60 kDa was achieved and shown at the example of myosin 5a.[178]

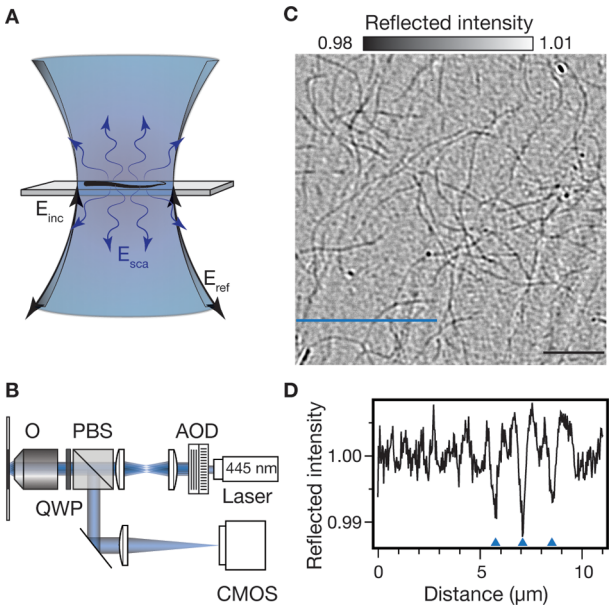


Figure 2.25: Interferometric scattering microscopy of biomolecules. (a) Schematic of the sample region including incident E_{inc}, reflected E_{ref}, and scattered E_{sca} light fields. (b) Experimental setup. O, objective; QWP, quarter wave plate; PBS, polarizing beamsplitter; AOD, acousto-optic deflector. (c) iSCAT image of individual, unlabeled actin filaments adhered to a microscope cover glass. Pixel nonuniformity and illumination inhomogeneity is removed by flatfielding with a temporal median filter (see Methods). Scale bar: 5 μm (black line). (d) Signal profile of the blue line in (c) shows three actin filaments indicated by the blue arrowheads. This figure is adapted from A. Ortega et al., Label-Free, All-Optical Detection, Imaging, and Tracking of a Single Protein, Nano Letters, 2014, 14, 2065-2070.[178] Reprinted with permission from ACS.

The notion that scattering cross sections of single biomolecules were by orders of magnitude too small for detection was herewith disproved. Being label-free and not relying on fluorescence made iSCAT overcoming inherent limitations to fluorescence spectroscopy such as limited localization precision, photobleaching, blinking and labelling protocols. With improved instrumentation the expected dependence of the iSCAT contrast on particle volume became even for single biomolecules measurable.[178]

Making the assumption that proteins have similar refractive indices and densities, the particle volume of a protein was expected to be proportional to its molecular weight. This expected linear relationship of molecular weight vs. iSCAT contrast was observed in the work of Piliarik et al.[170], where they compared the iSCAT contrasts of BSA, IgG1, CEA and fibrinogen. While still struggling with significant background contributions, the robustness of the measurements was sufficient to count single biomolecules and quantify their molecular weights. Moreover, measurements at different concentration ranges and with modified coverslip glass surfaces were performed to further explore the biosensor capabilities of iSCAT, but did not go beyond proof-of-principle experiments.[170,176] These findings showed the incredible potential of iSCAT to the scientific community.

However, it was the developments published by two different groups in 2017 that paved the way for a widespread adoption as biosensor technique.[3,154]

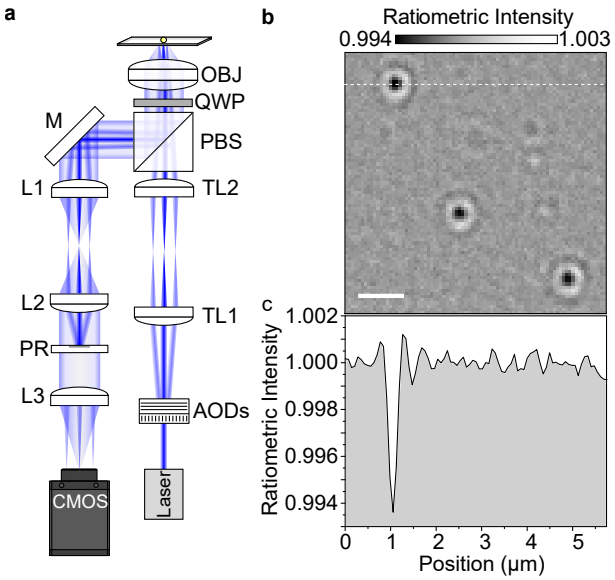


Figure 2.26: Label-free single-molecule imaging with numerical-aperture filtered iSCAT using rapid beam scanning. (a) Experimental setup based on acousto-optic deflector (AOD) scanning of a collimated beam using a telecentric imaging setup (TL1/ 2). The combination of a $\gamma/4$ waveplate (QWP) and polarizing beam splitter (PBS) separates incident from scattered and reflected light. Two lenses (L1/2) create an image of the back focal plane of the microscope objective (OBJ) where the partial reflector (PR) attenuates the back-reflected beam while leaving scattered light effectively unchanged. A final lens (L3) forms an image on the CMOS camera. Using a 3.5 mm diameter partial reflector together with a 1 mm diameter collimated illumination beam provides a good compromise between confocal sectioning and background attenuation. (b) Resulting ratiometric image using N = 150 revealing the binding of HSP16.5 to a bare cover glass surface. The weak bright features are caused by proteins unbinding from the surface. Incident power density: 150 kW/cm2; exposure time: 1.9 ms; frame rate: 500 Hz; 3 × 3 pixel binning; HSP16.5 monomer concentration: 240 nM; scale bar: 1 μm. (c) Image cross section from the dashed white line shown in (b). This figure is adapted from D. Cole et al., Label-Free Single-Molecule Imaging with Numerical-Aperture-Shaped Interferometric Scattering Microscopy, ACS Photonics, 2017, 4, 211-216.[3]. Reprinted with permission from ACS.

The introduction of a partially reflecting mask in an image plane of the iSCAT microscope detection channel combined with a efficient background subtraction allowed for selective attenuation of the intense reference signal over the weak scattering signal. In this way, expensive, high dynamic range cameras with large full well capacities could be replaced by low cost CMOS cameras. In combination with miniaturizing the imaging path[3] this allowed

for cost efficient bench-top iSCAT microscope, which help to make all optical, label-free sensors for nanoparticle detection and analysis widely accessible.[3,154]

Coinciding with the first commercialization of the iSCAT technique in 2018 by Refeyn Ltd. the term "mass photometry" was introduced. It is an overarching description for a set of iSCAT-based experiments with which biomolecule sample composition, interactions and dynamics can be investigated, as described in the paper of Young and Hundt et al..[4] Young and Hundt et al. showed the detection of label-free, single biomolecules, the quantification of their molecular weight, and propose routes to quantify protein-protein interactions.

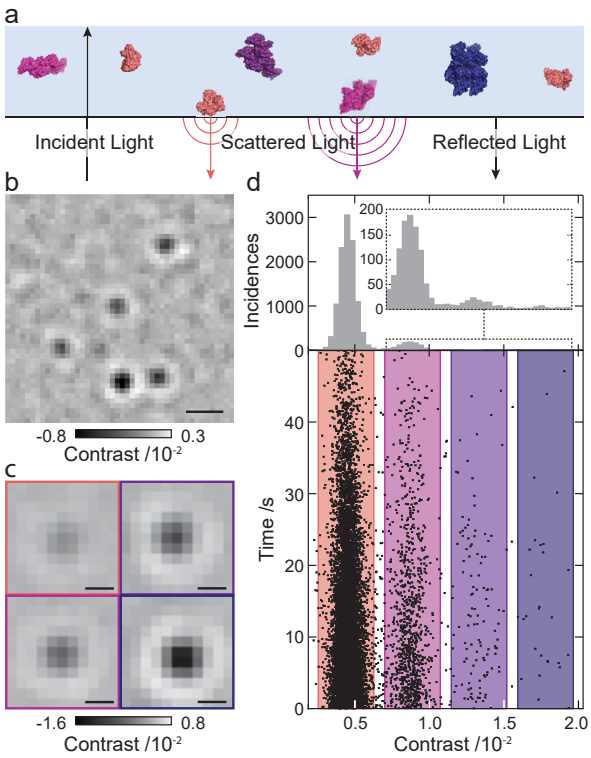


Figure 2.27: Concept of mass photometry (MP). (a) Schematic of the experimental approach relying on immobilization of individual molecules near a refractive index interface. Oligomeric states are colored differently for clarity. (b) Differential interferometric scattering image of BSA. Scale bar, 0.5 μm. (c) Representative images of monomers (top left), dimers (bottom left), trimers (top right), and tetramers (bottom right) of BSA. Scale bars, 200 nm. (d) Scatter plot of single-molecule binding events and their scattering contrasts for 12 nM BSA from 14 movies (lower panel). Corresponding histogram (n = 12,209) with a zoomed-in view of the region for larger species (upper panel). The reduction in landing rate results from a drop in BSA concentration with time owing to the large surface to volume ratio of our sample cell (supplementary materials). This figure is adapted from G. Young and N. Hundt et al., Quantitative mass imaging of single biological macromolecules, Science, 2018, 360, 423-427.[4]. Reprinted with permission from AAAS.

2.2.3 Open Questions

The accuracy of the protein-protein interaction measurements in the work of Young and Hundt et al.[4], as well as various dynamic ranges (e.g. concentration, dissociation constants, kinetics, stoichiometry) remained largely unexplored. Investigating how accurately the measured molecular weight distribution represented the real in-solution distribution should be a first goal. Subsequently it

would be interesting to understand under which conditions these measurements remain accurate and what the simplest and still accurate experimental procedures are. After having understood what mass photometry can do and how to best achieve it, it should be investigated how these measurements compare to established biophysical characterization techniques. Finally, it is important to choose appropriate examples to demonstrate the strengths and limitations to the scientific community.

Before going into this investigation and demonstration process in the next chapters, we should equip the reader with the essential concepts on how protein-protein interactions can be quantitatively assessed. For this purpose, we explain here the theory behind thermodynamics and kinetics of protein-protein interactions in solution.

2.3 Quantitative Analysis of Protein-Protein Interactions

Interactions between proteins govern processes and signaling pathways ultimately determining health and disease. Biophysical methods to characterize these interactions are instrumental in understanding the mechanisms and helping to develop new therapies against malignancies. We remind ourselves of the effort which has been put into the field of biophysical characterization when looking at the techniques presented in section 2.1.1. The data generated by these methods are all measures for certain thermodynamic or kinetics quantities. After appropriate data analysis and interpretation, they allow us to make comments about binding affinities and rate constants. To avoid misinterpretations of experimental outcomes it is important to understand basic experimental and theoretical concepts. This will also help to better understand the conversion of experimental data to quantities which universally describe protein-protein

interactions.

2.3.1 Thermodynamics and Kinetics of Protein-Protein Interactions in Solution

In general, thermodynamic parameters describe the state of a reaction after reaching equilibrium, while the kinetics describe the process of reaching this equilibrium. When it comes to binding affinities and reaction rates, the thermodynamic parameters are often expressed as dissociation constants (K_d) and the kinetic parameters as on and off rates (k_on, k_off). An exaggerated example of their mutual relevance is a receptor-binding antibody designed to prevent binding of another protein to the receptor. A successful antibody shows a strong binding affinity to the receptor. However, this binding affinity is only beneficial if matched with the right kinetics. Having an antibody which immediately dissociates after binding will most likely not show the desirable effect, contrarily an antibody that stays at the receptor for too long could cause complications. Thus, it is essential to have a good understanding of both kinetic and thermodynamic properties of the interaction of interest.

An important concept to understand thermodynamics of reactions in solution are chemical potentials.[179] We will see here how they help us to describe the initial ($G_{initial}$) and the final state (G_{final}) of a reaction and thereby calculating the driving force, the change in Gibbs free energy, ΔG.

$$\Delta G = G_{final} - G_{initial} \tag{2.5}$$

The sign of ΔG defines the spontaneity of a reaction (Table 2.1). From this it is intuitive that a reaction with a driving force equal to zero came to a halt, or for a reversible reaction, reached equilibrium. To further explain this we look best at an exemplary reaction as shown here,

$$aA + bB \longrightarrow cC + dD, \tag{2.6}$$

Table 2.1: ΔG values and their meaning

ΔG	Meaning
$\Delta G < 0$	spontaneous reaction
$\Delta G = 0$	equilibrium
$\Delta G > 0$	non-spontaneous reaction

where a moles of A and b moles of B react to c moles of C and d moles of D, all at molar concentrations [A], [B], [C] and [D]. With equation 2.6 and the assumption that we are working at constant temperature and pressure[179], we can express ΔG as function of the chemical potentials μ of the educts and products,

$$\Delta G = d\mu_D + c\mu_C - a\mu_A - b\mu_B. \tag{2.7}$$

Here, the equilibrium condition is met when chemical potential contributions of educts and products balance each other out. A chemical potential of a reactant, e.g. reactant A, depends on its standard chemical potential μ_A^0, molar concentration [A], molar standard concentration $[A]^0$, the dimensionless activity coefficient γ_A and temperature T, as:

$$\mu_A = \mu_A^0 + RT \ln\frac{[A]}{[A]^0} + RT \ln\gamma_A. \tag{2.8}$$

The activity coefficient γ describes the behavior of the real vs. ideal solution. For low concentration, γ is equal to one, which makes the logarithmic activity term neglectable. This holds also true for the work presented in this thesis where we will be working at low μM to pM concentrations. The division by the standard reference concentration $[A]^0$, set to 1 mol/l, ensures that the logarithmic concentration term stays dimensionless. Replacing all chemical potentials μ in equation 2.7 accordingly and neglecting the activity term yields

$$\Delta G = (d\mu_D^0 + c\mu_C^0 - a\mu_A^0 - b\mu_B^0) - RT \ln\frac{[A]^a[B]^b}{[C]^c[D]^d} + RT \ln\frac{([A]^0)^a([B]^0)^b}{([C]^0)^c([D]^0)^d}. \tag{2.9}$$

All μ^0 can be summarized as ΔG^0, which is the free energy change at standard conditions. The second term is important because it brings in the concentration dependence. On the other hand, the third term is often omitted although being mathematically inaccurate in cases where the molar units do not cancel out.

$$\Delta G = \Delta G^0 - RT\ln \frac{[A]^a[B]^b}{[C]^c[D]^d} \tag{2.10}$$

For a reversible reaction in an equilibrium state, we again expect the driving force ΔG to become zero, and simplify the equation to

$$\Delta G^0 = RT\,\ln\frac{[A]^a_{eq}[B]^b_{eq}}{[C]^c_{eq}[D]^d_{eq}} = RT\,\ln K_d \tag{2.11}$$

where K_d is the dissociation constant used in practice to describe binding affinities of protein-protein interactions.

In practice we are often looking at simple ligand-receptor interactions, and very quickly start to struggle when it comes to more complex interactions. Nowadays this is mostly due to the limited capability of existing biophysical characterization techniques to differentiate signal from co-existing species. Before the time of numerically solving equations with computers, it was also the lack of analytical solutions for more complicated biological systems, which limited the data analysis. In order to keep it simple at the start of an investigation, it is useful to make several assumptions.[6] They may turn out to be wrong later on, but this is part of a biophysical characterization procedure. In general, we assume that interactions are reversible and that all receptor molecules are equivalent and independent. We also have to make assumptions regarding the reaction rate order (associations are bimolecular, dissociations are unimolecular). Moreover, the measured signal has to be proportional to the number of occupied receptor sites, and the reaction components only exist in a bound and in an unbound state. For measurements of equilibrium states,

we initially assume that our reaction mixture is equilibrated.[6] Evidently, there can be more complex cases which will be identified as such during the data analysis when experimental data deviates from predictions or shows poor fits to models. This is then an opportunity for a biophysicist to conceptualize an appropriate experiment or data analysis to obtain an accurate K_{d}.

Whereas a biophysicist is most likely interested in the accurate determination of a K_{d}, the biochemist would like to know more about the factors which contributed to a specific K_{d}. In interactions of macromolecules non-covalent bonds, such as hydrogen bonds or salt bridges, play an important role.[180] Even though the contributions of individual groups are relatively small, they sum up to significant values in case of interaction interfaces. On such interfaces many groups can contribute simultaneously to the stabilization of a complex.[179] Looking at three different examples of energy values for molecular systems (Table 2.2) helps to put this into a more practical context. A change

Table 2.2: Reference energies for protein-protein interactions

Process	Energy (kJ/mol) at 298 °K
thermal energy (k_BT)	2.5
H-bond for protein in solution[181]	2 to 6
ATP to ADP hydrolysis[182]	38
PPI with $K_{\mathrm{d}} = 1$ μM	34
PPI with $K_{\mathrm{d}} = 1$ nM	51
PPI with $K_{\mathrm{d}} = 1$ pM	68

in K_{d} from 1 μM to 1 nM, corresponds to an energy difference of about 20 kJ/mol, which would correspond to four to ten additional H-bonds. H-bonds are important in stabilizing complexes, but are also environment dependent and can be accompanied by many other factors, such as charge-charge interactions, or increase in entropy, e.g. from releasing bound water at the binding interface of two proteins.[180] One way to access the entropic change induced

by an interaction is differential scanning calorimetry. In these experiments the van't Hoff equation (equation 2.12) is used to extract both the change in standard molar enthalpy ΔH^0S and entropy ΔS^0. Despite being widely used, they are often accompanied by difficulties.[179]

$$\ln K = -\frac{\Delta H^0}{RT} + \frac{\Delta S^0}{R} \tag{2.12}$$

This is the case for many other experimental techniques and in many cases it is therefore not straightforward to measure an accurate K_d and derive a structure-affinity relationship.[183] Next to repeating experiments with site-mutations or employing computational modeling[184] the use of orthogonal analytical techniques is essential.

In this context, going beyond equilibrium experiments and trying to access the kinetics can provide valuable information. In kinetic studies we usually observe a non-equilibrated system on its way to equilibrium, thereby measuring on and off rates of the reaction. In a simplified way, the on rate can be attributed to the probability of two molecules colliding and binding and the off rate as the strength of binding or the probability to unbind. The off rate also provides us with the residence time, defined as $1/k_\mathrm{off}$ in a two-state mechanism. The residence time tells us how long a drug stays bound to its target and is therefore of high relevance in pharmaceutical applications.[14,185–187]

For a 1:1 interaction of a receptor (R) and a ligand (L) we can develop a reaction equation as,

$$R + L \underset{k_{off}}{\overset{k_{on}}{\rightleftharpoons}} RL. \tag{2.13}$$

When the reaction is in equilibrium the change in concentration over time is 0 and can be described by the following differential equation, for the molar concentration $[R]$,

$$\frac{\mathrm{d}[RL]}{\mathrm{d}t} = [R] * [L] * k_{on} - [RL] * k_{off} = 0 \tag{2.14}$$

Re-arranging this equation, allows us to express the binding affinity as ratio of k_{off} over k_{on} and equal to K_{d} as following,

$$K_d = \frac{k_{off}}{k_{on}} = \frac{[R] * [L]}{[RL]}. \tag{2.15}$$

Writing this equation in terms of units, seconds (s) and molar (M), we get

$$K_d = \frac{[R] * [L]}{[RL]} = \frac{M * M}{M} = M \tag{2.16}$$

and

$$K_d = \frac{k_{off}}{k_{on}} = \frac{s^{-1}}{M^{-1} * s^{-1}} = M \tag{2.17}$$

In section 3.4 we show in detail how this approach can be used to extract rate constants from time-course data of a kinetic study. Briefly, we can numerically integrate the differential equation for each reaction component to obtain the time-dependent concentration, e.g. $[\text{R}]_t$ and $[\text{RL}]_t$. We then use the formula describing the ratio $[\text{R}]_t/[\text{RL}]_t$ and fit it to our experimentally obtained $[\text{R}]_{t,exp}/[\text{RL}]_{t,exp}$. From here we extract k_{off} and k_{on}, and can calculate the K_{d} with equation 2.15.

Chapter 3

Development of MP Based Biophysical Characterization Methods

This chapter has been adapted from the following publication: F. Soltermann, E. D. B. Foley, V. Pagnoni, M. Galpin, J. L. P. Benesch,P. Kukura and W. B. Struwe, Quantifying Protein–Protein Interactions by Molecular Counting with Mass Photometry, *Angewandte Chemie International Edition*, 2020, 59, 10774-10779.[155] Reprinted with permission from Wiley. The experiments, data and analysis presented in this chapter were designed, acquired and carried out by myself, where not otherwise noted. Weston Struwe expressed the 2G12 monoclonal antibody used for experiments in Figure 3.1. Erik Foley helped in the development and characterization of the continuous-flow injection system. Veronica Pagnoni helped developing the data visualization for Figure 3.1. The fitting and statistical analysis for the kinetic data shown in Figure 3.11 was developed in collaboration with Martin Galpin and Stephan Burkhalter.

3.1 Introduction

Understanding how biomolecules interact with each other is central to the life sciences. The complexity thereof ranges from specific binary interactions,

such as between antibodies and antigens,[188–190] to the formation of complex macromolecular machines.[191,192] Conversely, undesired interactions are often associated with disease, such as the formation of protein aggregates in neurodegenerative disease,[193] or the engagement of a virus with its target cell.[194,195] The high-specificity and critical role of these interactions make them an ideal target for intervention, either in promoting a certain response by presenting an alternative binding partner, or preventing (dis)assembly.[196–198] This diversity comes with a broad range of binding strengths and dynamics, measured in terms of thermodynamic and kinetic quantities such as equilibrium constants (e.g. for dissociation, K_d), free energies and rate constants (k_off and k_on).

In broad terms, existing biophysical methods can be categorized into size-based approaches performing quantification and separation by size or diffusion coefficient, physical interaction with functionalised surfaces, direct mass measurement, enthalpy changes or light scattering.[199] Single-molecule fluorescence, capable of operating at the single-molecule level, providing additional information on sample heterogeneity and dynamics.[200,201] All of the above methods operate in the context of various practical shortcomings such as non-native environments, artefacts caused by protein immobilization and labelling, lack of sensitivity at low concentrations or low resolution.[76,202,203] Biological systems can pose additional challenges from particularly fast or slow kinetics to complexities arising from multiple co-existing species. Label-free methods struggle with strong binding affinities ($K_\mathrm{d} < \mu$M), which are often encountered for interactions of particular relevance for biopharmaceuticals in the context of antibody-based drugs.[204]

We have recently developed mass photometry (MP), originally introduced as interferometric scattering mass spectrometry (iSCAMS), as a means for detecting and measuring the mass of single proteins and the complexes they

form in solution. MP detects single biomolecules by their light scattering as they bind non-specifically to a microscope cover glass surface. Each binding event leads to a change in refractive index at the glass/water interface, which effectively alters the local reflectivity and can be detected with high accuracy by taking advantage of optimized interference between scattered and reflected light (Figure 3.1a).[3] The magnitude of the reflectivity change can be converted into a molecular mass, for polypeptides with $\sim 2\%$ mass accuracy and up to 20 kDa mass resolution by calibration with biomolecules of known mass.[4] Both the original,[4] and subsequent studies have proposed methods to extract binding affinities from MP distributions of biomolecular mixtures,[157] and shown that the obtained affinities agree broadly with alternative approaches.[4,156,157] The degree to which these MP distributions are indeed quantitative, and how they can be used to efficiently extract not only binding affinities but also kinetics, however, remain unexplored.

3.2 Results and Discussion

3.2.1 Stoichiometry and Relative Abundances

Label-free single-molecule detection in principle provides the purest and most direct measurement of sample concentration by counting individual molecules. To explore the capability of quantifying relative abundances of co-existing biomolecules in a sample we chose the monomers and domain exchanged dimers of the HIV-1 neutralizing antibody 2G12 (Figure 3.1a).

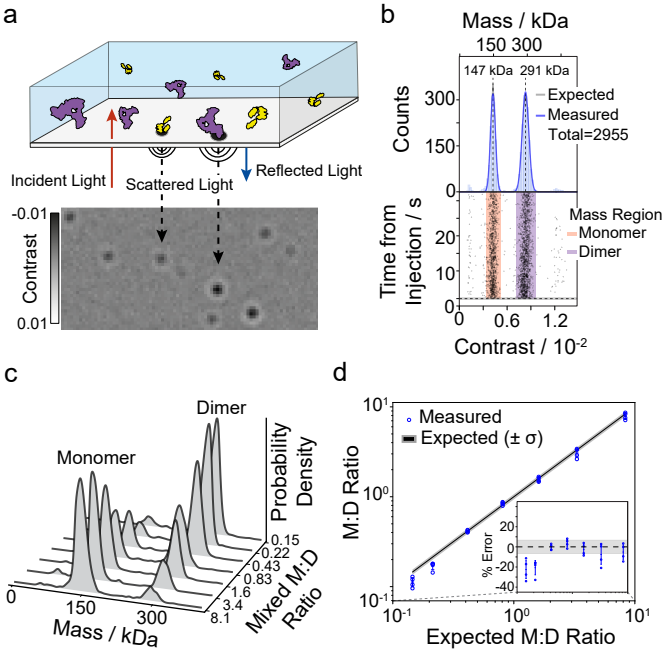


Figure 3.1: Principle of single-molecule counting by mass photometry. (a) Label-free single-molecule detection by imaging the interference of scattered and reflected light arising from individual protein landing events at a glass-water interface over time. (b) Scatter plot of single-molecule contrasts and resulting mass distribution for a 1:1 monomer:dimer 2G12 mixture. (c) Mass distributions for varying 2G12 monomer:dimer ratios. (d) Comparison of monomer:dimer ratios measured by MP compared to expectations based on UV-VIS absorption characterization.

The 2G12 antibody was selected for bench-marking because a monomer and a dimer specie could be expressed and purified with good yields and high purity. These two species were shown to not interact with each other, i.e. pure monomer did not form dimers and pure dimer did not form monomers. This allowed us to prepare custom-made monomer/dimer mixtures with the help of UV-VIS based concentration measurements. In this way mass distributions with the expected major bands at 147 kDa and 291 kDa (Figure 3.1b) could be obtained with MP and compared to UV-VIS based characterization. In Figure 3.1c we show these experiments for monomer/dimer ratios ranging from 0.15 to 8.1. Comparison with UV-VIS-based measurements revealed a close agreement within the experimental error (4.6% RMS), except for noticeable

deviations (∼20%) for the lowest ratios (Figure 3.1d). We found that such deviations could almost exclusively be attributed to sample preparation, such as an additional dilution step of the 2G12 monomer stock solution, required to reach sub-nM concentrations in the samples with a low monomer/dimer ratio. This led to variations in counts arising from non-specific protein adsorption to the sample tube (see more in Section 3.2.2). Additional to the sample preparation we investigated various other parameters which could influence the relative abundances in the MP experiments. Ultimately this helped to define the experimental procedure necessary for accurate measurements of relative abundances as shown in Figure 3.1. In Table 3.1 we show an overview of the parameters which we addressed in our bench-marking process.

Table 3.1: Comment on factors with potential influence on relative abundances

Factor	Comment
Non-specific binding of protein to coverslip glass	Valid for wide range of proteins[4]
Non-specific adsorption of protein to sample vial	Problematic at sub μM concentration[155]
Protein diffusion during acquisition	Correction via molecular weight dependence of diffusion coefficient[4,155]
Impurities in "pure" stock solutions	Measure pure samples before interaction experiments[155]
Detection efficiency of image analysis	Work in appropriate concentration range[155]
Reversible binding of protein to coverslip glass	Observed for extreme pH values or strong laser powers
Molecular weight resolution	Peak width ca. 10% of molecular weight
Molecular weight detection limit	40 and 70 kDa for qualitative and quantitative measurements respectively

A major concern, the non-specific binding of proteins to the coverslip glass,

was already assessed and shown to be valid for a wide range of proteins in the publication of Young et al.[4]. Moreover, any deviations from these findings becomes directly evident during each experiment if the measured counts deviate significantly from expected counts deduced from UV-VIS measurements.

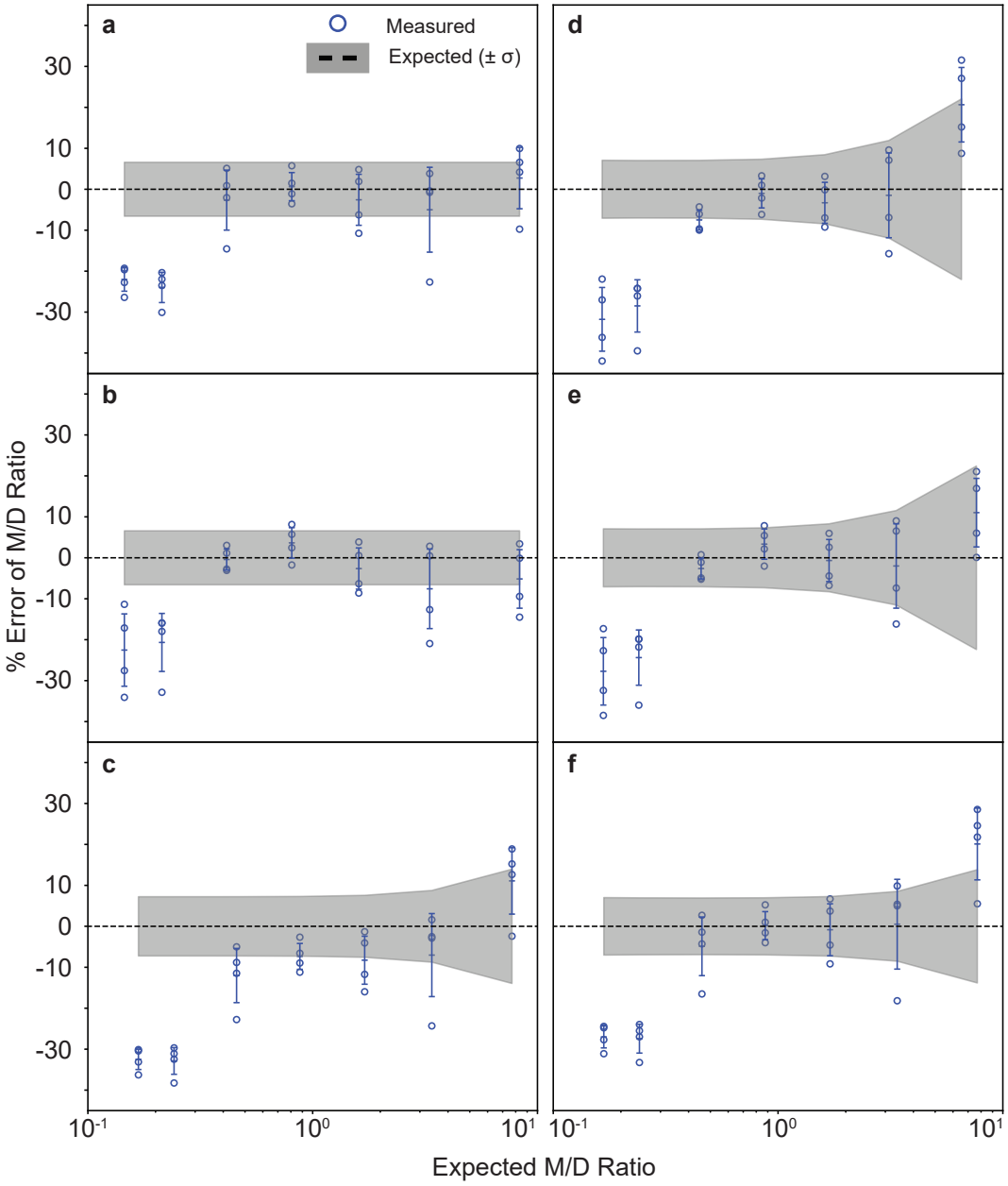


Figure 3.2: Data analysis approaches for 2G12 monomer/dimer ratios using gaskets. We tested the influence of data acquisition duration, diffusion correction ($MW_{-1/3}$) and correcting for minor impurities. (a) No corrections, 90 s acquisition time. (b) No correction and 30 s acquisition time. The combination of accurate results, not needing to apply correction and having the highest time resolution were the main reasons to use method (b) in our work. (c) 90 s acquisition time and correction for minor impurities from control experiments of pure monomer, dimer and trimer. (d) 30 s acquisition time and correction for minor impurities from control experiments of pure monomer, dimer and trimer. (e) 90 s acquisition time and correction for minor impurities from control experiments of pure monomer, dimer and trimer and diffusion correction. (f) 30 s acquisition time and correction for minor impurities from control experiments of pure monomer, dimer and trimer and diffusion correction.

Looking at the M/D ratios and their dependence on time delay between injection and acquisition start and the acquisition duration helped us to get insight into the effect of diffusion on relative abundances, when using gaskets as injection systems (Figure 3.2). Additionally, we included corrections for minor impurities in pure monomer and dimer samples. We concluded that acquisition duration and diffusion correction have only limited influence on the M:D ratio when the time between sample injection and acquisition start is kept minimal (ideally below 5 s) and measurement time is around 30-90 s, coinciding with a significantly lower landing frequency. The impact of diffusion corrections is expected to be even lower when looking at species with smaller MW differences. Corrections for minor impurities in pure monomer and pure dimer stayed negligible, thanks to the high purity of the samples. However, one should be cautious especially when mixing compounds in extreme ratios. As an example: Operator X wants to probe the binding affinity of specie A (150 kDa) and specie B (75 kDa) and mix them together. The operator decides to mix them in a 1:10 ratio, in the hope to enhance the formation of complexed species. Unfortunately, "pure" B contains a dimer at 150 kDa as minor impurity of 5%. If A and B are mixed 1:10, this minor impurity suddenly makes up 50% of the 150 kDa peak. This can be even more extreme, if the binding affinity of A and B is strong and most of A binds to B. In such a case the peak around 150 kDa would consist of almost 100% of the dimer impurity of B. Therefore, it is essential to assess purity and composition of the pure compounds, and account for it in binding affinity measurements which go beyond a yes/no answer, i.e. where a K_{d} is measured.

Having taken non-specific binding to the coverslip glass, sample preparation, impurities and diffusion into account, we have one more parameter to look at: spot-detection efficiency of the image analysis software. Therein we were

particularly interested in any bias for low or high molecular weight species. We made the crude hypothesis that the image analysis, an automated spot-detection algorithm is limited in the same way as the visual spot-detection by eye. In other words, in an image where landing events start to overlap, we struggle to identify every single landing event and we expect the algorithm to struggle in the same way. This parameter is therefore directly related to limits of the concentration range. We did not expect to see a sharp concentration threshold for this phenomenon, but rather a gradual process. At high concentration/ high landing event density we expected a bias towards larger species. These trends were experimentally supported in Figure 3.3, where we see that the M/D ratio is increasingly underestimated when going to higher concentration.

Next to the bias of the M/D at high concentration when using gasket injection we show that the continuous flow injection shows a bias for low MW species. The continuous-flow approach was applied when working at concentrations below 1 nM to ensure sufficient counts. These videos are characterized by low number of counts per image and are therefore expected to be reliably analyzed by the spot-detection algorithm. In contrast to gaskets, where we have a static solution standing over the field of view and basically performing a pull-down assay, the continuous flow constantly delivers fresh solution to the field of view, thereby favoring molecules which more frequently hit the glass surface. Thanks to their larger diffusion coefficient, which is MW dependent ($MW^{-1/3}$), lighter molecules will be detected more often. Therefore, counts obtained with a continuous-flow injection system must be diffusion corrected (Figure 3.3, blue and red).

In conclusion, we found that the experimental procedures have to be carefully designed when working at sub-µM concentrations (e.g. when adding dilution steps) because of non-specific adsorption of protein to sample tube

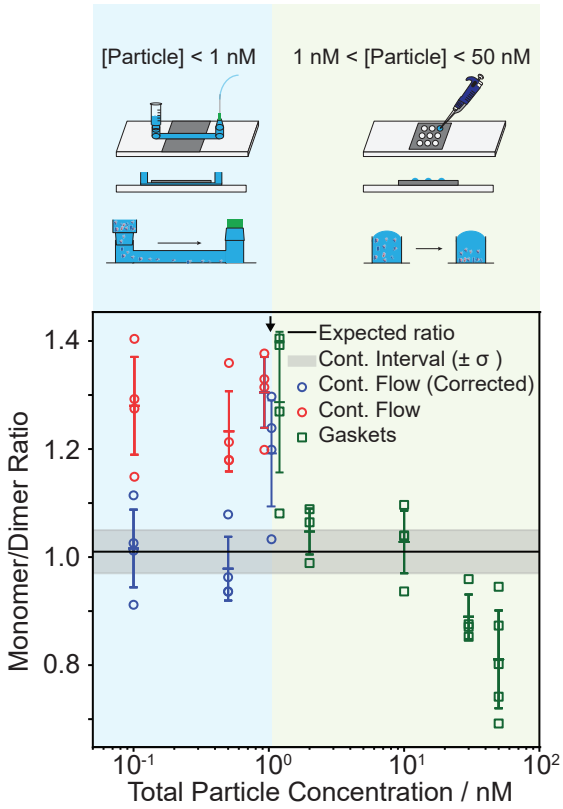


Figure 3.3: Dynamic range estimation, sample carriers and diffusion correction. Experimental setup for continuous flow chambers (top, left) and silicone gaskets (top, right). MP ratio measurements of a 1:1 mixture of 2G12 monomer and dimer at different dilutions (0.1, 0.5, 1, 1, 2, 10, 30, 50 nM). The three results for 1 nM solutions were separated horizontally (arrow) to improve readability. Diffusion-corrected continuous flow ratios (blue) where obtained by normalizing monomer and dimer counts to their corresponding molecular weight dependent factor in the diffusion coefficient ($MW^{-1/3}$). The expected ratio (1.04 ± 0.05, black) was determined from UV-VIS measurements of concentrated (μM) stock solution of the pure monomer and dimer as well as weighing monomer and dimer stock solutions on a microbalance. These experiments were conducted to probe the dynamic range, suggesting that we can accurately measure ratios for samples with particle concentrations below 50 nM and extending the dynamic range to sub-nM concentrations when going from gaskets to a continuous-flow injection system. In the case of the continuous flow system we observed an influence of diffusion on our monomer:dimer ratios, which is expected to be molecular weight dependent ($MW^{-1/3}$). No influence was observed when conducting the experiments with gaskets when time between sample introduction and data recording was minimized (delay time <5 s) (Figure 3.2).

surfaces. Moreover, the concentration range in which we can accurately quantify relative abundances is limited to up to 50 nM total particle concentration when

working at a frame rate of 956 Hz and with 5-fold frame pre-binning and 7-fold frame binning during image analysis. In the case of our injection procedure with gaskets, we show that sample diffusion has minor effects on the 2G12 monomer:dimer ratio. Contrarily, when using a continuous-flow system for injection the counts should be diffusion corrected. We also explained that minor impurities should be quantified when working at extreme ratios of analyte and binding partner or when attempting to quantify a K_{d}.

Finally, these findings justify the experimental procedures and methods applied in experiments shown in this thesis, starting with the accuracy of M/D ratios of the 2G12 antibody in Figure 3.1. In a next step, we would like to elaborate a bit more the challenges and potential solutions when handling samples at sub μM concentrations.

3.2.2 Working at sub-μM Concentrations

We just showed that the current dynamic range for concentrations in MP experiments is below 50 nM. Even though most steps of the sample preparation can be done at concentrations at μM or above, this means that we ultimately have to dilute our samples down to the nM or even pM range. Small relative sample losses at μM concentration due to non-specific adsorption to the sample tube surfaces could mean large absolute sample losses when working at three orders of magnitude lower concentrations. Adhesion of biomaterials to solid surfaces is a common phenomenon and known to create severe problems in various fields, including bioanalytics. In bioanalytics it is particularly problematic when working below μM concentrations and many approaches have been developed and tested to make surfaces more protein repellent.[205–207]

To briefly summarize this research: different proteins and even different portions of a protein behave differently when it comes to interactions with a surface.

Therefore, there is no generally applicable method to completely prevent such interactions for all proteins. What we could observe is that non-specific adsorption is dependent on sample tube material, protein and incubation time. It can lead to almost complete sample loss in case of a 5 nM antibody solution stored for 20 hrs in a PCR tube (Figure 3.4a) or only ca. 50% loss when storing the same sample in a normal Eppendorf tube (Figure 3.4b).

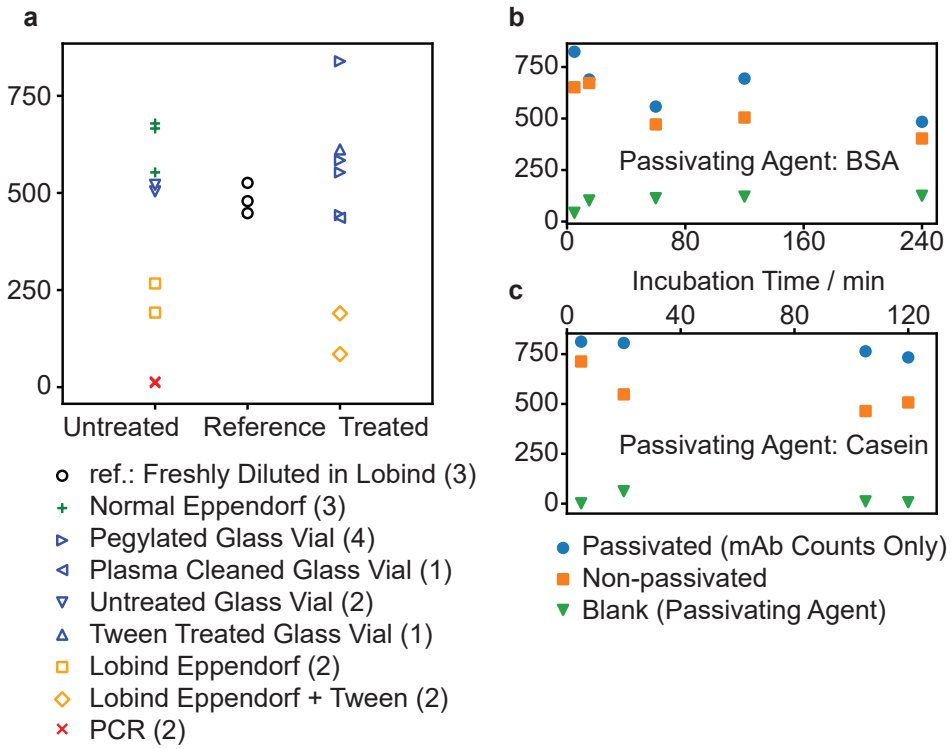


Figure 3.4: Non-specific adsorption and sample tube passivation. Non-specific adsorption comparison of different sample tubes by quantifying counts of a 5 nM trastuzumab solution after 20 hrs incubation. Recovery for a passivated (circle) and a non-passivated (square), normal Eppendorf tube (a). The passivation protocol with BSA (b) did not show an effect, passivation with casein (c) improved recovery of trastuzumab.

We hoped to further improve the recovery in normal Eppendorf tubes by passivating them with BSA prior to usage (see passivation protocols in section 3.4.5). Unfortunately, BSA proofed to be unsuitable for our MP compatible passivation protocol because it did not prevent loss of antibody (Figure 3.4b)

and directly interfered with our experiments by generating counts in the MW-region below 120 kDa. In contrast, the passivation with a hardly water-soluble protein (casein) prevented non-specific adsorption of antibody, even with long incubation times. Furthermore, the low MW of casein is compatible with MP experiments, when present in minor quantities (Figure 3.4c). We suggest that casein stays adsorbed to the sample vial surface due to its low solubility in water and therefore prevents adsorption of better water-soluble proteins, such as antibodies. While casein passivation showed to be very effective, this protocol added an additional workload, which was not compatible with our bench-marking process where large number of samples and experiments had to be processed. For practical reasons we decided to run our experiments without casein passivated sample tubes. Based on our findings we avoided Eppendorf Lobind and PCR tubes and chose normal Eppendorf tubes.

Having addressed limitations which are under control of laws of nature in the first two sections of this chapter, we now want to focus on things which are more under our control. In the next section we addressed pitfalls during data acquisition and processing and show how they can be identified and avoided.

3.2.3 Data Quality Control

Over the course of this project, we have been striving for improving the differentiation between "good" and "bad" quality data, ultimately enabling measurements with consistent and optimal molecular weight resolution. In this process, we were able to identify critical parameters to look out for when planning, performing and trouble-shooting an MP experiment (Table 3.2). This list is non-exhaustive and will need adjustments in the coming years when more people discover new challenges and new solutions thereof. With the current instrumentation and software available we recommend to briefly look at each

Table 3.2: Parameters, indicators and potential sources for impaired data quality

Parameter	Indicator	Potential sources
Out-of-focus measurement	Inversed contrast or anomalous PSF of particles in ratiometric image or no counts	Wrong focus position, field of view and illumination profile are not aligned
Unstable focus	Focus voltage is drifting	Excessive immersion oil between stage and coverslip, or stage perturbed by airflow
Drifting Image SD	Drifting image SD but stable focus voltage	Cold/hot sample injected
Rough/irregular glass surface	Large interfering black dots in native image	Insufficient quality control during glass cleaning procedure
Unbinding events	Particles with negative contrast values	Unsuitable pH, unsuitable glass surface properties (test APTES coating) or overloaded the glass surface by injecting too much protein
Buffer impurity or aggregation	Large particles floating around and causing interferences in the ratiometric image	Buffer or sample not filtered suitably (i.e. 0.22 μm filter), sample is precipitating under chosen conditions
Too high concentration	Landing events are overlapping in time and position	Insufficient dilution, camera frame rate too slow

video individually, ideally during acquisition or otherwise during data analysis. Videos which meet one of the criteria listed in Table 3.2 should be discarded. As part of the data analysis we recommend applying an xy-distance constraint filter to all confirmed counts, excluding particles which were recorded at the same xy-position in the field-of-view. This helps to exclude "blinkers" (i.e. fast

binding and unbinding events at the same position) and significantly lowers the baseline noize. For gasket injection experiments, we recommend to plot the counts as a detection rate ($-\Delta$counts/Δt) of the measured species X vs. time. The resulting decay curve should follow a single exponential decay, which indicates an error-free experiment. We experienced deviations from a smooth decay when one or several of the criteria in Table 3.2 were met.

Knowing general, as well as data processing related limitations of MP eventually enabled us to design experiments to more quantitatively explore biological system. Specifically we hoped to make progress in quantifying binding affinities and kinetics of protein-protein interactions.

3.2.4 Binding Affinity and Kinetic Measurements

Equipped with these bench-marking results, we set out to investigate the suitability of MP to characterize protein-protein interactions of varying affinities, using the immunoglobulin G (IgG) monoclonal antibody trastuzumab (Herceptin®) binding to soluble domains of IgG FcγRs or ErbB2 (HER2) antigens. In a first step, we looked at the purity and potential oligomerization of the pure compounds, as outlined in the MP screening in Figure 3.5. Trastuzumab, herein referred to as IgG, and FcγRIa by themselves revealed monodisperse distributions at 154 ± 1 kDa and 50 ± 1 kDa, respectively (Figure 3.6a). A 1:1 FcγRIa-IgG mixture resulted in a large IgG-FcγRIa complex peak, corresponding to $\sim$ 90% complex formation, from which we can extract an apparent K_{d} = 50 ± 10 pM by counting bound and unbound species in combination with knowledge of the total protein concentration (more information in section 3.4). IgG N-glycan removal (Figure 3.19) weakened FcR binding[208] resulting in a 1:1 mixture of FcγRIa and deglycosylated IgG exhibiting considerably less bound antibody ($\sim$ 50%) (Figure 3.6b), corresponding to an apparent K_{d} = 1.0 ± 0.1

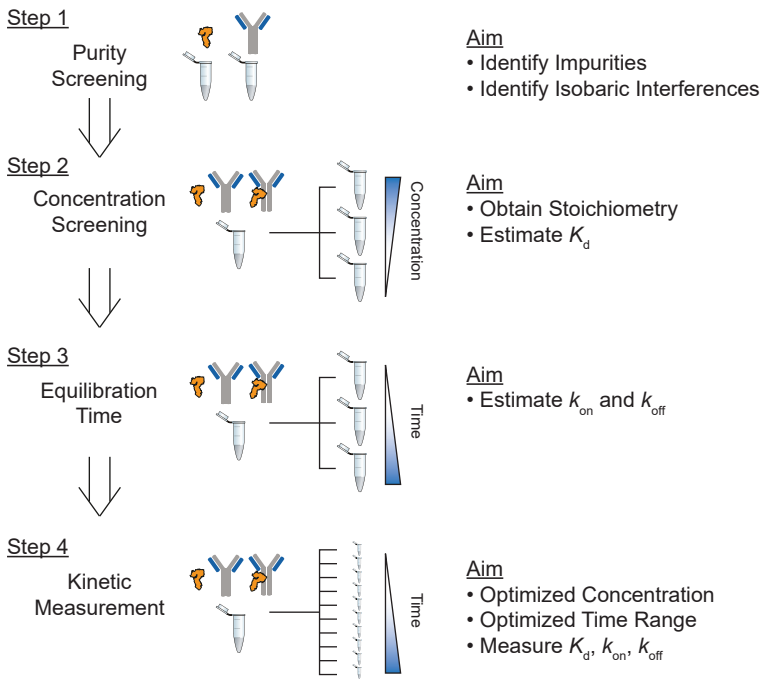


Figure 3.5: Screening method for the quantification of impurities, stoichiometry, binding affinities and kinetics of protein-protein interactions with MP. With Step 1 and 2 we can obtain an estimate for the K_d of the interaction, as well as impurities and stoichiometry. Step 3 and 4 are used for a more in-depth analysis with the aim to quantify and confirm binding affinities and kinetics of the interaction.

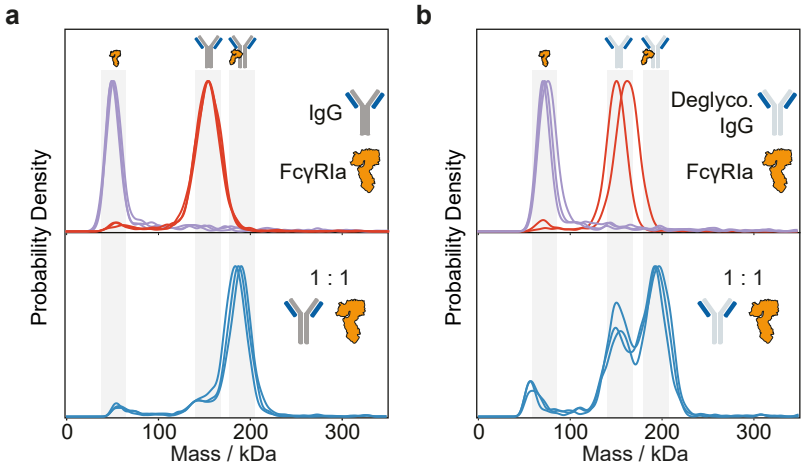


Figure 3.6: Single-shot K_d of IgG-FcγRIa interactions. (a) MP mass distributions of IgG (red), FcγRIa (purple) and a 1:1 mixture of IgG-FcγRIa (blue). (b) MP distributions of deglycosylated IgG (red), FcγRIa (black) and 1:1 mixture of IgG-FcγRIa (blue)

nM, This simple single-shot approach presented so far, however, necessarily neglects the importance of kinetics and equilibration conditions. To address this, we probed FcγRIa binding to deglycosylated IgG at a 1:1 ratio. Samples were mixed as 4 µM, incubated for 15 minutes and diluted to 5, 1 and 0.3 nM final protein concentrations (Figure 3.7a and 3.5).

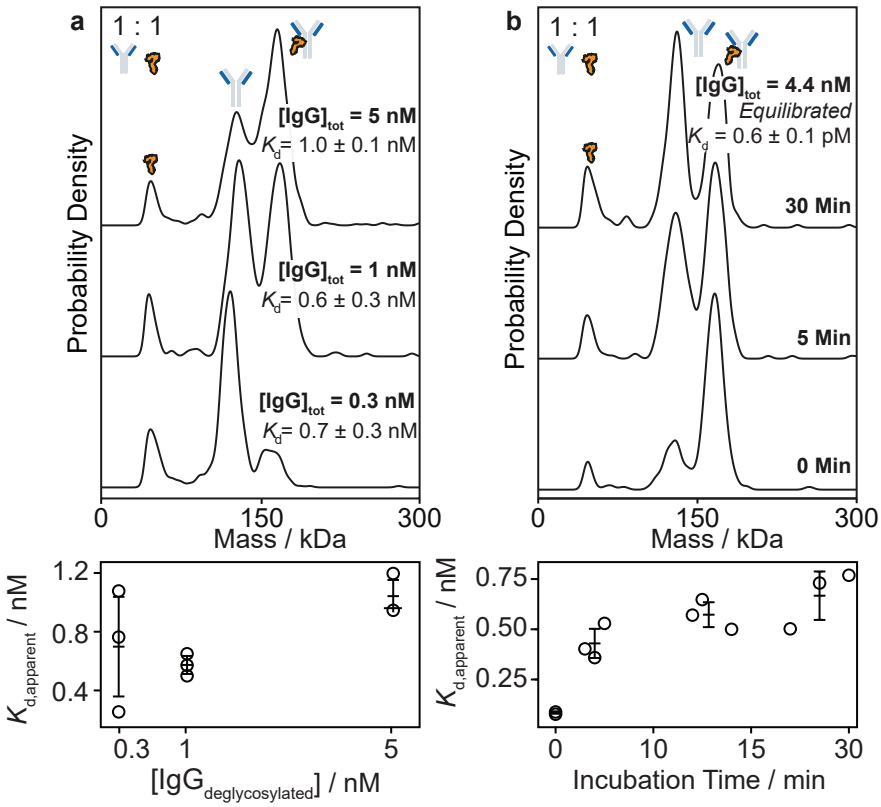


Figure 3.7: K_d screening of deglycosylated IgG-FcγRIa. (a) Mass distributions for a 1:1 mixture of deglycosylated IgG-FcγRIa at total IgG concentrations ranging from 300 pM to 5 nM. (b) Mass distributions for a 1:1 mixture of deglycosylated IgG-FcγRIa at 1.5 nM total IgG concentration, ranging from 0 to 30 minutes after dilution from 2.9 μM.

At concentrations above the K_d we found mostly bound complexes, with free species dominating below the K_d, but all measurements providing similar binding affinities (K_d =1.0 ± 0.1, 0.6 ± 0.1 and 0.7 ± 0.3 nM), suggesting that they were performed at or close to equilibrium (Figure 3.7a). These binding affinities were confirmed after equilibration time screening (Figure

3.7b). Specifically, for FcγRIa binding to deglycosylated IgG, shifts in peak intensities were observed during the concentration screening, indicating that we should be able to observe the time dependence of these interactions. Starting from apparent K_{d} values of 0.09 nM after 0.4 min incubation time we can observe a gradual increase over time, until we start to reach a plateau-region after ca. 10 min, suggesting a $K_{\mathrm{d}} = 0.6 \pm 0.1$ nM. These measurements revealed that equilibrium was reached after 10 minutes, yielding $K_{\mathrm{d}} = 0.6 \pm 0.1$ nM (Figure 3.7b).

For quantification of the tighter interaction between FcγRIa and IgG, the herein described K_{d} screening method was essential to avoid misinterpretation of single-shot K_{d} measurements. Measuring the FcγRIa-IgG sample at different concentrations (Figure 3.8a) gave us a first estimate of the strength of the interaction (K_{d} $\sim$100 pM). Based on this information we could then perform an equilibration time screening to estimate the underlying kinetics (Figure 3.8b). Starting with an apparent K_{d} value of 200 fM after 2 min, K_{d} values are reaching a plateau-region after $>$ 80 min incubation time, with K_{d} values between 60-100 pM.

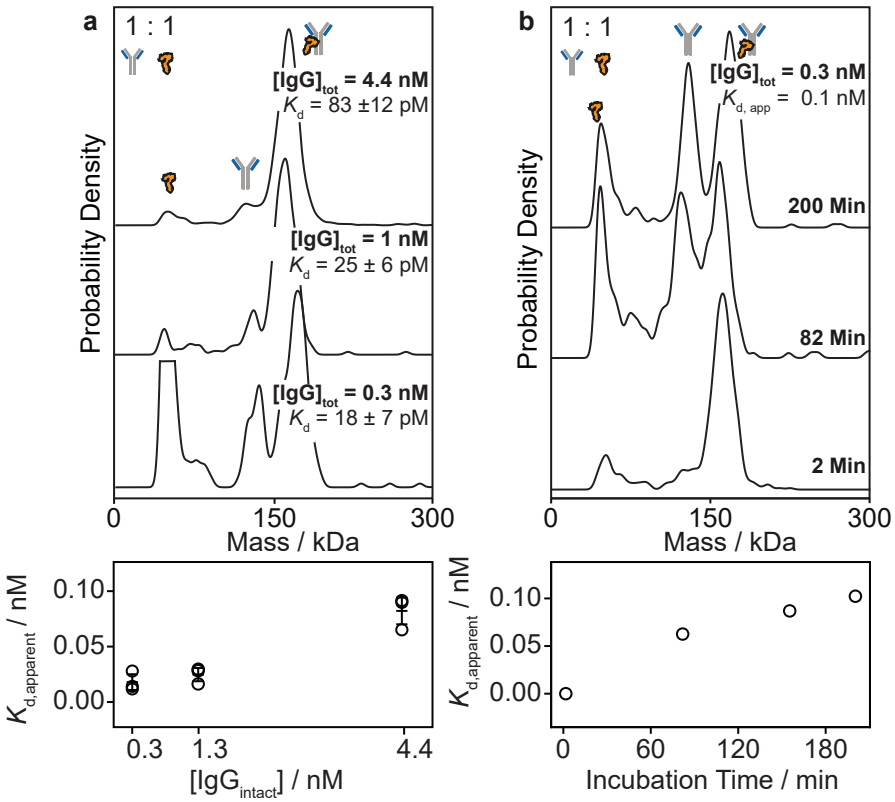


Figure 3.8: K_d screening of IgG-FcγIa complexes. (a) MP measurements at different total concentrations (4.4, 1 and 0.3 nM). (b) Equilibration time screening at a concentration where complexed and free species can be observed, measured 2, 82 and 200 min after dilution.

As an additional example for the importance of this screening protocol, we show the binding affinity measurements of the HER2-IgG interaction. A simple single-shot measurement would have led to a $K_{d,1} = 1.4 \pm 0.1$ nM and $K_{d,2} = 4.8 \pm 0.3$ nM (Figure 3.9). By simply recording distributions at a few different concentrations, however, we could reveal a linear dependence of our K_d values on concentration, indicating a very tight $K_d < 70$ pM, and/or slow interactions with off-rates on the order of hours, suggesting that this interaction exceeds the current dynamic concentration range/sensitivity of MP (i.e. sub-pM K_d). Therefore, performing a few measurements at a range of concentrations is crucial to prevent misinterpreting data derived from a single-shot K_d approach for very strong interactions. Irrespective, our method provides rapid and clear

distinction between interactions with vastly different binding affinities, which only need to be refined if highly accurate measurements are required.

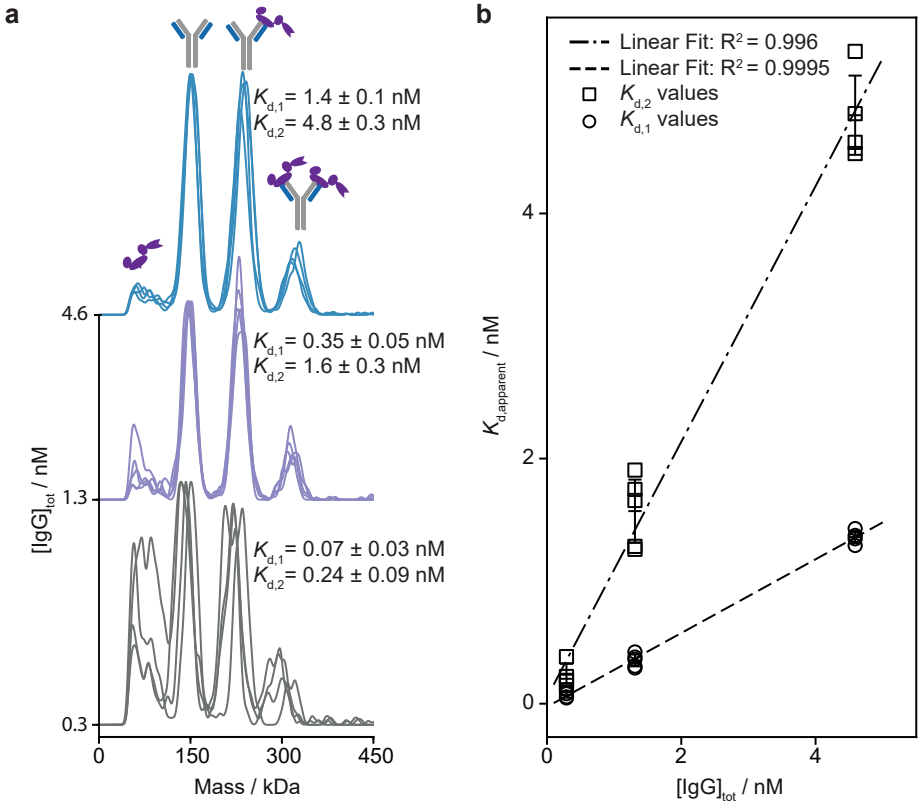


Figure 3.9: Screening of trastuzumab-HER2 interaction. (a) K_d screening at different concentrations, with no change in bound/unbound ratio. (b) Strong linear dependence on concentration of the measured apparent K_ds, indicating non-equilibrium conditions and/or K_d values, suggesting that this interaction exceeds the current dynamic concentration range/sensitivity of MP (i.e. sub-pM K_d).

The importance of (dis)association rates in addition to thermodynamic quantities raises the question to which degree we can use MP to directly visualize and quantify interaction kinetics. As MP measurements currently take place in the <100 nM concentration range, we should be able to access dissociation kinetics by simply diluting to total protein concentrations around the estimated K_d (approx. 1:1 ratio bound: unbound species for a 1:1 interaction), and monitoring the bound:unbound ratio throughout (Figure 3.10a).

The observed exponential decay reveals the desired kinetic information,

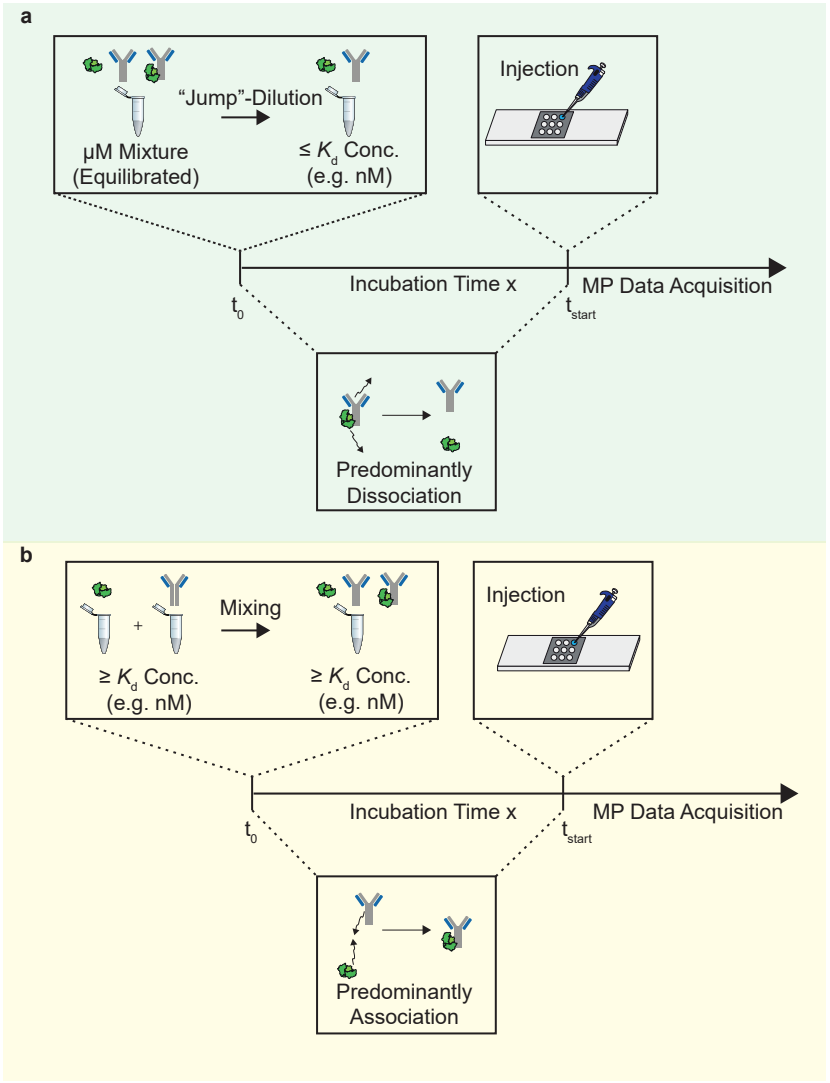


Figure 3.10: Principle of dissociation and association measurements. (a) Jump-dilution strategy for measuring K_d and kinetics. Dilution to sub-K_d concentrations results in dissociation of protein complexes over time (from t_0). After incubation time t_{start} we quantify the bound to unbound ratio with a MP measurement, typically lasting 30 s (for gaskets). (b) Mixing at concentrations above the expected K_d, in association experiments permits the quantification of complexes that form from t_0. Importantly, non-specific protein adsorption is a factor in both methods, but more noticeable for association measurements.

while the plateau yields the K_d, ultimately enabling us to determine k_{off}. For FcγRIa binding to deglycosylated IgG, this approach yielded $k_{off} = 1.1 \pm 0.2$ nM (Figure 3.11a) in good agreement with our single-shot measurements (Figure 3.7), $k_{on} = 6.0 \pm 1.7 \times 10^6$ M^{-1} s^{-1} and $k_{off} = 6.8 \pm 1.6 \times 10^{-3}$ s^{-1}. The

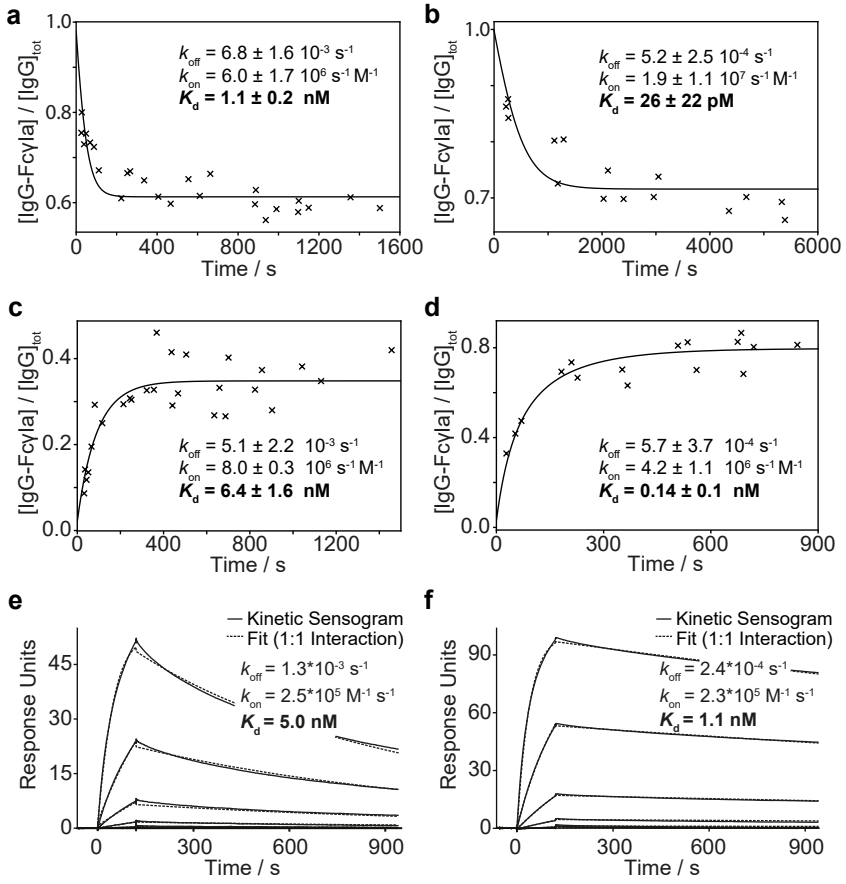


Figure 3.11: Kinetic measurements of FcγRIa binding to intact and deglycosylated IgG. Kinetic measurements of FcγRIa binding to deglycosylated IgG (a, c and e) and FcγRIa binding to glycosylated IgG (b, d and f). The first 4 panels show MP data (a, b, c, d), the last two panels show control experiments with SPR (e,f).

corresponding experiment with glycosylated IgG-FcγRIa yielded $K_{\mathrm{d}} = 26 \pm 22$ pM with an off-rate one order of magnitude slower (5.2 ± 2.5 x 10^{-4} s^{-1}) than for deglycosylated IgG but an almost identical on-rate (1.9 ± 1.1 x 10^{7} M^{-1} s^{-1}) (Figure 3.11b), again in good agreement with our single-shot screening data (Figure 3.8). The difference in K_{d} between the glycosylated and deglycosylated IgG originates mostly from the off-rate caused by protein-protein interactions (Figure 3.12), confirming that the glycans are critical for tight binding.

Association measurements (Figure 3.10b) can in principle be used in an

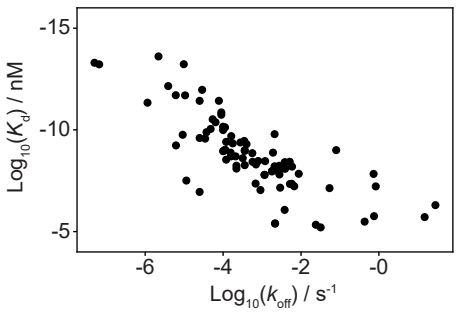


Figure 3.12: Correlation of published K_d vs k_{off} values. Various biomolecular interactions measured by orthogonal techniques (e.g. SPR, BLI). Data used to generate this figure is available in Soltermann et al.[155]. These data show a general correlation between stronger binding affinities corresponding to slower k_{off} rates.

analogous fashion, although we found it more susceptible to protein loss due to non-specific adsorption (Figure 3.11 c,d). Overall, our results were in good agreement with SPR measurements (3.11 e,f), subject to on-rate variations expected from a matrix and surface-immobilization based approach compared to ours, where all interactions take place in free solution (Figure 3.13).

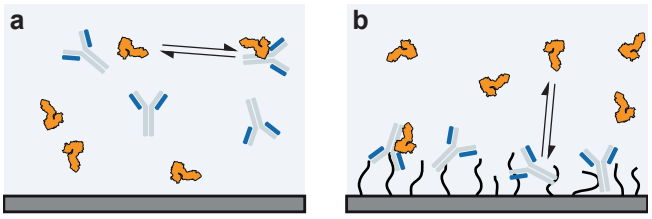


Figure 3.13: Schematic of interactions in MP and SPR. (a) In-solution, label-free interactions occurring in MP. (b) Surface-immobilization (e.g. in a dextran matrix) and associated interactions in SPR. Differences in on-rates between SPR and MP (Figure 3.11) are attributed to mass transport, protein immobilization (i.e. orientation of IgG) and matrix effects.[202] Lower experimental on-rates, therefore, lead to greater calculated K_d values by SPR.

A key advantage of MP over ensemble-based approaches is the ability to distinguish directly between different species contributing to a multicomponent system, as given by the IgG-FcRn (neonatal FcR) interaction involving as many as five different interacting species. FcRn regulates serum IgG half-life and transcytosis to the fetus via a pH gradient in endosomes, yet the interplay between self-assembly and IgG binding is disputed[209,210], which are

both important factors in biotherapeutic design. Based on the existing literature we based our calculations on the independent free monomer binding model (Figure 3.14c).

At pH = 5 FcRn formed monomers and dimers with a $K_d = 31 \pm 11$ nM (Figure 3.14 and Supplementary Figure 27 in[155]). At pH = 5.5 and pH = 6,

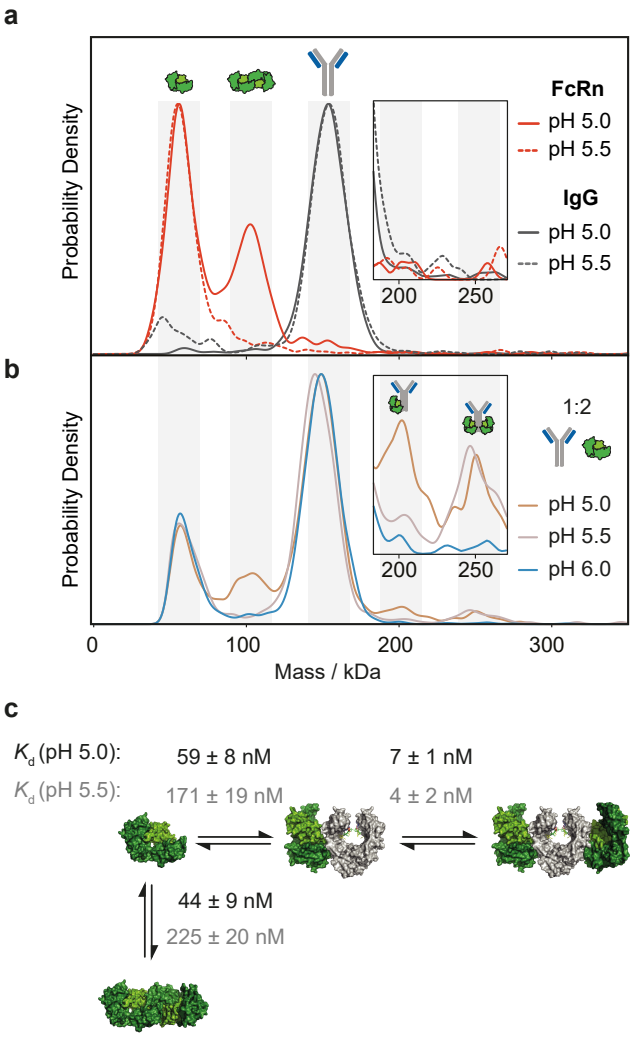


Figure 3.14: Binding stoichiometry and affinity of the IgG-FcRn interaction as a function of pH. (a) Self-assembly of FcRn dimers at pH 5 (red) and 5.5 (dotted red) and equivalent pH measurements of IgG at pH 5 (grey) and 5.5 (dotted grey). (b) IgG-FcRn complexes (1:1 mixture) at pH 5, 5.5 and 6. (c) Associated pH dependent binding affinities of interaction revealing cooperativity in FcRn binding (PDB: 4N0U, 3FRU).

only negligible amounts of FcRn dimers were present with a FcRn monomer-dimer K_d >200 nM (Figure 3.14a). The resulting K_d values for the IgG-FcRn interaction, at pH 5, were 44 ± 9 nM for the monomer-dimer equilibrium, 59 ± 8 nM for the IgG-FcRn monomer and 6.6 ± 0.6 nM for IgG plus two FcRns (3.14b and equations 3.7-3.18). Increasing the pH to 5.5 decreased the binding affinities to 171 ± 19 nM and 225 ± 20 nM but did not significantly affect the binding affinity of IgG plus two FcRns of 3.9 ± 1.5 nM (Figure 3.14 b, c), contrasting SPR results for similar systems reporting an ensemble K_d = 760 ± 60 nM for all interactions.[210] At pH = 6 and 7, our current sensitivity only allowed for an estimate of the binding affinities to be K_d >200 nM (Figure 3.14b). These results highlight pH-dependent FcRn dynamics and IgG engagement, and reveals cooperativity where the second receptor binds IgG tighter than the first and with a weaker pH sensitivity.

3.3 Summary and Outlook

Taken together, we have demonstrated that molecular counting with MP is sensitive, quantitative and accurate in determining the relative abundances of different biomolecules and their complexes in solution. When implemented in the vicinity of the binding affinity, a single measurement lasting typically 30 s, or 240 s for continuous flow injection, yields accurate binding affinities spanning four orders of magnitude from 30 pM to 200 nM, while enabling kinetic probing with a time-resolution on the order of 30 s in the range of minutes to hours. As a result, MP affords real-time assessment of (dis)assembly completely label-free and independent of protein immobilization to a surface, minimizing any possible perturbations, as well as being intrinsically sensitive to binding stoichiometries and oligomerization. The current limitation to sub-μM affinities and concentration range can be addressed in the future by combination

with fluidic approaches[211], as well as improvements to hardware and software, with which we expect to reach the µM range in the near future. This will enable measurements up to 100 μM affinities, making MP a powerful approach for characterizing biomolecular interactions without labels and single-molecule sensitivity in a minimally perturbative fashion. Furthermore, the applicability of MP to both nucleic acids[165] and large multi-molecular machines[162] provides scope for MP becoming a universal tool for studying biomolecular interactions and dynamics in a rapid, label-free and yet single-molecule sensitive fashion.

3.4 Methods

3.4.1 Synopsis

We first characterized all compounds separately by MP to assess their oligomeric composition, following the method outlined in Figure 3.5. Subsequently, we prepared stoichiometry-dependent mixtures of analyte and binding partner (1:1 or 1:2) at μM concentration and equilibrated at room temperature overnight. The samples were then diluted to concentrations near the expected K_d value and equilibrated during a time FcγR before conducting a concentration screening. In these experiments we set the equilibration time to $t = 15$ min and measured the sample at three different dilutions (0.3 nM, 1 nM, 5-50 nM) to obtain an estimate of the K_d and, most importantly, to confirm that complexes are dissociating upon dilution, i.e. the signal corresponding to the biomolecular complex decreases in relative intensity (Figure 3.7 and 3.8). If complexes do not dissociate upon dilution, i.e. relative peak intensities are not changing, the biomolecule interaction is likely to exhibit very tight binding affinities (Kd < 0.1 nM) and/or slow kinetics (> 5 hrs) (Figure 3.9) possibly beyond the dynamic range and sensitivity of the current MP instrumentation. Provided the K_d screening was successful, we proceeded with the kinetic studies for

which we diluted the sample to a concentration around the estimated K_{d}. After dilution/mixing we followed dissociation/association of the biomolecular complex by acquiring individual MP measurements at different time points. From these experiments, we obtained K_{d} values and on-and off-rates. With the current dynamic range we can inject concentrations from 100 pM to 50 nM, and thus quantitate binding affinities ranging from 10 pM to 300 nM and measure kinetics ranging from a few minutes to several hours.

3.4.2 Materials and Sample Preparation

The 2G12 antibody was expressed and purified as described previously.[212] Briefly, plasmids encoding 2G12 antibody heavy and light chains were transiently expressed in HEK 293F at a cell density of 1×10^6 cells/mL with a 1:2 construct ratio (heavy to light chain). After 5 days, cells were pelleted and the supernatant was loaded onto a HiTrap Protein A column (GE Healthcare) following the manufacturers protocol. The binding buffer was 20 mM sodium phosphate, pH 7.5, and the elution buffer was 0.1 M citric acid, pH 3. Antibodies were immediately neutralized with 1 M Tris-HCl, pH 9, prior to buffer exchange into phosphate buffered saline (PBS) (Gibco® DPBS) using a 50 kDa cut-off spin filter (Vivaspin, Sartorius). Antibody oligomers were then separated with size exclusion chromatography (HiLoad Superdex 16/600 200 ps, GE Healthcare) and fractions were collected according to the SEC profile and SDS-PAGE (NuPAGE™ 4-12% Bis-Tris Protein Gels, Invitrogen™). Antibodies were stored at 4 °C. Trastuzumab (Herceptin®) was purchased from Oxford University Hospital, CD64 human recombinant (His Tag) was purchased from SinoBiological, recombinant human FcRN (His and Avi tagged) was purchased from Stratech Scientific Ltd, ErbB2 (Her2) human recombinant was purchased from Sigma-Aldrich. Deglycosylated trastuzumab was obtained

by treatment with Endo S (New England BioLabs) at 37 °C, overnight. 2G12 antibody was used for contrast vs. molecular weight calibration, with monomer and dimer masses of 148.5 and 296.9 kDa respectively.

Samples and buffers were filtered through 0.1 μm centrifugal filters (Ultrafree –MC- VV, MerckMillipore) prior to use. Initial stock concentrations of all proteins were measured using a DeNovix DS-11+ spectrophotometer. Protein solutions were diluted in PBS (Gibco® DPBS (1X)) to obtain concentrations between 0.2 to 1 absorbance at 280 nm (low μM range). Pipetting precision was checked with a microbalance (Mettler Toledo, AT261).

Relative Abundance Measurements

For the experiments determining the accuracy of determining relative abundances (Figure 3.1), we used the two SEC-fractions of the 2G12 antibody purification (Figure 3.15 and 3.16), containing either the pure monomer or the intermolecular domain exchanged dimer version of the monomer.[213] Charac-

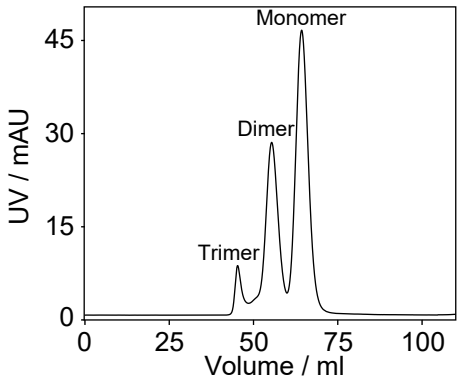


Figure 3.15: Size exclusion chromatography of 2G12. UV profile of the monoclonal antibody 2G12 monomer, dimer and trimer/aggregation complexes.

terization of the monomer fraction with MP confirmed the absence of dimerization and analogously the dimer fraction revealed absence of dissociation into monomer. Different ratios of the two non-interacting species (monomer and dimer) were mixed at μM concentration and diluted in PBS to pM-nM

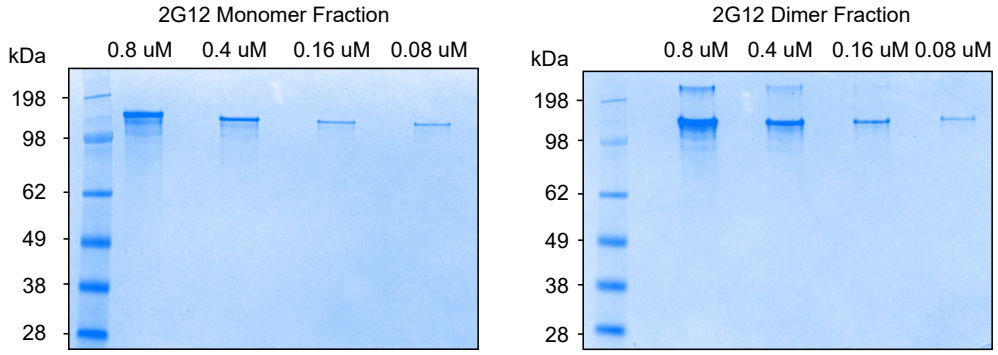


Figure 3.16: SDS-PAGE of SEC purified 2G12. (top) Monomer fractions and (bottom) dimer fractions. Concentrations from 0.8 μM to 0.08 μM were imaged for each monomer/dimer SEC fraction.

concentrations prior to measurement (Table 3.3). For the two lowest M:D ratios (0.15 and 0.22) in Figure 3.1 c and d the pure monomer stock solution had to undergo an additional step from 1 µM to 500 nM. All pipetting steps were checked on a microbalance.

Table 3.3: 2G12 stock solutions and diluted concentrations

Figure	2G12 monomer (stock mixture) μM	2G12 dimer (stock mixture) μM	2G12 mononomer (diluted mixture) nM	2G12 dimer (diluted mixture) nM
1 a	0.59	0.74	2.9	3.6
1 b	0.59	0.74	2.9	3.6
1 c + d	1.4	0.17	5.3	0.63
	1.2	0.35	4.9	1.4
	0.88	0.55	3.9	2.4
	0.59	0.74	2.9	3.6
	0.37	0.88	2.0	4.8
	0.19	0.88	1.2	5.7
	0.14	0.95	0.90	6.1

Screening Experiments

Screening experiments (Figure 3.7, 3.8 and 3.14): Individual FcRs (FcγRIa, FcRn) and IgGs (trastuzumab and deglycosylated trastuzumab) were mixed at μM concentration in a 1:1 (IgG-FcγRIa, deglycosylated IgG-FcγRIa) or

1:2 (IgG-FcRn) ratio and incubated overnight at room temperature (see Table 3.4 for exact concentrations). The μM mixtures were diluted in PBS to pM-nM concentrations and measured at specific incubation times. For FcRn-IgG (Figure 3.14), this procedure was repeated for each pH (5.0, 5.5, 6.0, 7.2). *Kinetic experiments (Figure 3.11 a-d):* Dissociation experiments were prepared as described for those shown in Figure 3.7 and 3.8 and repeated after specific incubation times. For association experiments, individual proteins were diluted in PBS to pM-nM concentrations and then mixed in 1:1 ratios. Measurements were taken after specific incubation times had elapsed. For association experiments of IgG and FcγRIa, the pure compounds were diluted to nM concentrations, mixed, then incubated for the desired incubation time and then measured by MP. The sample tube passivation protocol, based on casein was applied (see section 3.4.5).

Table 3.4: FcR/IgG mixtures and incubation times

Figure	FcR (stock) /μM	IgG (stock) /μM	FcR (diluted mixture) /nM)	IgG (diluted mixture) /nM	incubation time after dilution /min
3.6 a	2.7	2.7	4.4	4.4	10-18
3.6 b	2.9	2.9	4.6	4.6	12-18
3.7 a	2.9	2.9	0.3, 1.3, 4.6	0.3, 1.3, 4.6	
				10-35	
3.7 b	2.9	1.3	1.3	1.3	0.4-30
3.14 a	18.8	7	11.8	9.2	0.4-89
3.14 b	16.9	7.6	0.4-6.0	0.2- 2.7	0.5-78
3.11 b	2.7	2.7	0.21- 0.26	0.21- 0.26	1.8-88
3.11 a	2.6	2.6	4.6- 4.9	4.5- 4.8	0.3-58

ErbB2-trastuzumab Interaction Study

Experiments were performed analogously to IgG-FcγRIA. Briefly, we applied the K_{d} screening procedure to investigate the binding affinity of trastuzumab

to the ErbB2 (HER2) antigen. The two compounds were mixed in a 1:1 molar ratio and incubated at room temperature overnight. The next day, MP data was acquired at different dilutions (0.3, 1.3, 4.6 nM trastuzumab concentration) and time points after dilution (2.5 – 100 min). Gaskets were used for the experiments with the 1.3 and 4.6 nM dilutions and the continuous flow setup for the 0.3 nM dilution (Figure 3.3).

3.4.3 MP Data Acquisition

Microscope coverslip cleaning and assembly was performed as described previously.[4] Borosilicate microscope coverslips (No. 1.5H thickness, 24 x 50 mm, VWR (630-2603) were cleaned by 5 min sequential sonication (PS-40A Ultrasonic Cleaner, Cole Palmer) in Milli-Q water, isopropanol and Milli-Q water, followed by drying under a clean stream of nitrogen. Quality control of new batches of coverslips was based on checking the surface roughness on the mass photometry native images for 6 out of 100 coverslips from a single box. Batches with large particles or irregularities on the glass surface were disposed. Clean coverslips were assembled for sample delivery using silicone gaskets (CultureWell^{TM} reusable gasket, 3mm diameter x 1 mm depth, Grace Bio-Labs) or plastic flow chambers (sticky-Slide VI 0.4, Ibidi). For experiments involving flow chambers, a microfluidic syringe pump-based system was used (World Precision Instruments AL-1000) (Figure 3.3). For data acquisition, gaskets were filled with buffer (40 μl) to enable focusing of the glass surface. Subsequently, 36 μl were removed, while keeping the focus position stable, and replaced by 36 μl sample solution at nM concentration. Measurements were started immediately (delay time $\sim$2 seconds) for 30 - 60 seconds. For samples with sub-nM K_{d} values, we conducted continuous flow experiments at sub-nM concentrations typically over 240 s. Flow chambers were filled with

150 μl buffer and connected to the sample reservoir and syringe pump, while preventing the generation of air bubbles in the flow chamber. The flow chamber was then placed on the instrument in a way that the laser was positioned close to the inlet of the flow chamber. Next, the syringe pump was started in pump mode and run at 90 μl /min. Once the sample reservoir was almost empty, the sample (sub-nM concentration) was injected, focus checked and the measurement started. The acquisition time was chosen depending on concentration, i.e. lowering the concentration by a factor of 10 requires 10 times longer acquisition times to keep the total number of molecular counts constant. Continuous flow experiments at concentrations in the nM range or higher should be avoided because the coverslip glass surface becomes saturated with analyte molecules within 1 min after injection. The experimental mass photometry setup has been described elsewhere.[3,4] Briefly, a 525 nm laser diode was used for illumination with the following instrument parameters: acquisition camera frame rate = 955 Hz, pixel binning = 4x4, 5-fold time-averaging. Data was acquired for 30 or 240 s, depending on the experiment. Particle detection and quantification was processed as described by Young et al. using custom software written in Python.[4] For each particle a time stamp, position and contrast value was obtained.

Quality Control for Quantitative Measurements

During acquisition, each video was examined visually and excluded when one of the criteria listed Table 3.5 was met. During data analysis we applied an xy-distance constraint filter to all confirmed counts, excluding particles which were recorded at the same xy-position in the field-of-view. This helped to exclude "blinkers" (i.e. fast binding and unbinding events at the same position) and significantly lowered the baseline/noise. For gasket experiments, we plotted the counts as a detection rate ($-\delta$counts/δt) of the measured species X vs.

time. The resulting decay curve was expected to follow a single exponential decay, which indicates an error-free experiment. We experienced deviations from a smooth decay when one or several of the criteria in Supplementary Table 3.5 were given.

Table 3.5: Quality Data Criteria and Indicators

Criteria	Indicators	Most common reasons
Out-of-focus measurement	Inversed contrast or anomalous PSF of particles in ratiometric image or no counts	Wrong focus position
Unstable focus	Focus voltage is drifting	Excessive immersion oil between stage and coverslip
Rough/irregular glass surface	Large interfering black dots in native image	Insufficient quality control during glass cleaning procedure
Unbinding events	Particles with negative contrast values	Unsuitable pH, unsuitable glass surface properties (test APTES coating)[214]
Buffer impurities	Large particles floating around and causing interferences in the ratiometric image	Buffer or sample not filtered suitably (i.e. 0.22 μm filter), sample is precipitating under chosen conditions
Too high concentration	Particles are overlapping in time and position	Incorrect dilution

3.4.4 Data Analysis

Quantification of species-specific counts: Contrast values of observed counts were converted into molecular weight via a mass calibration (Figure 3.17), here with the 2G12 WT antibody monomer and dimer peaks. In the resulting molecular weight (MW) vs. counts histogram each species was identified as a resolved peak and counts were obtained from Gaussian fitting to these peaks. Molecular weights near the MP detection limit (ca. 40 kDa) were not quantified

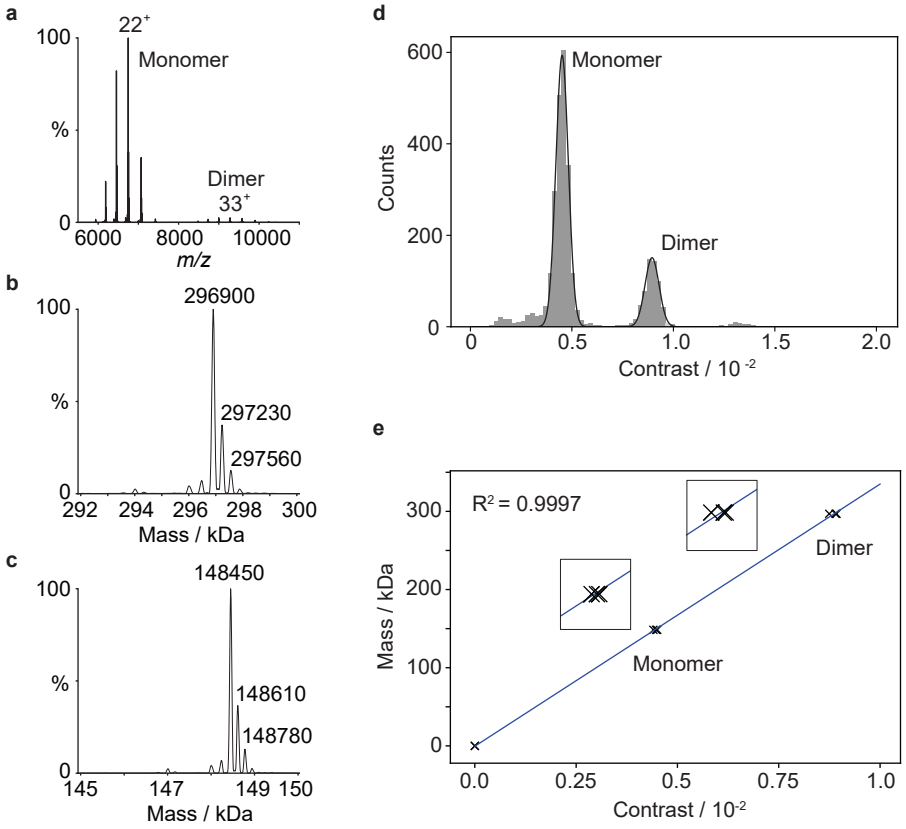


Figure 3.17: Native mass spectrometry of 2G12 and contrast calibration. (a) Native mass spectrometry of 2G12 (top spectrum). (b,c) Zoom of the zero-charge state deconvoluted spectra, showing monomer mass range and dimer mass range. (d) Corresponding mass distribution obtained by MP. (e) MP mass calibration and reproducibility.

to ensure differentiation from background noise and were generally not treated as quantitative with respect to counts for larger species (Figure 3.18).

The measured counts were then converted into molar concentrations following the protocol described in equations 3.1-3.5 (for IgG and FcγRIa) and equations 3.7-3.13 (for IgG and FcRn). For continuous flow experiments, the counts were diffusion-corrected by normalizing to the MW-dependent factor of the diffusion coefficient ($MW^{-1/3}$). For gasket experiments, the contribution from diffusion was negligible, as shown in Figure 3.3 and 3.2.

K_d screening experiments (Figure 3.7,3.8 and 3.14): K_d values are calculated

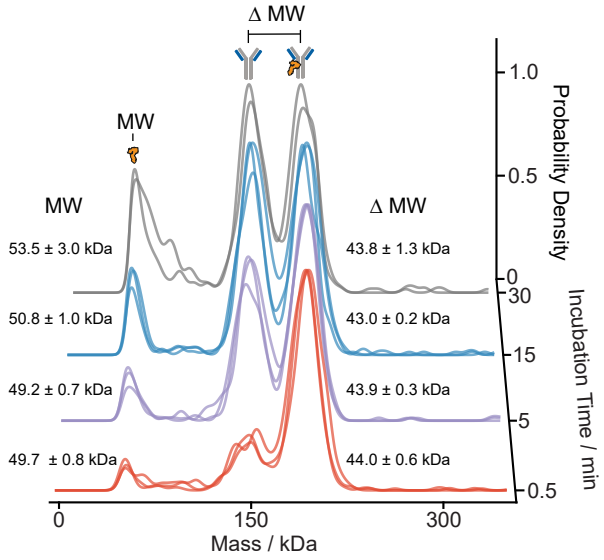


Figure 3.18: Assignment of FcγRIa molecular mass. FcγRIa mass measured from the FcγRIa peak (left, around 50 kDa). FcγRIa mass measured from the mass difference between bound IgG (FcγRIa + IgG) and unbound IgG (right, 150- 200 kDa). We expect the molecular weight of FcγRIa (ca. 43-44 kDa) from the mass difference method to be more accurate than the direct read-out (49-54 kDa) due to its vicinity to the detection limit of our instrument.

by inserting the molar concentrations obtained from the previous section into equation 3.6 for IgG-FcγRIa and equations 3.14-3.18 for IgG-FcRn.

Kinetic experiments (Figure 3.11 a-d): Monitoring association or dissociation of the biomolecular complex allowed us to extract on-and off-rates. Additionally, we could extract K_{d} values after reaching equilibrium (plateau regions in the kinetic plots). Kinetic data sets were always composed of a series of individual MP experiments acquired at different time points after dilution from μM to pM-nM (continuous flow or gasket experiments). In both cases, we can extract the time-dependent ratio of free vs. bound species from each measurement at a given time. *Association experiment:* We begin by defining the differential equation describing the time-dependence for association (equations 3.22-3.28), based on the stoichiometric information from our MP experiments. In the association experiment, the starting concentrations of each species at t = 0 are known (equations 3.19-3.21). We also know that $[\mathrm{IgG}_{bound}]_0$=0 and

[IgG_{bound}]=x_t, i.e. x_t is the amount of generated complex since mixing. The ordinary differential equation (ODE), equation 3.28, is numerically solved in Mathematica (Mathematica, Version 12.0) with the built-in function "Dsolve". With this the numerical solution of x_t was obtained as a function of k_{on} and k_{off}. The result for x_t is fit to the experimentally obtained ratio of the counts of IgG_{bound} and the total counts of IgG as described in equation 3.29. For fitting we used Mathematica's built-in function "NonlinearModelFit" with the method "NMinimize" to optimize k_{on} and k_{off}. From this we obtain K_{d}, k_{on} and k_{off} values and confidence intervals (Figure 3.11 c, d). Specifically, fitting involved two parameters (k_{on} and k_{off}), the NonlinearModelFit function returned 95% confidence intervals for the separate estimates of k_{on} and k_{off}. As these values were not symmetric about the mean, the reported error bars in Figure 3.11 were the greater of the two values. This function also returned a 95% parameter confidence region in the "k_{off}, k_{on}" plane. This was used to calculate the largest and smallest $K_{\mathrm{d}} = k_{\mathrm{off}}/k_{\mathrm{on}}$ that was within the confidence region. Similarly as above, these values were not symmetric about the mean and the greater of the two were reported. Scattering of the data was partly attributed to experimental error arising mostly from UV-VIS spectrophotometer concentration measurements, with an expected relative error of ∼5%. The shot noise contribution to the scattering can be estimated from the mean relative standard deviation for each figure (3.8 ± 0.3%, 3.9 ± 0.4%, 5.1 ± 0.5% and 6.1 ± 0.7%) calculated from the total counts shown in Table 3.6. *Dissociation experiment:* First, we calculate the K_{d} from the plateau region of the plot (equations 3.1-3.6). Knowing the K_{d} and the total concentrations of IgG and FcγIa before dilution (ca. μM), we can calculate the equilibrium concentrations of each species before dilution by solving equation 3.32 and inserting into equations 3.30 and 3.31. At t = 0 after dilution, this distribution is unchanged, and the concentrations

have to be divided by the dilution factor (equations 3.33-3.35). This yields $[IgG_{bound}]_0=[IgG_{bound}]_{(eq,conc)}/f_{dilution}$ and $[IgG_{bound}]=[IgG_{bound}]_0-x_t$, i.e. x_t is the amount of dissociated complex since diluting from the stock concentration to pM/nM concentration. Proceeding as described for the association experiment and using equations 3.36-3.42 we obtain K_d, k_{on} and k_{off} values (Figure 3.11 a-d). In the future, we could combine the information from association and dissociation data and perform the fitting iteratively/simultaneously, from which k_{off}, k_{on} and K_d can be obtained without waiting for equilibration. This approach will extend our applicability to slow reactions by circumventing equilibration times of hours or even days (Figure 3.12) and with this also reduce sample loss due to non-specific adsorption to sample tubes over time (Figure 3.4).

3.4.5 Non-specific Adsorption: Challenges and Solutions

Protein Passivation of Sample Tubes

Bovine serum albumin (BSA, Sigma-Aldrich) was prepared as a 1 μM solution in phosphate buffered saline (PBS) (Gibco® DPBS). 1 ml of this solution was added to each sample vial (1.5 ml Safe-Lock Tubes, Eppendorf) and rotated for ca. 2 hrs at room temperature (VWR rotator, VWR). The solution was completely removed, washed 3 times with PBS (1 ml each), filled with PBS and rotated for 30 min, then washed 3 times with PBS (1 ml each). All liquid was removed and replaced by either PBS buffer or 5 nM trastuzumab (Herceptin®). The trastuzumab solution was directly diluted in the passivated tube by mixing 2 μl of trastuzumab with 398 μl PBS. The control sample was prepared in the same way, but using an untreated sample vial. casein from bovine milk (technical grade, Sigma-Aldrich) was dissolved as 1 mg/ml in phosphate buffered saline (PBS) (Gibco® DPBS) at 42 °C overnight. 1

Table 3.6: : Total Number of Counts for Kinetic Experiments

Figure 3.11a		Figure 3.11b		Figure 3.11c		Figure 3.11d	
Time after dilution / s	Counts	Time after dilution / s	Counts	Time after dilution / s	Counts	Time after dilution / s	Counts
222.5	688	26	927	32	409	28	518
259.8	570	28	611	36	396	53	404
265.3	818	39	820	43	396	70	370
1117.6	657	49	810	51	361	182	268
1180.8	546	69	647	66	264	210	404
1288.4	494	88	770	81	337	227	365
2029.1	849	112	463	116	258	352	403
2110	708	223	480	214	319	367	504
2400	738	253	502	244	261	508	364
2958.8	835	267	868	251	193	535	483
3046.1	573	336	564	322	251	560	464
4352.2	681	406	620	355	400	675	398
4675	715	467	697	368	309	685	464
5332.5	651	555	468	437	242	691	358
5389.9	800	611	894	441	220	720	416
		663	700	467	277	842	246
		884	712	505	275		
		888	786	635	245		
		937	717	659	253		
		990	760	687	200		
		1097	672	701	346		
		1100	673	824	263		
		1149	605	856	168		
		1356	712	903	305		
		1501	548	1042	245		
				1130	227		
				1457	236		

ml of the solution was added to each sample vial (1.5 ml Safe-Lock Tubes, Eppendorf) and rotated for ca. 2 hrs at room temperature. The solution was completely removed, washed 3 times with PBS (1 ml each), filled with PBS and rotated for 30 min, then washed 3 times with PBS (1 ml each). All liquid was removed and replaced by either PBS buffer or 5 nM trastuzumab

(Herceptin®). The trastuzumab solution was directly diluted in the passivated tube by mixing 2 μl of trastuzumab with 398 μl PBS. The control sample was prepared in the same way, but using an untreated sample vial.

Non-specific Protein Adsorption to Sample Tubes

*m*PEG-silane coated glass vials (1.75 ml, Samco Trident Vial Tall with PP Screw Cap) were sonicated (PS-40A Ultrasonic Cleaner, Cole Palmer) for 10 min in 2% aqueous Hellmanex solution (Hellmanex III, HellmaAnalytics), washed with deionized water, then sonicated for 10 min in deionized water. The sonication step was repeated in ethanol. In a next step the glass vials were thoroughly dried under a stream of dry nitrogen and then placed in an O_2 plasma (Zepto System, Diener Plasma Surface Technology) for 8 min. After plasma cleaning the vials were filled with a 5 mg/ml *m*PEG-silane solution in 1% acetic acid in ethanol. *m*PEG-silane was purchased from Laysan Bio as "MPEG-SIL-2000". The vials were then placed in an oven (Vacucenter, SalvisLab) at 70 °C and the reaction solution mixed after 30, 60 and 90 min. After 2 hrs, the vials were emptied, washed with ethanol and deionized water and blow-dried under a stream of dry nitrogen. *Plasma cleaned glass vials:* The protocol for "mPEG-silane coated glass vials" was stopped after the plasma cleaning step. *Tween treated glass vials* (1.75 ml, Samco Trident Vial Tall with PP Screw Cap) were incubated for 4 hours with 2% aqueous Tween solution (Tween20, Sigma-Aldrich), then rinsed with deion. water and blow-dried under a stream of dry nitrogen. For *untreated glass vials* we used 1.75 ml, Samco Trident Vial Tall with PP Screw Cap. For protein LoBind tubes we used Protein LoBind Tubes (1.5 ml, Eppendorf). Safe-Lock Tubes (1.5 ml, Eppendorf) were used as Eppendorf tubes. Tween treated Protein LoBind tubes (Protein LoBind Tubes (1.5 ml, Eppendorf)) were incubated for 4 hours with 2% aqueous Tween solution (Tween20, Sigma-Aldrich), then rinsed with

deionized water and blow-dried under a stream of dry nitrogen. PCR tubes were Fisherbrand 0.2 ml PCR tubes. In the last step, all tubes were washed with phosphate buffered saline (PBS) (Gibco® DPBS), dried and then incubated with 5 nM trastuzumab (Herceptin®) in PBS for 20 hrs at room temperature. A freshly prepared 5 nM IgG solution in LoBind tubes was used as a reference. The acquisition time of MP experiments was 90 s. Absolute count values of the IgG peak were then used to compare the performance of different sample tubes, i.e. counts were used as an indicator for absolute concentration.

3.4.6 Surface Plasmon Resonance

Surface plasmon resonance experiments were carried out using a BIAcore T200 instrument (GE Healthcare). All experiments were performed in 10 mM HEPES, pH 7.4, 150 mM NaCl, 0.005% Tween 20 at 25 °C. Trastuzumab and deglycosylated trastuzumab mAb were immobilized on a CM5 chip (GE Healthcare) by amine coupling. Concentration series of human FcγRIa (A: 0.007-27 nM, B: 0.027-110 nM) were flowed over IgG (trastuzumab) (A) or deglycosylated IgG (trastuzumab) (B) bound surface at 30 µl/min for 120 s followed by buffer for 900 s. After each run, the biosensor chip was regenerated using 10 mM glycine, pH 2.5, which breaks the antibody-FcγR interaction. The specific binding response to antibody was obtained by subtracting the response given by analytes to an uncoupled surface and a blank run of buffer only. The kinetic sensorgrams were fitted to a global 1:1 interaction model to allow calculation of k_{on}, k_{off}, and K_{d} using BIAevaluation software 2.0.3 (GE Healthcare).

3.4.7 Native Mass Spectrometry

Deglycosylated and intact IgG were buffer exchanged into 1 M aqueous ammonium acetate (Sigma-Aldrich) using P6 Biospin columns (Bio-Rad) for the first

two exchanges, followed by two exchanges using Amicon Ultra centrifugal filters (0.5 ml, 30 kDa MWCO) and in a last buffer exchange to 200 mM aqueous ammonium acetate using Amicon Ultra centrifugal filters. All protein solutions were analyzed at concentrations between 5 and 10 μM. Experiments were carried out on a prototype Thermo Scientific Q Exactive Hybrid Quadrupole Orbitrap Mass Spectrometer. Data were acquired using Xcalibur 3.0 software (Thermo Fisher Scientific) and raw spectra were deconvoluted to zero-charge spectra using UniDec.[215] Complete deglycosylation of the IgG could be confirmed (Figure 3.19).

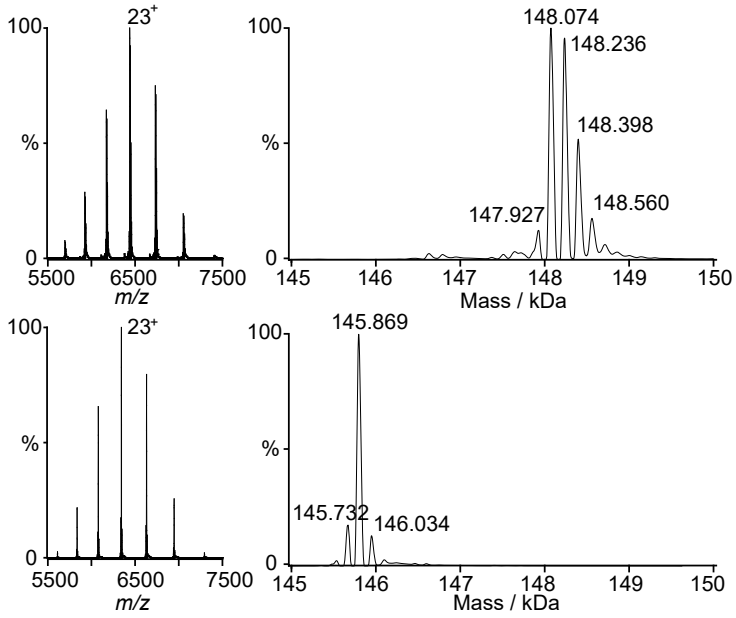


Figure 3.19: Native MS experiments to confirm IgG deglycosylation. Native MS of IgG (top, left) and corresponding zero-charge state deconvoluted spectrum (top, right). Corresponding deglycosylated IgG following treatment with Endoglycosidase S (native spectrum, bottom left and zero-charge state deconvoluted spectrum, bottom, right

3.4.8 Equations

Equilibrium experiments

IgG - FcγIa and deglycosylated IgG - FcγIa:

We started with the calculation of K_{d} values from relative abundances measured

with MP. For the interactions of IgG - FcγIa and deglycosylated IgG - FcγIa we obtain the following equations for the mass balance:

$$[IgG]_{tot} = [IgG]_{unbound} + [IgG]_{b}ound \tag{3.1}$$

, where $[\mathrm{IgG}]_{\mathrm{total}}$, $[\mathrm{IgG}]_{\mathrm{unbound}}$ and $[\mathrm{IgG}]_{\mathrm{bound}}$ are IgG molar concentrations. For the conversion of counts into molar concentrations we used the following conversion factor:

$$f_{conversion} = \frac{[IgG]_{total}}{(\mathrm{counts}(IgG_{unbound}) + \mathrm{counts}(IgG_{bound}))} \tag{3.2}$$

, where $\mathrm{counts}(\mathrm{IgG}_{\mathrm{unbound}})$ and $\mathrm{counts}(\mathrm{IgG}_{\mathrm{bound}})$ are the counts obtained from Gaussian fits to the mass histograms, $\mathrm{f}_{\mathrm{converesion}}$ is the conversion factor which converts counts into molar concentrations. With this we can now convert counts into molar concentrations:

$$[IgG]_{bound} = \mathrm{counts}(IgG_{bound}) * f_{conversion} \tag{3.3}$$

$$[IgG]_{unbound} = \mathrm{counts}(IgG_{unbound}) * f_{conversion} \tag{3.4}$$

$$[Fc\gamma Ia]_{unbound} = [Fc\gamma Ia]_{total} - [IgG]_{bound} \tag{3.5}$$

Due to variable noise contributions in the low molecular weight range (<80 kDa), we have to calculate the molar concentration of FcγIa via equation 3.5. The K_{d} is then obtained from equation 3.6.

$$K_d = \frac{[Fc\gamma Ia]_{unbound} * [IgG]_{unbound}}{/[IgG]_{bound}} \tag{3.6}$$

IgG - FcRn:

For the interactions of IgG-FcRn we have to take the monomer and dimer of FcRn, the IgG, as well as the 1:1 and 1:2 complex of IgG-FcRn into account and obtain the following equation for the mass balance:

$$[IgG]_{total} = [IgG]_{unbound} + [IgG]_{singlebound} + [IgG]_{doublebound} \tag{3.7}$$

Analogous to above we can calculate a conversion factor to convert counts into molar concentration:

$$f_{converesion} = \frac{[IgG]_{total}}{\begin{array}{c}\text{counts}(IgG_{unbound})+ \\ \text{counts}(IgG_{singlebound}) + \text{counts}(IgG_{doublebound})\end{array}} \tag{3.8}$$

Conversion of counts to molar concentrations:

$$[IgG]_{bound} = \text{counts}(IgG_{bound}) * f_{conversion} \tag{3.9}$$

$$[IgG]_{singlebound} = \text{counts}(IgG_{singlebound}) * f_{conversion} \tag{3.10}$$

$$[IgG]_{doublebound} = \text{counts}(IgG_{doublebound}) * f_{conversion} \tag{3.11}$$

$$[FcRn_{dimer}] = \text{counts}(FcRn_{dimer}) * f_{conversion} \tag{3.12}$$

$$\begin{aligned}[FcRn_{monomer}] =&[FcRn]_{total} - 2 * [FcRn_{dimer}]- \\ &[IgG]_{singlebound} - 2 * [IgG]_{doublebound}\end{aligned} \tag{3.13}$$

Calculation of K_{d} values for IgG-FcRn interactions:

$$K_1 = \frac{[FcRN_{monomer}]^2}{[FcRN_{dimer}]} \tag{3.14}$$

$$K_2 = \frac{[FcRN_{monomer}] * [IgG]_{unbound}}{[IgG]_{singlebound}} \tag{3.15}$$

$$K_{3a} = \frac{[FcRN_{monomer}] * [IgG]_{singlebound}}{[IgG]_{doublebound}} \tag{3.16}$$

$$K_{3b} = \frac{[FcRN_{dimer}] * [IgG]_{unbound}}{[IgG]_{doublebound}} \tag{3.17}$$

$$K_{3,app} = K_{3a} * K_{3b} \tag{3.18}$$

Kinetic experiments

Kinetic experiments of IgG - FcγIa and deglycosylated IgG- FcγIa: For association: At t=0:

$$[Fc\gamma Ia] = [Fc\gamma Ia]_0 = [Fc\gamma Ia]_{tot} \tag{3.19}$$

$$[IgG_{unbound}] = [IgG_{unbound}]_0 = [IgG]_{tot} \tag{3.20}$$

$$[IgG_{bound}] = [IgG_{bound}]_0 = 0 \tag{3.21}$$

At t>0:

$$[IgG_{unbound}] = [IgG_{unbound}]_0 - x_t \tag{3.22}$$

$$[Fc\gamma Ia] = [Fc\gamma Ia]_0 - x_t \tag{3.23}$$

$$[IgG_{bound}] = [IgG_{bound}]_0 + x_t \tag{3.24}$$

$$K_d = k_{off}/k_{on} \tag{3.25}$$

$$\frac{\mathrm{d}[IgG_{bound}]}{\mathrm{d}t} = k_{on} * [Fc\gamma Ia] * [IgG_{unbound}] - k_{off} * [IgG_{bound}] \tag{3.26}$$

$$\frac{\mathrm{d}[IgG_{unbound}]}{\mathrm{d}t} = \frac{\mathrm{d}[Fc\gamma Ia]}{\mathrm{d}t} = \frac{-\mathrm{d}[IgG_{bound}]}{\mathrm{d}t} \tag{3.27}$$

$$\frac{\mathrm{d}x}{\mathrm{d}t} = k_{on}*([Fc\gamma Ia]_0 - x_t)*([IgG_{unbound}]_0 - x_t) - k_{off}*([IgG_{bound}]_0 + x_t) \tag{3.28}$$

$$\frac{\mathrm{counts}(IgG_{bound})}{\mathrm{counts}(IgG_{tot})} = \frac{x_t}{[IgG]_{tot}} \tag{3.29}$$

For dissociation: Calculation of the concentrations after equilibration of stock mixtures (ca. μM concentrations):

$$[IgG_{unbound}]_{eq,conc} = [Fc\gamma Ia]_{eq,conc} \tag{3.30}$$

$$[IgG_{unbound}]_{eq,conc} = [IgG]_{tot,conc} - [IgG_{bound}]_{eq,conc} \tag{3.31}$$

$$K_d = \frac{[IgG]_{tot,conc} - [IgG_{bound}]^2_{eq,conc}}{[IgG_{bound}]_{eq,conc}} \tag{3.32}$$

Using the known dilution factor (from diluting the stock mixtures (ca. µM) to nM/pM concentrations): At t=0:

$$[Fc\gamma Ia] = [Fc\gamma Ia]_0 = \frac{[Fc\gamma Ia]_{eq,conc}}{f_{dilution}} \tag{3.33}$$

$$[IgG_{unbound}] = [IgG_{unbound}]_0 = \frac{[IgG_{unbound}]_{eq,conc}}{f_{dilution}} \tag{3.34}$$

$$[IgG_{bound}] = [IgG_{bound}]_0 = \frac{[IgG_{bound}]_{eq,conc}}{f_{dilution}} \tag{3.35}$$

At t>0:

$$[IgG_{unbound}] = [IgG_{unbound}]_0 + x_t \tag{3.36}$$

$$[Fc\gamma Ia] = [Fc\gamma Ia]_0 + x_t \tag{3.37}$$

$$[IgG_{bound}] = [IgG_{bound}]_0 - x_t \tag{3.38}$$

$$K_d = \frac{k_{off}}{k_o n} \tag{3.39}$$

Differential equation describing the dissociation:

$$\frac{\mathrm{d}[IgG_{bound}]}{\mathrm{d}t} = -k_{on} * [Fc\gamma Ia] * [IgG_{unbound}] + k_{off} * [IgG_{bound}] \tag{3.40}$$

$$\frac{\mathrm{d}[IgG_{unbound}]}{\mathrm{d}t} = \frac{\mathrm{d}[Fc\gamma Ia]}{\mathrm{d}t} = \frac{-\mathrm{d}[IgG_{bound}]}{\mathrm{d}t} \tag{3.41}$$

$$\frac{\mathrm{d}x}{\mathrm{d}t} = k_{on} * ([Fc\gamma Ia]_0 + x_t) * ([IgG_{unbound}]_0 + x_t) - k_{off} * ([IgG_{bound}]_0 - x_t) \tag{3.42}$$

$$\frac{\mathrm{counts}(IgG_{bound})}{\mathrm{counts}(IgG_{tot})} = \frac{[IgG_{bound}]_0 - x_t}{[IgG]_{tot}} \tag{3.43}$$

Chapter 4

Investigating protein-protein interactions in HIV with MP

The SOSIP, bsAb and background information about the bsAb was kindly provided by Snezena Vasiljevic, Oxford Glycobiology Institute, Oxford. We are also grateful for the support from the NIH AIDS Reagent Program and Katie Doores, King's College London, who provided us with the samples for the antibody library. gp120, 2G12 and BG505 SOSIP.664 were expressed by Weston B. Struwe and purified in collaboration with Fabian Soltermann.

4.1 Introduction

Over the last 40 years, since the discovery of the human immunodeficiency virus (HIV), HIV has led to more than 32 million deaths and estimates suggest that more than 38 million people are currently infected with HIV worldwide.[216] In 2019, the United States spent more than $ 28 billion on their domestic response and to help countries around the world who are living with HIV and AIDS.[217] The scale of this pandemic highlights the importance of better AIDS therapies to improve patients' lives. Moreover, it is evident that an universal preventative treatment, such as a vaccine, is urgently needed. Despite 4 decades of research efforts no viable vaccine is available yet.

A major challenge is the high mutation rate of the viral genome, which leads to highly diverse structures and changing cellular processes. Eventually this allows HIV to escape from the immune system and newly developed drugs. The viral fusion protein HIV-1 envelope glycoprotein (Env) plays an important role in this evasion process. Env covers the surface of the HIV virion and provides it with extensive and heterogeneous surface glycosylation. This glycosylation, referred to as the glycan shield, is believed to be a primary hurdle in the development of an immune response. First, the host immune system regards the glycan shield as immunologically "self", because glycans are derived form the host cell glycosylation mechanism. Additionally, the high mutation rate of HIV leads to constant changes in the glycan shield and keeps HIV always one step ahead of the immune system and drug development.

Interestingly, some regions in this shield are more constant and led in small sets of infected individuals to the development of broadly neutralizing antibodies (bnAbs). These bnAbs showed neutralization efficacy over various HIV strains. Although, bnAbs cannot completely eliminate the virus, they serve as a starting point for vaccine development by priming the immune system.[218]

A potential avenue towards a vaccine constitute Env-derived immunogens, which could trigger an immune response and induce bnAbs expression.[219] So far, no native-like Env has been successful in promoting bnAb expression in humans.[220]

Briefly, it is assumed that Env exists in several different conformational states, but that only certain states can trigger a beneficial immune response (Figure 4.1a). Knowing the structures of these states could be used to engineer suitable mutants. Such an Env mutant would be an artificially stabilized version of an immunogen-relevant state and would trigger an immune response.

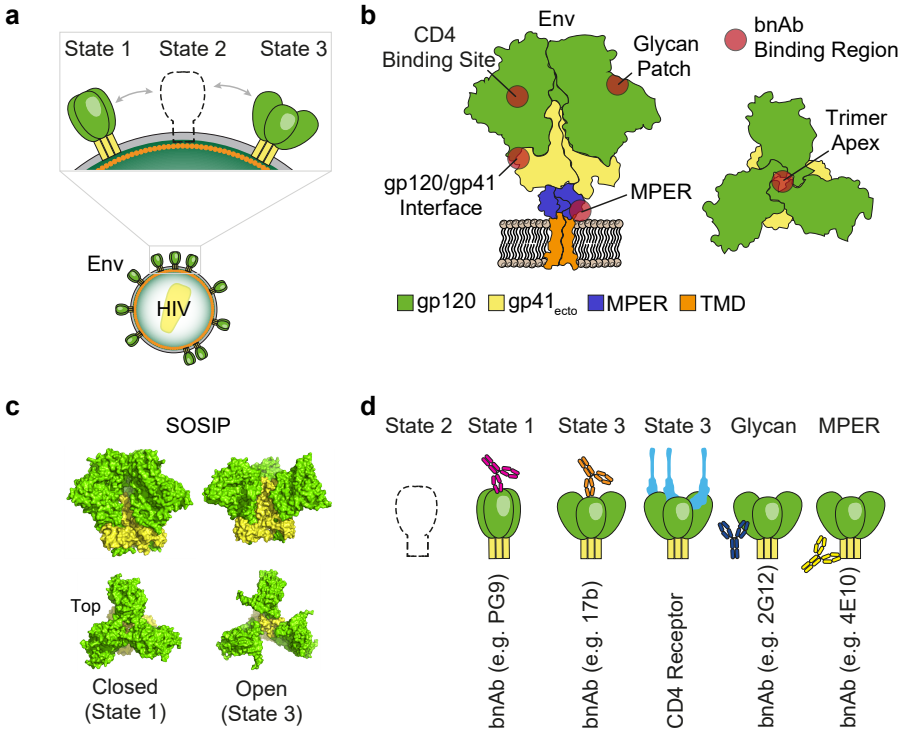


Figure 4.1: Structure, conformational dynamics and epitope targeting on HIV Env trimers. (a) Structural dynamics of viral spike envelope glycoprotein in pre-fusion (1 and 2) and fused state (3). (b) Schematic structure of Env with membrane-proximal external region, trans-membrane domain and epitope map for bnAbs and CD4 receptor. (c) High resolution structures of engineered Env (SOSIP) in open and close state. (d) Principle of probing different Env structures with bnAbs and receptors.

In more detail, Env is a non-covalent trimer, with each sub-unit consisting of a gp120 and gp41 heterodimer (Figure 4.1a, b). The wild-type, unbound Env, present on virus particles, is expected to exist in a pre-triggered conformation, in literature referred to as state 1.[221] Upon binding to its target receptor (CD4 receptor) on the host cell it transitions via an intermediate state 2 to an open conformation, known as state 3.[222] Pre-fusion states related to state 1 are expected to be relevant for immunization.

In 2013, a major progress was achieved with the development of engineered stabilized Env trimers (clade A, BG505 strain), which resemble a state 1 conformation (Figure 4.1c).[223] This BG505 SOSIP.664 gp140 showed high

binding affinity to all bnAbs against multiple neutralizing epitopes on HIV-1 Env. This indicates its potential as a vaccine and provides a biologically relevant model for further biophysical characterization of structure and interactions with binding partners (Figure 4.1d).

Until a universal HIV vaccine is available, treatment is as important as vaccination. In this regard, direct infusion of bispecific antibodies (bsAbs) into the bloodstream to confer immunity has been a promising approach and proven to be effective in non-human primate models.[224] With this the long standing problem of poor control of virus replication and the rapid emergence of resistant variants can be addressed. Bispecific antibodies possess two modalities targeting different epitopes on the same Env protein, making them more potent and less prone to loss of efficacy when mutations occur. Although, bsAbs promise to be superior in these aspects, the lack of existing bsAbs based immunotherapies exemplify the challenging manufacturing process of these therapeutics. Improvement of expression and purification processes are hampered by the limited capability of established biophysical characterization techniques to provide sufficiently detailed insight into these processes. One such limitation is the differentiation of co-existing species, such as intact and half-molecules as well as mismatched half-molecules. Despite the challenges of bsAbs manufacturing they are becoming increasingly important as biotherapeutics, especially for cancer treatment, as demonstrated by FDA approvals and clinical studies in 2019.[225]

In this chapter we use the unique ability of mass photometry to characterize assembly and functionality of biomolecules, as shown in chapter 3 to characterize bnAbs and bsAbs as well as their interaction with engineered Env trimers. We quantify binding affinities and stoichiometries of these interactions. This allows us to probe and identify different structural states of the Env trimer. The

herein presented approach offers a direct avenue to investigate conformational dynamics which are essential in further developing engineered Env proteins towards a universal vaccine. Finally, we introduce a MP method for biophysical characterization of bsAbs and demonstrate its applicability in bsAb drug development.

4.2 Results and Discussion

As our HIV study is centered around the soluble HIV-1 Env Trimer, BG505 SOSIP.664 (herein referred to as SOSIP) it was paramount to first establish a protocol to reproducibly obtain stable and pure SOSIP. Our work in Chapter 3 highlighted that having a good understanding of analyte purity is critical during the interpretation of MP data from protein-protein interaction studies.

For our MP project, the unambiguous assignment of peaks in a protein-protein interaction experiment is much easier if the number of peaks is low and not interfering in terms of molecular weight. Arguably, for qualitative conclusions, e.g. A binds/binds not to B, samples do not have to fulfil this criterion strictly, for quantitative conclusions it is however strongly recommended to work with highly pure samples.

Applying this principle to our SOSIP sample included a MP based sample purity assessment. In this process the affinity purified SOSIP (against Ni-NTA and PGT151 antibody) was further purified with SEC. The SEC chromatogram (Figure 4.2a) showed several unresolved peaks, indicating different oligomeric states. MP analysis of SEC fractions (Figure 4.2b) revealed high abundance of different oligomeric species (mostly sub-units, SOSIP and SOSIP dimer), ranging from below 100 kDa to above 1000 kDa. Based on these results the fractions with highest relative abundance of SOSIP monomer, our target protein, were selected.

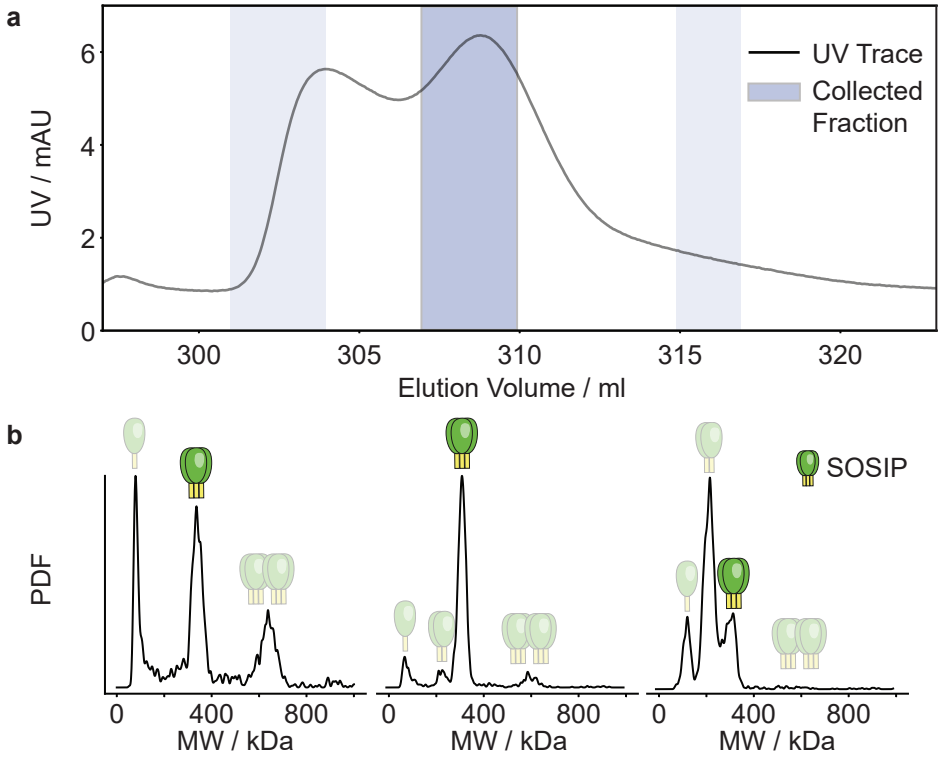


Figure 4.2: Fraction selection of SOSIP SEC-purification. (a) SEC-purification of affinity purified SOSIP (against Ni-NTA and PGT151 mAb) revealed several unresolved peaks, indicating different oligomeric states. (b) MP analysis of different fractions (from left to right) showed SOSIP (green) being present as different oligomeric species (fragments, sub-units, monomer and dimer) with varying abundances. The most homogeneous SOSIP monomer fractions (307 to 310 ml elution volume) were selected for further experiments. MP data (from left to right): 1680, 1549, 2924 counts.

Before starting with the SOSIP interaction study, we wanted to bench-mark the specificity of the bnAbs obtained from collaborators and the NIH AIDS Reagent Program. For this purpose, we simplified our system and first focused on an Env sub-unit, gp120. This is a heavily glycosylated protein, which is usually linked to gp41, the MPER and TMD to build one larger subunit (Figure 4.1). Three of these large subunits constitute then the Env protein.

In Figure 4.3 we show MP data, which suggests that glycan targeting bnAbs (PG9, b12, PGV04, PGT128, 2G12-M and 2G12-D) bind with high specificity to their epitope on gp120, with estimated binding affinities in the nM range.

In more detail, we first performed a MP based purity assessment for all compounds. All bnAbs (except PGT128) and gp120 showed mono-disperse molecular weight distributions at the expected molecular weight (Figure 4.3, dotted and dashed lines). The lower molecular weight shoulder of the PGT128 peak indicated heterogeneity of the sample, potentially due to incomplete assembly of IgG.

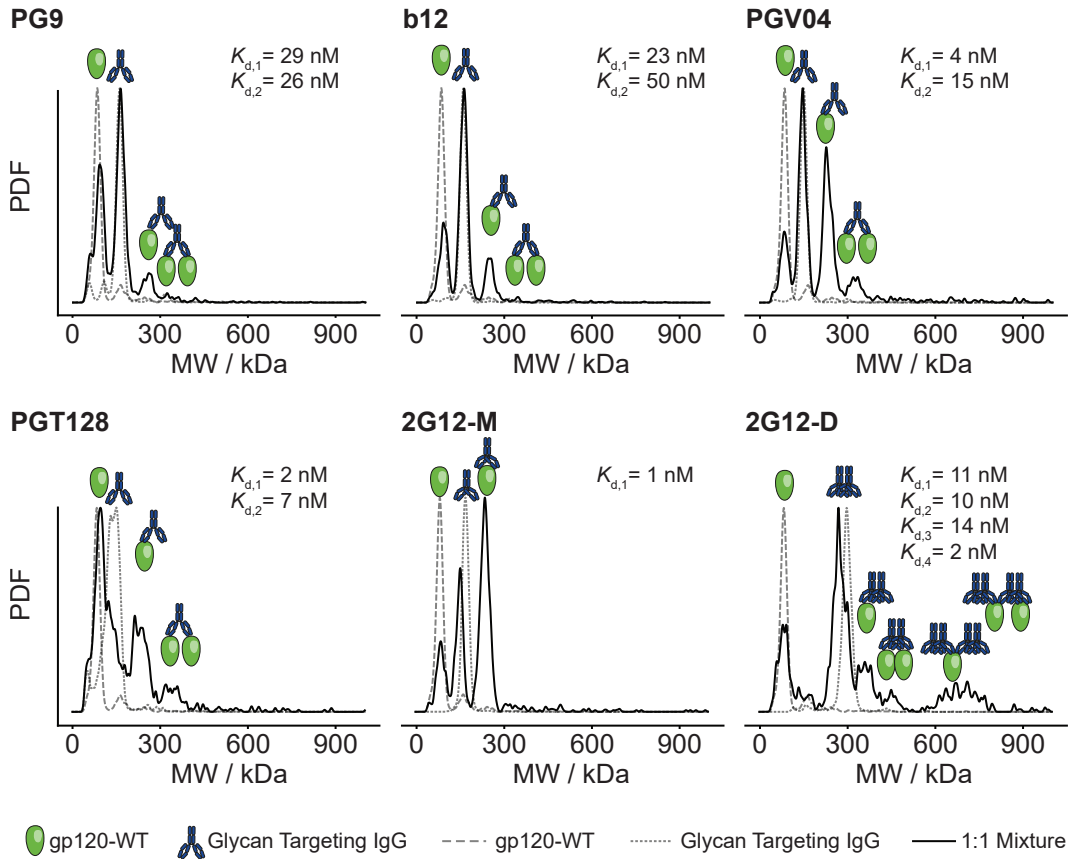


Figure 4.3: Screening of gp120 interaction with glycan targeting bnAbs. Each experiment included MP data of pure gp120 (dashed), pure IgG (dotted) and 1:1 mixture of gp120 and IgG (solid). Glycan targeting bnAbs (blue) formed 1:1 and 1:2 complexes with gp120 (green) and have estimated binding affinities in the nM and pM range. 2G12-D formed various complexes with nM affinity. Experiments were performed by mixing gp120 and IgG in a 1:1 molar ratio at 2 μM each, 2 hrs incubation at RT and dilution to 8 nM each, followed by 60 s MP data acquisition. Observed counts for pure gp120 were 1830, for the pure IgGs and 1:1 mixtures (x counts, y counts) as follows: PG9 (3116, 1842), b12 (3268, 1704), PGV04 (3366, 1292), PGT128 (2229, 1101), 2G12-M (3396, 1008) and 2G12-D (2378, 1071).

In a next step, we measured 1:1 mixtures of gp120 with bnAbs. These experiments revealed 1:1 and 1:2 complex formation with estimated nM binding affinities for most interactions (Figure 4.3 solid lines). As expected, 2G12 only formed a 1:1 complex due to its domain-exchanged architecture, which leaves the 2G12 monomer (2G12-M) with only 1 binding site for gp120. Interestingly, 2G12 dimer (2G12-D), which we isolated during SEC-purification of 2G12-M, revealed formation of various complexes. Beside the expected 1:1 and 1:2 complexes, we also observed a species around 700 kDa (Figure 4.3, 2G12-D). Summing up different molecular weight combinations suggested that 2G12-D can access two binding sites on gp120 to form a complex consisting of 2 2G12-D molecules and one gp120. Although a SPR study[226] reported a 1:1 complex of 2G12-D and gp120 with a binding affinity of 1 nM we report here a previously unknown complexity of this interaction and are able to estimate individual binding affinities for each complex.

A comparison of our gp120-IgG interaction study with literature is shown in Table 4.1. All binding affinities and epitope specificity were in good agreement with reported literature values. Compared to literature, MP data offered additional insights by allowing the quantification of previously unknown stoichiometries and individual binding affinities of co-existing complexes.

Table 4.1: Comparison of literature with MP data (K_d estimates) for the bnAbs-gp120 binding studies. Stoichiometry of IgG (A) to gp120 (B) is shown as A:B, NB indicates "no binding" and "intact?" refers to the structure of the IgG used in the study.

	Literature				Mass Photometry		
	K_d /nM	A:B	Meth.	intact?	K_d /nM	A:B	intact?
PG9	30	2:1	ITC[227]	Fab	29, 26	1:1, 1:2	Yes
b12	20	1:1	SPR[98]	Fab	23, 50	1:1, 1:2	Yes
	50	1:1	SPR[228]	Yes			
	3	1:1	SPR[229]	Yes			
PGV04	10	1:1	SPR[230]	Fab	4, 15	1:1, 1:2	Yes
PGT128	22	1:1	SPR[230]	Fab	2, 7	1:1, 1:2	Yes
2G12-M	6	1:1	SPR[229]	Yes	1	1:1	Yes
2G12-D	1	-	SPR[226]	Yes	various	various	Yes
PGT145	NB	-	FC[223,231]	Yes	NB	-	Yes
PGT151	NB	-	ELISA[232]	Yes	NB	-	Yes
17b	1	1:1	SPR[233]	Yes	11, 19	1:1, 1:2	Yes
4E10	NB	-	ELISA[234,235]	Yes	NB	-	Yes

In control experiments we confirmed that antibodies which are specific to epitopes on fully-assembled SOSIP (PG145 and PGT151) or the membrane proximal external region of Env (MPER) did not show any binding to gp120 (Figure 4.4).

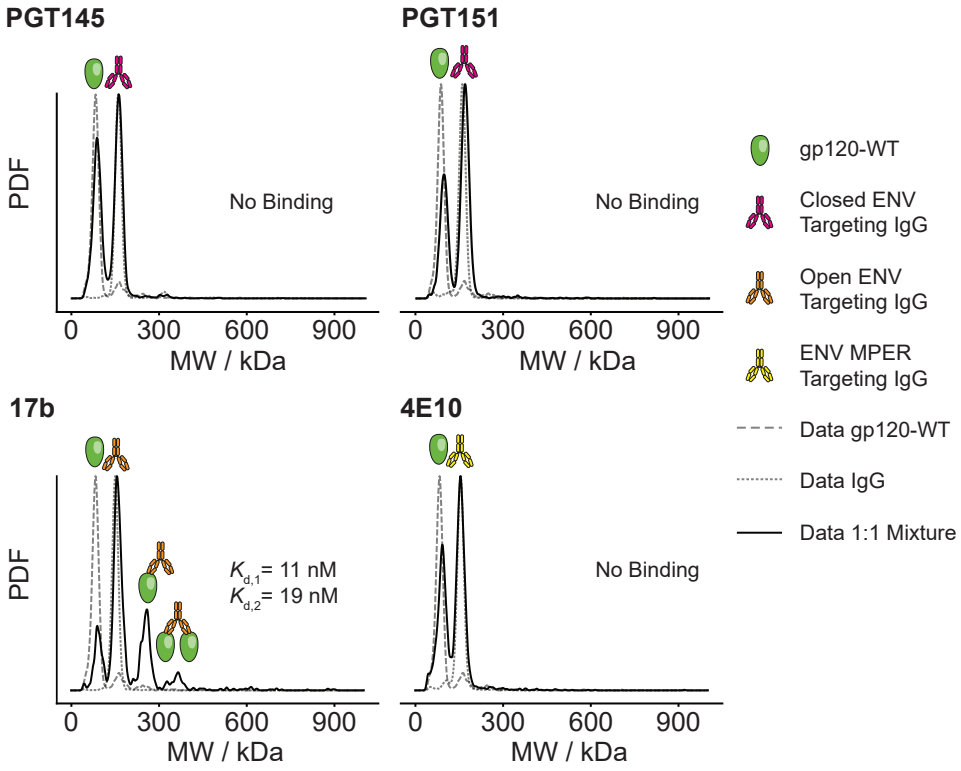


Figure 4.4: Control experiments of gp120 interaction with Env targeting bnAbs. Each experiment included MP data on pure gp120 (dashed), pure IgG (dotted) and the 1:1 mixture (solid). Closed Env conformation targeting bnAbs (pink) showed no interaction with gp120, open Env conformation targeting mAb (orange) formed 1:1 and 1:2 complexes with gp120 and have estimated binding affinities in the low nM range. Env membrane-proximal external region targeting bnAb (yellow) did not show any binding to gp120. Experiments were performed by mixing gp120 and IgG in a 1:1 molar ratio at 2 μM each, 2 hrs incubation at RT and dilution to 8 nM each, followed by 60 s MP data acquisition. Observed counts for pure gp120 were 1830, for pure IgGs and 1:1 mixtures (x counts, y counts) as follows: PGT145 (2883, 3739), PGT151 (3650, 2282), 4E10 (4278, 2142) and 17b (3514, 1316.

Moreover, we confirmed binding of 17b to gp120, which revealed 1:1 and 1:2 complex formation wit nM binding affinities. 17b is known to only bind the open-state Env and should therefore bind gp120 but not to SOSIP in experiments shown later on.

Overall, the gp120-IgG interaction study with MP was a successful proof-of-principle, which showed that we should be able to use bnAbs to probe different structural states of Env with high specificity. In more detail, the

MP data presented in Figure 4.3 and showed that bnABs bound with high affinity (nM to pM) to their specific epitopes on g120 or did not show binding, when the epitope was not present. From the summary shown in Table 4.1 we can conclude that literature and MP agree in all experiments in terms of specificity and affinity and that MP has the advantage of explicitly revealing the stoichiometry of the interaction.

After having shown in the proof-of-principle experiment, that our method is suitable to probe different epitopes on gp120 with high specificity, we then went on to probe SOSIP (closed Env, state 1) with the bnAb library. Given the homo-trimeric architecture of SOSIP and the estimated nM binding affinities from the gp120 experiments, we expected to observe SOSIP-IgG interactions with up to 1:3 stoichiometry, depending on epitope specificity of the IgG. To allow for formation of the expected stoichiometries we added the IgG in 5-fold excess.

Equivalent to the previous experiments, we first investigated the interaction of glycan-specific bnAbs. From literature and gp120 results we expected to see binding to SOSIP for all of these antibodies, except b12 (Table 4.2. In Figure 4.5 we confirm that b12 is not binding to SOSIP. Furthermore, MP data yields estimates of binding affinities in the nM range for PG9 ($K_{\mathrm{d}} = 1$ nM) and a sub-nM K_{d} for PGT128 and 2G12-M, which is in agreement with literature values, compared in Table 4.2.

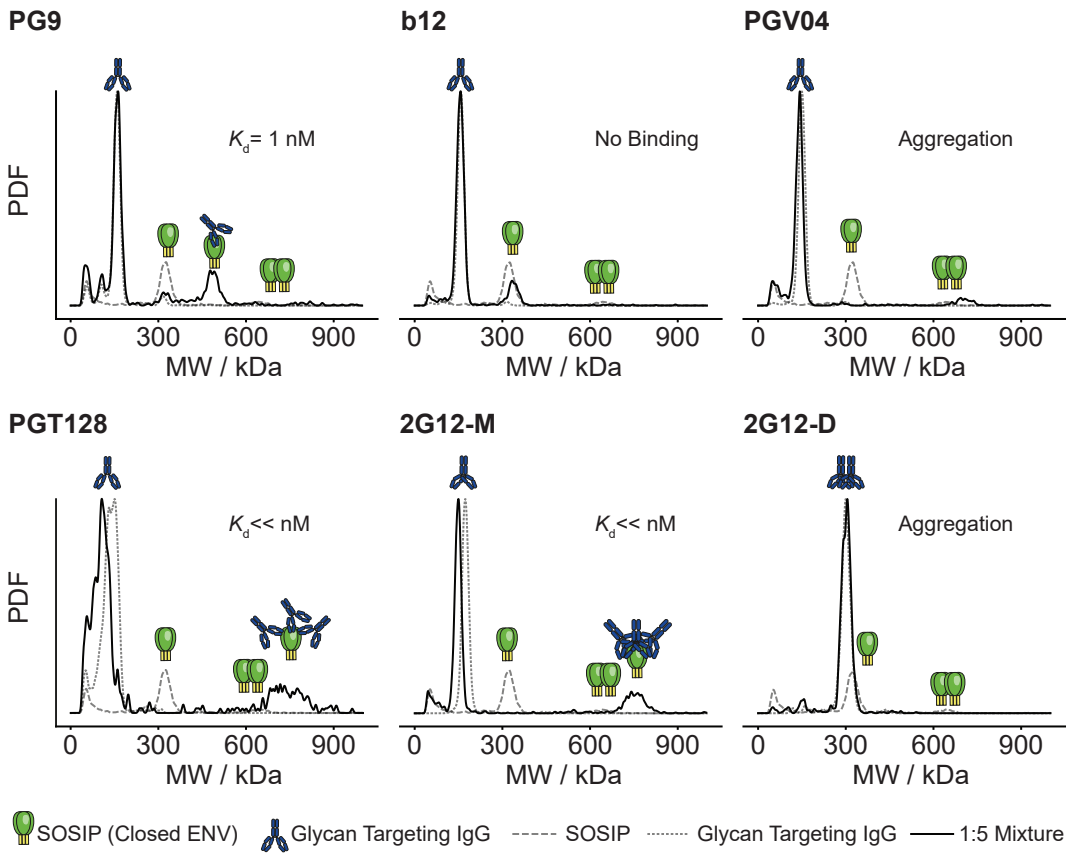


Figure 4.5: Screening of SOSIP interaction with glycan targeting bnAbs. Each experiment included MP data of pure SOSIP (dashed), pure IgG (dotted) and 1:5 mixture of SOSIP and IgG (solid). Glycan targeting bnAbs (blue) showed either no binding, aggregation, 1:1 or 1:3 interactions with SOSIP. Experiments were performed by mixing SOSIP and antibody in a 1:5 molar ratio at low μM concentration, 2 hrs incubation at RT and dilution to 3 nM SOSIP and 12 nM antibody, followed by 60 s MP data acquisition. Observed counts for pure SOSIP were 1241, for the pure antibodies and 1:5 mixtures (x counts, y counts) as following: PG9 (3116, 1191), b12 (3268, 1634), PGV04 (3366, 941), PGT128 (2229, 505), 2G12-M (3396, 1255) and 2G12-D (2378, 853).

Excitingly, the molecular weight resolution of MP provided us with further details of the interactions. MP data for PG9 revealed that PG9 only forms a 1:1 complex. This bnAb is known to bind an epitope on gp120 which is located at the apex of SOSIP (closed-state Env trimer). In other words, the spatial proximity of the individual binding sites on g120 in the closed-state Env trimer allow only for one IgG to bind. Although this is well-known, it highlights the

ability of this MP-bnAb assay to probe structural elements of Env.

In contrast, PGT128 and 2G12-M have an epitope on gp120, which is still accessible in the closed-state of Env trimer (SOSIP). This is confirmed by MP data, which showed formation of SOSIP-IgG complexes with 1:3 stoichiometry.

Surprisingly, we made then the observation that SOSIP related peaks vanished in binding experiments of PGV04 and 2G12-D. From literature we concluded that these IgGs have particularly high affinity (pM) to SOSIP and show up to 2:1 IgG:SOSIP stoichiometry (Table 4.2). In theory, these stoichiometries and binding affinities could allow for infinite cross-linking between species.

In other words, we expect a bidentate IgG with sub-nM affinity for its epitope on SOSIP to be able to cross-link SOSIP molecules, if SOSIP has more than one of these epitopes per molecule and if the structural restraints allow for cross-linking. Considering that mixing was performed at μM, which is up to 10^6 times above the K_d concentration, we suggest that cross-linking followed by precipitation could explain the disappearance of SOSIP and its complexes in MP data.

This hypothesis is further supported by data from the PG9 bnAb (presented above). Although PG9 bound SOSIP with pM affinity we think we did not make the same observation here because PG9 has only one binding site on SOSIP, and literature suggests that the binding is highly dependent on quaternary structure.[227]

Interestingly, we found that binding affinity experiments (Table 4.2) and structure determination of SOSIP-IgG complexes (cryo-EM and X-ray crystallography) in literature are almost exclusively performed with Fabs. We suspect that structural flexibility and difficult to interpret binding data are the main reasons for avoiding intact antibodies in these studies, but that antibody

induced cross-linking could be a factor contributing to complexity of data, when using intact IgGs.

This example also shows that carefully designed experiments with immobilized analytes, e.g. in SPR, can have advantages, despite being often considered as inferior. Immobilizing SOSIP with sparse density on an SPR-chip could still reveal affinities and with additional efforts also stoichiometry, while preventing cross-linking and precipitation of the formed complexes.

Table 4.2: Comparison of literature with MP data (K_d estimates) for the bnAbs-SOSIP binding studies. Stoichiometry of IgG (A) to SOSIP (B) is shown as A:B, NB indicates "no binding", "XL" indicates cross-linking and "intact?" refers to the structure of the IgG used in the study.

	Literature				Mass Photometry		
	K_d /nM	A:B	Meth.	intact?	K_d /nM	A:B	intact?
PG9	5	1:1	SPR[236]	Yes	1	1:1	Yes
b12	NB	-	[237]	-	NB	-	Yes
PGV04	0.008	2:1	SPR[236–238]	Yes	XL	-	Yes
PGT128	3	1:1	BLI[232]	Fab	<nM	3:1	Yes
	6	2.5:1	ITC[223]	Fab			
2G12-M	1	2.5:1	SPR[236]	Yes	<nM		Yes
	16	3:1	SPR[223]	Yes			
2G12-D	-	-	-	-	XL	-	Yes
PGT145	0.2	1:1	SPR[236]	Yes	3	1:1	Yes
	1	1:1	SPR[239]	Fab			
	63	2:1	ITC[237]	Fab			
PGT151	0.3	2:1	SPR[232,236]	Yes	XL	-	Yes
	2	1:1	BLI[232]	Fab			
	130	1:1	ITC[237]	Fab			
17b	NB	-	[223]	-	NB	-	Yes
4E10	NB	-	[235]	-	NB	-	Yes

Finally, we repeated the previous control experiments from the gp120-IgG (PGT145, PGT151, 17b and 4E10) experiments with SOSIP. Firstly, both experiments confirmed that 4E10 does not bind to gp120 nor SOSIP, because 4E10's epitope on MPER is not present on these constructs (Figure 4.6.

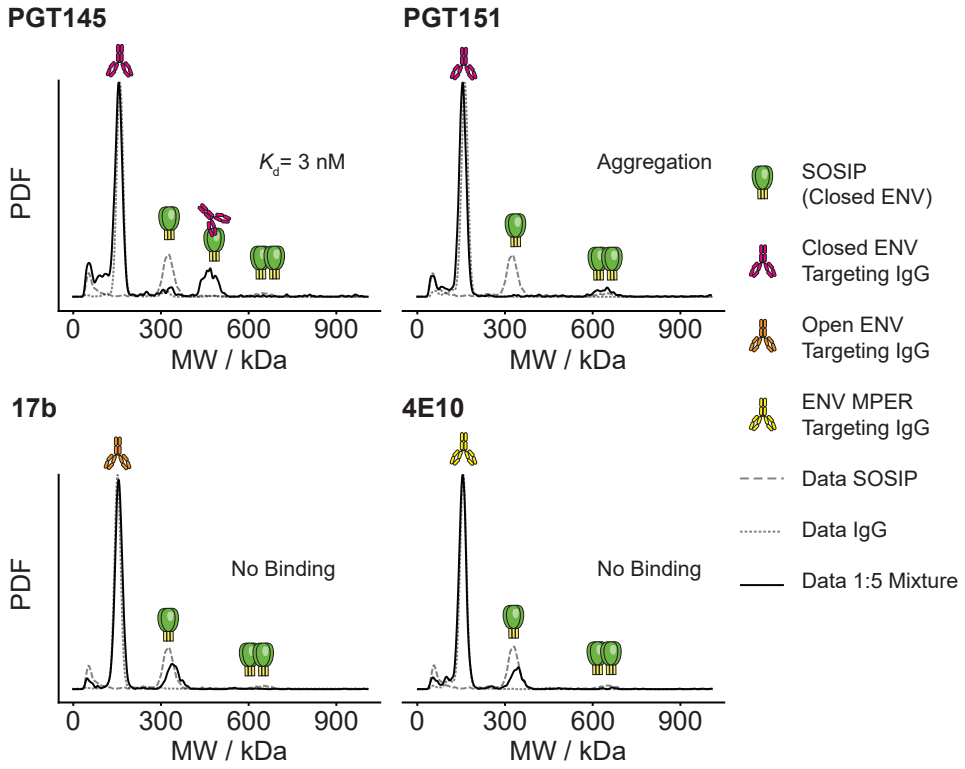


Figure 4.6: Screening of SOSIP interaction with Env targeting bnAbs. Each experiment included MP data on pure SOSIP (dashed), pure IgG (dotted) and the 1:5 mixture (solid). Closed Env conformation targeting bnAbs (pink) showed 1:1 interaction (PGT145) or aggregation (PGT151) with SOSIP. For open Env conformation targeting mAb (orange) no binding was observed (17b). Env membrane-proximal external region targeting bnAb (yellow) did not show binding to SOSIP (4E10). Experiments were performed by mixing SOSIP and IgG in a 1:5 molar ratio at low μM concentration, 2 hrs incubation at RT and dilution to 3 nM SOSIP and 12 nM IgG, followed by 60 s MP data acquisition. Observed counts for pure SOSIP were 1241, for the pure antibodies and 1:5 mixtures (x counts, y counts) as follows: PGT145 (2883, 1382), PGT151 (3650, 1529), 17b (3514, 2013), 4E10 (4278, 1750)

Secondly, we confirmed that the open-state ENV epitope targeted by 17b is accessible on gp120, but is buried in closed-state Env (SOSIP).[223] Thirdly, our MP data showed that PGT145 has a high specificity for its quaternary epitope at the apical 3-fold symmetry axis of the closed Env trimer, as previously described in literature.[239] More specifically, we confirmed in Figure 4.4 that PGT145 does not bind to gp120 whereas it binds with nM affinity in 1:1 stoichiometry to SOSIP (Figure 4.6). And finally, PGT151 with the epitope

at the gp120-gp41-interface[240], was confirmed to not bind to gp120 alone, but showed the previously observed aggregation behavior when being exposed to the gp120-gp41-interface contained in SOSIP (Figure 4.4). Similar to above mentioned observations of vanishing SOSIP peaks for PGV04 and 2G12-D, PGT151 was shown to have pM binding affinity to SOSIP in a previous SPR study and being able to occupy at least two binding sites on SOSIP.[232,236] Although we did not find further evidence to proof our aggregation hypothesis, we suggest that it is a plausible explanation for the disappearance of SOSIP related peaks in certain samples.

Except the observed aggregation, SOSIP-IgG data was in excellent agreement with literature data in terms of affinities and specificity (Table 4.2). Equivalent to the previous gp120 experiments, MP provided additional information regarding the stoichiometry of the complexes which makes the combination of MP and bnAbs a powerful combination to probe different structural states of Env protein.

Although (suspected) IgG induced cross-linking was not a desirable outcome in our MP experiments, it remains one of the key responsibilities of IgG in an immune response. Naturally, IgG have two different modalities (2 identical Fab arms and a Fc-domain), which are used to identify antigens on invaders and mark them for detection by Fc-receptors on immune cells, e.g. T killer cells. Current research in drug development focuses on increasing this "two modalities" concept to three, using a new class of biotherapeutics termed bispecific antibodies (bsAb). An IgG-like bsAb has two different Fab domains and can simultaneously bind to two different types of antigens. Together with the Fc-domain this antibody becomes tri-functional and can bring together tumor cells, cytotoxic T-cells and macrophages which is expected to induce specific immune responses, e.g. against cancer cells.[241]

Beside the ability to cross-link different species, bsAbs could be designed to enhance specificity for just one species, by directing it to two epitopes in close proximity on the surface of the invader. This would result in tighter binding, more specificity and potentially lower doses and less side-effects. In cases such as HIV or cancer, where high mutation rates pose additional challenges for drug development, bsAbs offer a route to prevent or at least delay occurrence of drug-resistance.

Recent, unpublished studies proposed a bsAb consisting of 2G12 and trastuzumab as a promising route for metastatic breast cancer treatment. In more detail, combining the Fab domains of our above tested glycan-targeting IgG 2G12 with one of the most successful breast cancer drugs, trastuzumab, is expected to enhance specificity and affinity compared to trastuzumab. This bsAb would target the Her2 receptor, as well as cancer-specific oligomannose glycans in the proximity of the Her2 receptor. This is supported by ion-mobility mass spectrometry studies which show that oligomannose glycans on cancer cells and the HIV protein gp120 have a similar architecture. Together with ELISA data this shows that the bsAb contains a 2G12 Fab domain and a trastuzumab Fab domain. The exact affinity of both Fab regions for their targets (2G12: glycans, trastuzumab: Her2 receptor), as well as the abundance of bsAb half-molecules or mispaired bsAbs remained unknown.

With MP we set out to quantify this interaction in terms of binding affinities and stoichiometry. More specifically, we wanted to test if we can observe gp120 and Her2 binding to the bsAb, both in 1:1 stoichiometry.

Starting with a purity assessment of all components, we observed high purity for gp120 and Her2 (Figure 4.7, dotted and dotted-dashed lines). MP analysis of bsAb (dotted line) revealed significant impurities, most likely fragments and half-molecules.

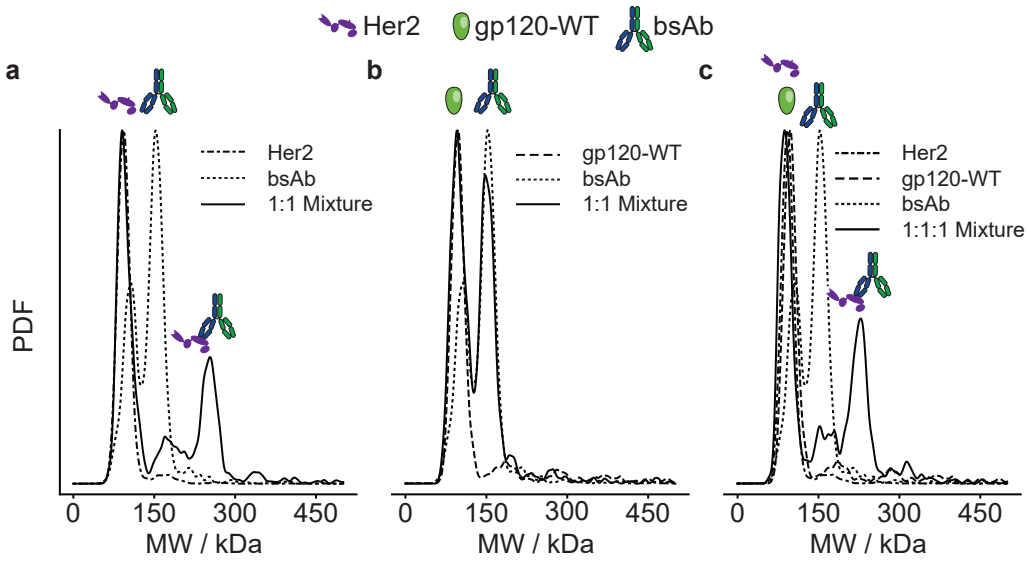


Figure 4.7: MP analysis of bsAb interaction with gp120-WT and Her2). (a) MP analysis of a 1:1 mixture of Her2 (violet) and bsAb (blue/green) revealed a 1:1 complex with an estimated K_d of 1 nM. (b) An equivalent experiment with gp120-WT (bright green) and bsAb showed no detectable complex formation. (c) A 1:1:1 mixture of Her2, gp120-WT and bsAb confirmed previous findings. (a, b, c) Each panel consists of MP data of pure compounds (dotted, dashed and dotted-dashed) and the compounds mixed in a 1:1 ratio (solid). Experiments were performed by mixing compounds at μM, 1-3 hrs equilibration at RT followed by dilution to 11 nM (each) and immediate MP data acquisition for 60 s. Detected counts for experiments were as follows: pure bsAb (2216), pure gp120-WT (1364), pure Her2 (2978), bsAb-gp120 1:1 (1121), bsAb-Her2 1:1 (1566), bsAb-Her2-gp120-WT 1:1:1 (1557).

Following the purity measurements, we showed that Her2 is binding to the bsAb with an estimated affinity of 1 nM in 1:1 stoichiometry (Figure 4.7a). Unfortunately, no binding was observed between gp120 and bsAb under our experimental conditions with final concentrations around 10 nM (Figure 4.7b). These findings were confirmed when analyzing a 1:1:1 mixture of gp120, Her2 and bsAb (Figure 4.7c). Given the unique architecture of intact 2G12, which results in a mono-dentate antibody, it is possible that the high binding affinity of full-length 2G12 towards the glycans on gp120 is lost when only using a half-molecule of un-domain-exchanged 2G12 in the engineered bsAb. Performing additional experiments with SPR at μM concentrations could show

whether the binding affinity just decreased to the μM range or is even further diminished.

4.3 Conclusion and Outlook

We showed at the example of SOSIP (state 1 stabilized Env) that MP can be used to guide sample purification by characterizing purity and oligomerization of SEC fractions. We then went on to showcase at the example of gp120 and SOSIP binding to bnAbs that this experiment can be used to measure binding affinities and stoichiometry against various epitopes on HIV-1-Env. Further work is needed to understand and support our hypothesis that certain antibodies lead to cross-linking of SOSIP.

Beside quantification of binding affinities and stoichiometries the herein presented method can be used to probe the structure and presence of different states of Env. With this we can gain insight in dynamics and structural changes that influence the interaction of Env (in various conformational states) with its target receptors (e.g. CD4), putative drugs or further structural probes (e.g. glycan targeting lectins). Eventually this should help to bring new inputs in the 40 years long quest for an HIV vaccine candidate and more efficient treatments.

We also showed at the example of bsAb analysis with MP, that MP can be used to guide fine tuning of bsAbs as promising drug candidates for HIV therapies. We show with the example of a bsAb candidate for cancer treatment that simple and quick MP experiments can provide important information about sample purity and integrity of bsabs as well as their bivalent binding behavior. Moreover, the concept of the herein investigated bsAb could also be applied in HIV to address the problem of fast mutation rates and their impact on drug-resistance.

Finally, we would like to highlight aspects, which go beyond the herein shown experiments and instrumentation. Specifically, MP fulfills some prerequisites which make it highly suitable for high-throughput screening. In more detail, short measurement times, minute sample consumption, low-cost sample carriers and automated data analysis are just waiting to be combined with a robotic system for sample handling. With this high-throughput screening of protein-protein interactions and potential drug candidates, be it small molecules or larger biomolecules, could bring significant advances in the development of new therapies against HIV.

4.4 Methods

4.4.1 Sample preparation

anti-HIV-1 gp120 monoclonal antibodies (PG9, 17b, b12, PGT145) and anti-HIV-1 gp41 monoclonal antibody (4E10) were obtained from the NIH AIDS Reagent Program. 2G12-M and 2G12-D were expressed and purified as described in Soltermann et al.[155]. PGV04, PGT151 and PGT128 were obtained from Katie Doores, King's College London. Gp120 was expressed and purified as described in Struwe et al.[242]. HIV-1 BG505 SOSIP.664 was expressed and purified as described in Struwe et al.[243] Her2 (ErbB2) human recombinant was purchased from Sigma-Aldrich. All samples were buffer exchanged to into phosphate buffered saline (Gibco® DPBS) prior to use.

4.4.2 MP experiments

Binding experiments were performed at concentrations displayed in the figures and according to the experimental procedure described in Chapter 3. For data acquisition and image processing the OneMP instrument and DiscoverMP software from Refeyn, Oxford was used. Binding affinity calculations were

performed as described in Chapter 3. Briefly, observed peaks where used to define a binding model (e.g. 1:1 or 1:2). Afterwards, relative peaks intensities in MP data, combined with known total concentrations from UV absorbance measurements where used to calculate molar concentrations of bound and unbound species. In this way estimates of binding affinities (K_{d}) were obtained.

Chapter 5

Characterization of Glycoproteins and their Interactions by MP

In this chapter Siyun Chen, Robinson Group, Oxford performed the stepwise deglycosylation procedure of t-PA and etanercept and performed the native MS data acquisition of both t-PA samples.

5.1 Introduction

In eukaryotes, the relatively strict and almost template-like translation from DNA to RNA to protein is followed by a less predictable attachment of sugars (glycans) to the peptide backbone. Together with lipids (e.g. GPI-anchors), glycans are the major posttranslational modification on proteins and allow cells to develop a complex proteome from a relatively small number of genes.[244] The diversity and heterogeneity of glycans makes the development of complex organisms possible by mediating interactions, such as cell-cell, cell-matrix or cell-molecule to simple protein-protein interactions.[245] In this way glycans and glycoproteins ensure function of complex organisms, but can also be related to disease when malfunctioning[246–251] or when mediating interactions between hosts and pathogens[25,238,252,253].

Before regulating functions on various levels, glycoproteins themselves are produced in a highly controlled, but non-templated manner in the endoplasmatic reticulum (ER) and Golgi. In humans, glycosylation on glycoproteins are classed in two major categories, N-linked glycans or O-linked glycans (Figure 5.1a). N-glycans are attached via the nitrogen atom on an Asn side chain, and contain the characteristic $GlcNAc_2$ Man_3 core, where GlcNAc stands for N-acetylglucosamine, and Man for mannose. As larger precursor ($Glc_3Man_9GlcNAc_2$, where Glc means Glucose), oligosaccharyltransferase attaches the glycan at the specific Asn-X-Ser/Thr site (where X is can be any amino acid except proline) to the protein in the ER. As part of the transfer from ER to the Golgi the Glc are removed and can be further trimmed with mannosidases in the Golgi (Figure 5.1b). At this stage we differentiate between high-mannose and hybrid-glycans. Complex-glycans are obtained in the next step in the Golgi, if GlcNAc, galactose, sialic acid or fucose is added. In contrast to N-glycans, O-glycans follow a sequential addition process in the Golgi and lack the trimming step. O-glycans are attached to oxygen atoms in hydroxyl groups of Ser and Thr and are mostly GalNAc and GlcNAc glycans. Glycosyltransferases can further extend these structures by attaching galactose, GlcNAc, sialic acid or fucose.[254] Overall, this modular principle of glycans, together with stereo-centres at the linkages and enzymes with different site preferences gives rise to the structural diversity of glycoproteins.

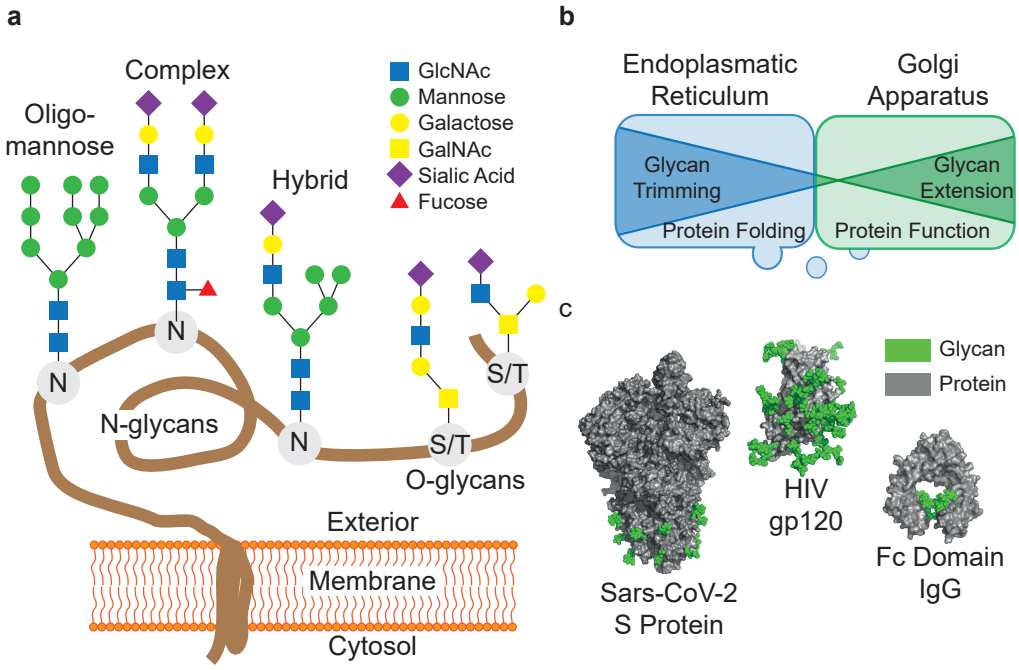


Figure 5.1: Glycoprotein overview. (a) In glycorproteins, glycans are attached to the protein via the nitrogen atom on Asn (N-glycans) or the oxygen atom on Ser or Thr (O-glycans). N-glycosylation can be categorized in oligomannose-, complex- or hybrid-type, whereas O-glycans can be always considered complex-type. (b) N-glycan maturing takes place in the ER or Golgi, whereas O-glycans are gradually attached in the Golgi. (c) The degree of glycosylation can vary dramatically between proteins, ranging from 1-2 glycans in antibodies, to glycan-shield like structures in HIV or SARS-CoV-2 spike proteins.

With the structural diversity comes the functional diversity which gives glycoproteins critical roles in health and disease. On one side this makes glycoproteins interesting targets for drug development but also incredibly difficult to analyse, characterize and reproducibly manufacture.

Whereas monoclonal antibodies, the most prominent class of biotherapeutics, have only a few percent of their molecular weight contributed by glycans, more complex glycoproteins can have large glycan portions with 20 to 50 % of the molecular weight (Figure 5.1c). Such examples can be found in successful biotherpeutics[255,256], but also in pathogens, such as in virus spike proteins of HIV[242] or SARS[25].

On one hand, glycosylation on biotherapeutics can help to increase stability,

specificity and *in vivo* efficacy[257], on the other hand glycosylation in disease states or pathogens allows for immune evasion and fast mutation rates.[258,259] Improving the characterization of glycoproteins, their structure and interactions will help to better understand processes in health and disease and ultimately contribute to more effective therapies.

In a first step, current glycoprotein characterization methodologies aim to confirm the presence of glycans and their type with a combination of gel electrophoresis and endo- or exoglycosidases.[260] Unfortunately, the heterogeneity of intact glycoproteins often results in diffuse gel bands or smearing over a wide molecular weight range. Determining exact molecular weights and oligomeric states is therefore often impossible. To probe a protein for glycosylation enzymes with various specificities are available. After enzymatic treatment of the glycoproteins sharper bands in gel-electrophoresis indicate successful deglycosylation. Removal of N- or O-glycans is performed with endoglycosidases (PNGase F, Endo H, Endo F, or for endo-α-N-acetyl galactosaminidase for O-glycans). Glycan residues can also be gradually cleaved from the tip to the core by exoglycosidases, such as sialides or β-galactosidase.[255,256] Low mass resolution, combined with smearing and the need for denaturation limit the usage of gel electrophoresis experiments, especially when it comes to oligomeric state or interaction studies.

For sparsely glycosylated proteins, native mass spectrometry approaches offer high mass resolution of glycosylation patterns even for intact proteins. Similar to gel electrophoresis, mass spectrometry of intact glycoproteins with several glycosylation sites often struggles with the heterogeneity of the sample[255,256], resulting in unresolvable spectra and finally unknown molecular weight.[242] Reducing complexity of the sample with endo-or exoglycosidases can help to overcome this limitation but takes away the "native" character of

the experiment. Complete or partial removal of glycans is expected to directly affect the affinity to ligands in interaction experiments.[155,261]

In a next step, current methodologies would focus on the identification of the general type of glycans, the determination of glycan composition, configuration and position of linkages and their location on the protein.[260] These methods include enzymatic/chemical release of glycans, separation (SEC, SAX, WAX, HPLC, CE) and further structural analysis with high-resolution techniques such as MS or NMR.[260]

In the context of this chapter we investigate the suitability of mass photometry to complement existing methods for characterization of glycoproteins at the intact level. We assess the accuracy of molecular weight measurements and determination of oligomeric states in denaturation-free MP experiments in physiological buffer with minute sample consumption and fast experimental procedures. At the example of Alteplase we demonstrate how MP can be used as a fast and accurate method for identification of glycans on glycoproteins. We then extend these applications to interaction measurements of etanercept and its target TNF-alpha, which highlights a limitation of MP. Finally, we combine the findings from this chapter and the work published by F. Soltermann et al.[155] to support the world-wide effort to tackle the COVID-19 health-crisis. For this, we look at interactions of glycoproteins involved in the host cell entry by the SARS-CoV-2 virus.

5.2 Results and Discussion

Although we already studied glycoproteins with MP in previous chapters, we wanted to investigate the achievable mass accuracy, ability to determine oligomeric states and quantify protein interactions in detail with MP.

First and foremost, we studied the mass accuracy of MP at the example of 9 glycoproteins (Figure 5.2). As reference standards, we used average masses obtained from native mass spectrometry measurements. For glycoproteins with low amounts of glycosylation native MS yielded resolved spectra with narrow mass distributions (e.g. transferrin in Figure 5.2a, b).

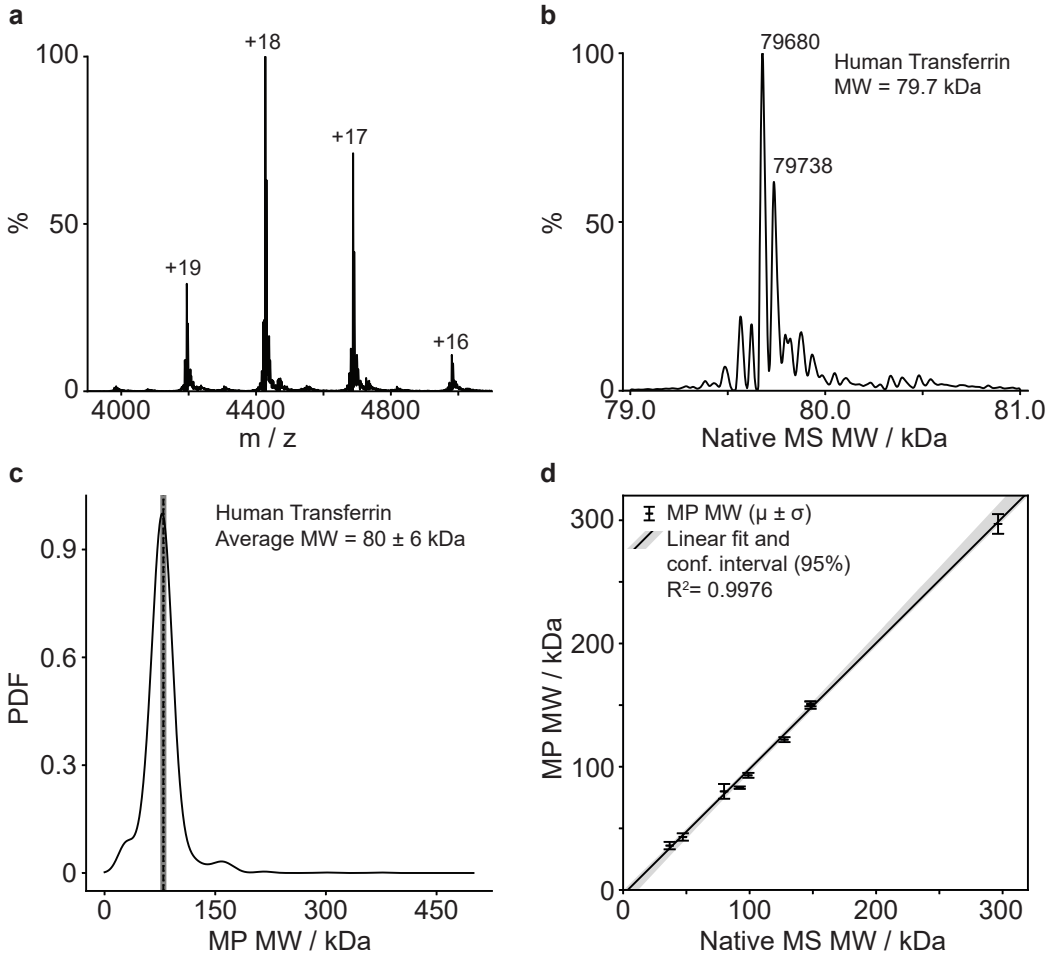


Figure 5.2: Glycoprotein molecular weight of MP vs. native MS. Molecular weight determination of glycoproteins with MP vs. native MS. (a) Native MS spectra of human transferrin, (b) zero-charge spectra of transferrin, (c) MP data and the corresponding data for a set of 9 glycoproteins measured with MP and native MS. With a slope value of 1.02 and strong linear correlation (R^2= 0.9976) we confirm that MP accurately measures molecular weights of glycoproteins. Proteins from left to right: α1-acid glycoprotein (AGP), fetuin, transferrin, haptoglobin 1-1, gp120 (kifunensine expressed), Etanercept, Herceptin, 2G12-WT monomer and 2G12-WT dimer (d).

For heavily glycosylated proteins, such as gp120 (50% w/w) or etanercept (20% w/w), native MS struggled to provide highly-resolved charge states. In an alternative approach we used versions of glycoproteins with simplified glycosylation patterns. For gp120 we obtained more homogeneous glycosylation by expressing it in the presence of kifunensine.[242] Kifunensine is a potent inhibitor of class 1 α-mannosidase, which prevents trimming of mannose residues in the Golgi and results in $Man_9GlcNAc_2$-oligomannose glycans. For etanercept we eventually used the mass of the intact molecule by taking the mean m/z values of charge states to obtain a molecular weight of 128 kDa, which corresponds to recently published literature.[255] For a control experiment, we desialidated the molecule with sialidase, which resulted in a resolved mass spectrum and a molecular weight of 119.1 kDa.

In a next step, we compared the obtained molecular weights of MP and native MS (Figure 5.2c). Linear regression with a slope of 1.02 and a R^2 value of 0.9976 confirmed the expected slope of 1 and indicated strong linear correlation. In an attempt of confirming these findings on a theoretical level, we looked at the difference in refractive index increments between glycans and proteins. Refractive index increment values (dn/dc) obtained from surface plasmon resonance[262], suggest that dn/dc values between average proteins (dn/dc=0.18) and average polysaccharides (dn/dc= 0.15) vary by ca. 15%. For the most extreme case in our experiments, gp120, 50% of the molecular weight are glycans. Here, MP should underestimate the molecular weight of gp120 by ca. 7.5%. Indeed, we observe that native MS of gp120-KIF yields a MW of 99 kDa, whereas MP measures 93 $\pm$ 2 kDa, which corresponds to an underestimation of ca. 6%. All other glycoproteins of our experiment have a glycan content of 20% or significantly less. In these cases, we expect underestimations to disappear in the experimental error of an MP measurement.

Having shown that MP measures single oligomeric states with good accuracy, we then went on to quantify molecular weight distributions and comparing results between MP, native MS and literature (Figure 5.3).

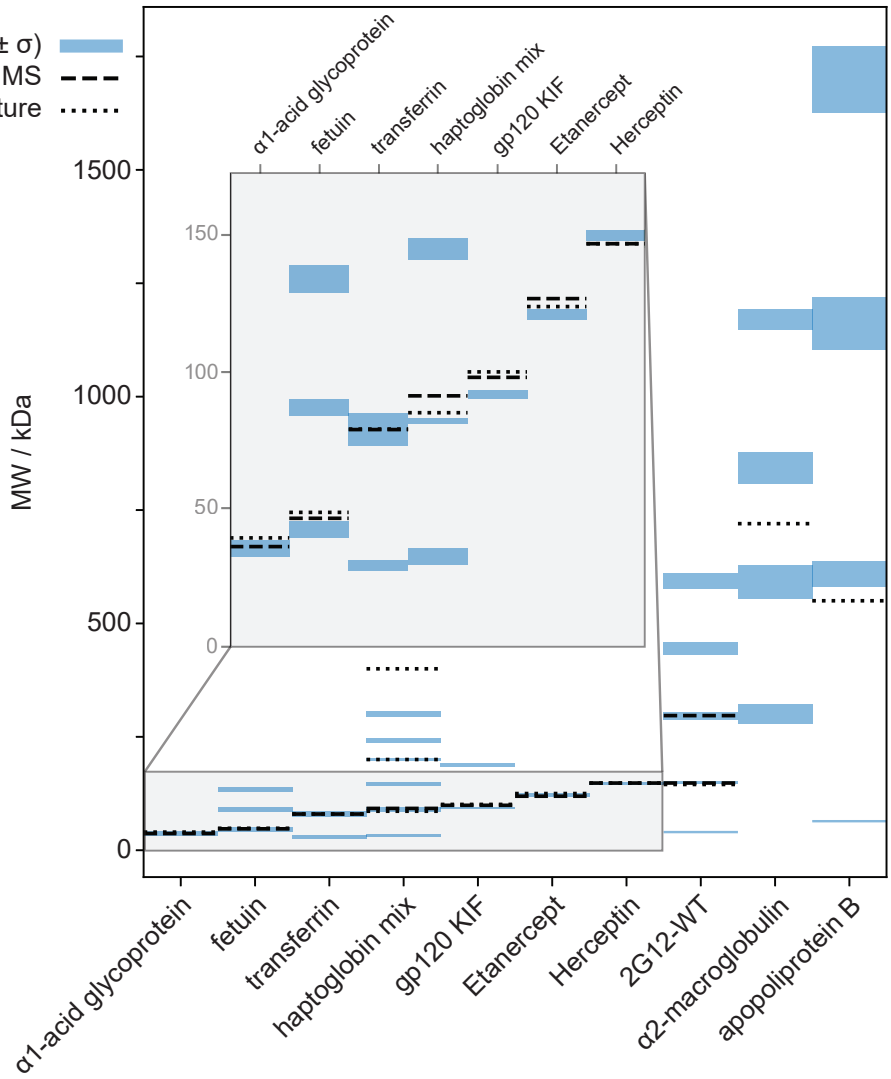


Figure 5.3: Comparison of glycoprotein mass measurements with MP (blue), native MS (dashed) and literature (dotted). Measured proteins included (from left to right): α1-acid glycoprotein (AGP), fetuin, transferrin, haptoglobin mix (1-1, 1-2, 2-2), gp120 (Kifunensine expressed), Etanercept, Herceptin, 2G12-WT, α2-macroglobulin and apopoliprotein B. MP revealed several oligomeric states which were not detectable with native MS and/or not reported in literature.

Inspired by SDS-PAGE gels, we display the oligomeric states as MW bands, with the width corresponding to the standard deviation (Figure 5.3, green

bands). For comparison we show MP, native MS (dashed) and literature data (dotted). From this data we see that MP detects oligomeric states over a molecular weight range from 40 up to 2000 kDa. Many of these states were previously unreported. Beside the molecular weight determination, we can use the relative peak intensities to quantify relative abundance of different oligomeric states, as described in previous studies.[4,155] This also represents a powerful alternative to gel-electrophoresis approaches, because results can be obtained instantaneously, with higher sensitivity and without denaturation.

As mentioned in the introduction, gel electrophoresis combined with enzymatic removal of glycans is often the first step to identify glycoproteins and the type of glycans. In Figure 5.4, we show this principle applied to MP at the example of Alteplase (t-PA).

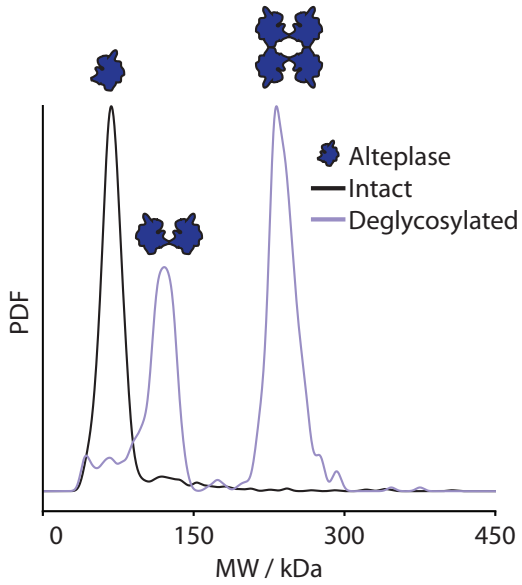


Figure 5.4: Influence of glycosylation on t-PA (Alteplase) oligomeric states. Intact t-PA, with 3 glycosylation sites, is present as monomer with a molecular weight of 66 ± 3 kDa, which agrees with native mass spectrometry data (63 ± 1 kDa). After deglycosylation with neuraminidase, galactosidase, N-acetyl glucosaminidase and mannosidase, t-PA is present as dimer and tetramer, with molecular weights of 121 ± 3 and 240 ± 6 kDa, respectively. Measurements were performed at 5 nM, with average counts of 1200 and 6 replicates.

Interestingly, sequential digest with neuroaminidase, galactosidase, N-acetyl glucosaminidase and mannosidase did not only lead to removal of glycans, but also to disappearance of t-PA monomer and formation of dimer and tetramers. Looking at this in more detail, we see that the mass of intact t-PA with up to 3 glycosylation sites (66 ± 1 kDa) corresponds well to literature (60-70 kDa) and native mass spectrometry (63 ± 1 kDa). The mass of deglycosylated t-PA dimer and tetramer (121 ± 3 and 240 ± 6 kDa resp.) was in partial agreement with native mass spectrometry. Native MS of deglycosylated t-pA yielded poorly resolved charge states. Processing with UniDec revealed a broad mass distribution from ca. 112 to ca. 127 kDa. A second charge state distribution at higher m/z was suspected, but could not be resolved.

According to literature t-PA has 2 to 3 N-linked glycans, where one to two are complex glycans and one oligomannose type.[263,264] From the applied enzymes we expected that glycans are trimmed down to the core, leaving 1.8 to 2.7 kDa of sugars on the protein. This suggests an expected mass of 60.8 to 61.7 kDa for our deglycosylated t-PA. This is in good agreement with the experimentally determined 60.5 ± 1.5 kDa by MP. Moreover, a comparison of MP data of intact and deglycosylated t-PA suggests a weight loss of 6 kDa per monomer.

In a biological context this data might also help to explain the reduced enzymatic activity and enhanced plasma clearance of deglycosylated t-PA.[263] Reduced plasma clearance was observed upon deglycosylation of t-PA with Endo-H, whereas plasma clearance was enhanced by high-oligomannose glycans, most likely due to the immune mannose receptor.[265,266] Changes in enzyme activity were observed when treating t-PA with neuroaminidase and β-galactosidase (decreased activity) and α-mannosidase (increased activity).[267] We suggest that formation of oligomers, as observed in our experiments, might

slow down plasma clearance. Additionally, hindered accessibility of oligomerized t-PA could lead to reduced enzyme activity.

We then attempted a similar approach with the heavily glycosylated Fc-fusion protein etanercept (Figure 5.5). Etanercept is used for treatment of autoimmune diseases, such as rheumatoid and psoriatic arthritis by inhibiting the tumor necrosis factor (TNF). Its structure is composed of the TNF-α receptor coupled to the Fc-domain of a human IgG-1 and carries in total 6 N-glycans (2 on the Fc domain, and 4 on the TNF-α receptor) and 18-21 O-glycans (on the TNF-α receptor).[255,268] Intact mass with MP and native MS yielded 122 $\pm$ 2 kDa and 128 kDa respectively. This is, within the experimental error, in accordance with the expected underestimation of molecular weight due to glycosylation. Sequential treatment with neuraminidase, galactosidase and N-acetyl glucosaminidase resulted in a molecular weight loss of approximately 8-13 kDa, this is an agreement with native mass spectrometry (13 kDa) and estimated values derived from literature (ca. 10-15 kDa).[255]

Unexpectedly, deglycosylation, especially removal of negatively charged sialic acids, did not affect the oligomeric state of etanercept (Figure 5.5, middle and right). This suggests that reported effects of deglycosylation on stability might need further deglycosylation or need to be measured at higher concentrations.[269] On the other hand, expected was our observation that deglycosylation has no effect on binding affinity to TNF-α, due to spatial separation of binding and glycosylation sites. Although MP data directly reveals high binding affinity of this interaction, with an estimated K_{d} in the sub-nM range, we could not confidently determine a specific value. Molecular weight interference at 120 kDa, combined with very strong binding, did not allow us to determine contributions of unbound etanercept and the hexamer of TNF-α to the low abundant peak at 120 kDa. This could potentially be

overcome by SEC-purification of TNF-α, if TNF-α oligomers are not in an equilibrium.

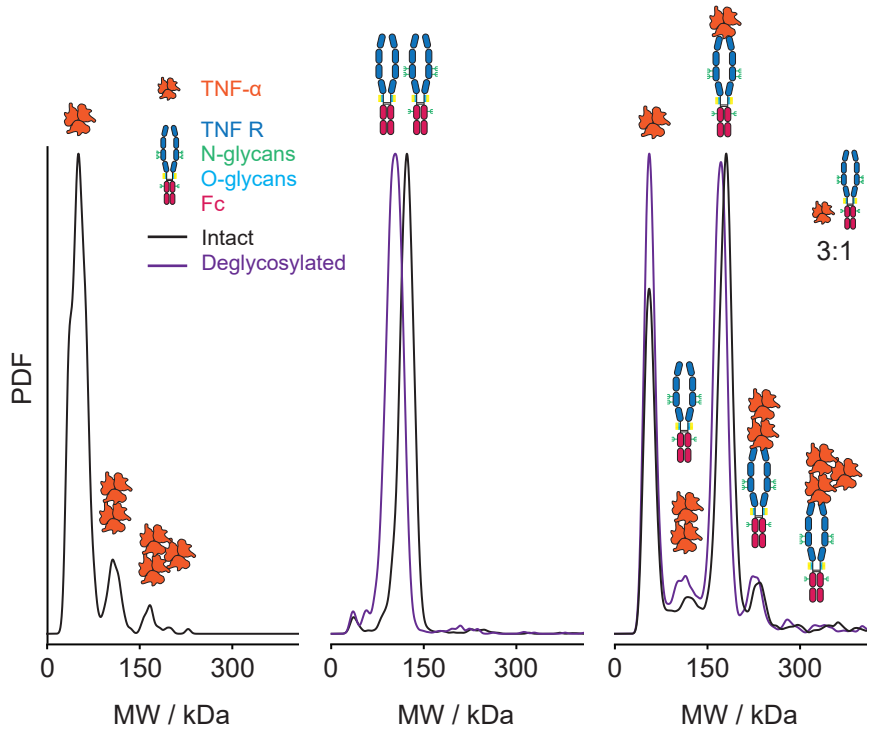


Figure 5.5: Interaction study of etanercept and TNF-α. MP interaction study of etanercept and TNF-α. (left) Pure TNF-α at concentration of 12 nM homotrimer (52 ± 2 kDa), showing presence of homohexamer (104 ± 1 kDa) and homononamer (159 ± 6 kDa). (middle) Pure etanercept at concentration of 6 and 5 nM for intact (black) and deglycosylated (violet) protein respectively. Deglycosylation was performed stepwise with neuraminidase, galactosidase and N-acetyl glucosaminidase. (right) Etanercept and TNF-α (1:3) at a final etanercept concentration of 8-10 nM. Molecular weights of etanercept (122 ± 2 kDa for intact, 111 ± 1 kDa for neuraminidase, galactosidase and N-acetyl glucosaminidase treated) were within experimental errors and deviations induced from refractive indices differences of amino acids and glycans in accordance with native MS data (128 kDa for intact, 119 kDa for disialyted and 115 kDa for neuraminidase, galactosidase and N-acetyl glucosaminidase treated etanercept). K_d values could not be determined accurately due to a mass interference around 120 kDa. However, the data suggests strong binding of 3-mer, 6-mer and 9-mer of TNF-alpha to etanercept with K_ds stronger than nM. As expected, removal of N-glycans in the TNF-R and Fc region did not affect the binding affinity to TNF-α.

Applying our method further to myeloperoxidase (MPO) in a collaborative project, resulted in a contribution to the publication of H. C. Tjondro et al.[270].

MPO is a microbicidal glycoprotein with a crucial role in fighting pathogens by generating reactive oxidation products. Tjondro et al. characterized the structure-biosynthesis-activity relationship of neutrophil MPO (nMPO) with an integrated biomolecular analytics approach (native mass spectrometry, glycopeptide profiling and mass photometry) and report novel functional roles of MPO glycans. Ultimately, their research provides new insight into neutrophil-mediated immunity. They showed that MPO is a glycoprotein with highly heterogeneous N-glycosylation on all five glycosylation sites. Mass photometry measurements of nMPO revealed the presence of a low-abundance monoprotomer and a high abundance diprotomer, with a K_{d} in the low pM range (Figure 5.6). These findings were confirmed by native mass spectrometry and cooled non-reductive SDS-PAGE followed by peptide profiling. The biological significance of the maturely processed monoproteomeric MPO remains unknown, but findings are expected to further guide glycoengineering efforts to construct MPO products with therapeutic effects against severe pathogen infections.

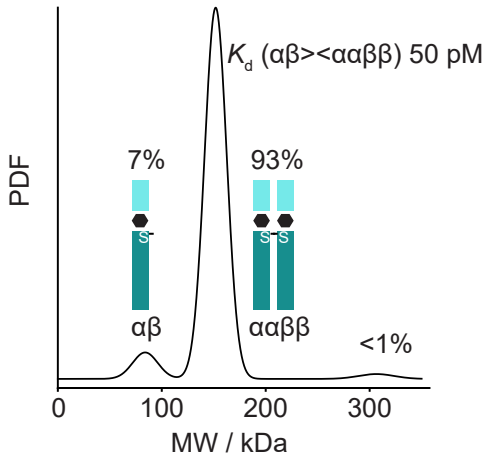


Figure 5.6: MP analysis of neutrophil granule myeloperoxidase. The presence of a previously unreported low-abundance monoprotomer (7%) and a high-abundance diporotomer (93%) of nMPO is revealed. Measurements were performed at 10 nM final concentration after dilution from 4 μM and 20 min equilibration resulting in 520 total counts and an estimated K_d in the low pM range.[270] This figure is adapted from H. C. Tjondro et al., Hyper-Truncated Glycans Augment the Activity of neutrophil granule myeloperoxidase, *bioRxiv*, 2020, 2020.07.24.219956.[270] Adapted with permission from author.

5.3 Conclusion and Outlook

In conclusion, our results show that MP can indeed quantify molecular weights of glycoproteins with high accuracy. We suggest that an underestimation of molecular weight in the range of a few percent should be expected when measuring heavily glycosylated proteins with MP. We then showed that the same approach can be used to quantify oligomeric states and interactions of glycoproteins. This information can be hard or even impossible to assess with techniques such as native MS and SDS-page due to the heterogeneity of glycosylation patterns. In this context, MP offers lower resolution then native MS but is not limited by the complexity of the glycosylation patterns. Moreover, measurements can be performed in a wide range of physiological buffers, with minute sample amounts and with simple and short experimental procedures.

In combination with endo- and exoglycosidases MP can be used to probe glycoproteins and identify types of glycans similar to well-known gel electrophoresis and mass spectrometry based assays.

In the future we expect MP to become a routine analysis method for glycoprotein characterization. It will help to complement existing methods thanks to its combination of acceptable mass resolution and accuracy together with broad buffer compatibility and ability to measure even complex glycoproteins, oligomers and their interactions.

5.4 Methods

5.4.1 Materials

α1-acid glycoprotein from human plasma, fetuin from fetal bovine serum, transferrin human, haptoglobin plasma (mixed type) from human plasma, apolipoprotein B from human plasma, α2-macroglobulin from human plasma, tumor necrosis factor-α human expressed in HEK239 and tissue plasminogen activator human were purchased from Sigma. Trastuzumab (Herceptin) and etanercept (Enbrel) were purchased from Oxford University Hospital. The 2G12 antibody (2G12-M and 2G12-D) was expressed and purified as described previously[212] and in section 3.4.2. Antibody monomers and dimers were then separated with size exclusion chromatography (HiLoad Superdex 16/600 200 pg, GE Healthcare) and fractions collected according to the SEC profile and mass photometry data. gp120 was expressed and purified as described previously.[242] Briefly, BG505 SOSIP.664 gp120 was transiently expressed in HEK293F cells in presence of 20 umol/l kifunensine and purified by nickel affinity chromatography (HisTrap HP column, GE Healthcare), buffer exchanged into PBS and purified by SEC (HiLoad Superdex 16/600 200 pg, GE Healthcare) and fractions collected according to the SEC profile and mass photometry data. Exoglycosidases

(α2-3,6,8,9 Neuraminidase A, β1-4 Galactosidase S, β-N-Acetylglucosaminidase S, α1-2,3,6 Mannosidase) were purchased from New England BioLabs. Deglycosylated tissue plasminogen activator human was obtained after sequential treatment with neuraminidase, galactosidase, N-acetyl glucosaminidase and mannosidase, according to manufacturer's instructions. A similar procedure (without mannosidase) was applied to obtain deglycosylated etanercept.

5.4.2 Native Mass Spectrometry

Prior to mass spectrometry analysis, glycoprotein samples were buffer exchanged into 1 M ammonium acetate, pH 7.0, with Bio-Spin 6 columns (Bio-Rad), further desalted in 5 sequential washes of 1 M ammonium acetate, pH 7.0, with 10 kDa MWCO centrifugal spin filters (Amicon Ultra 0.5 ml centrifugal filters, Merck), with a final buffer exchange into 200 mM ammonium acetate, pH 7.0. Concentrations were adjusted to 1-10 μM. Samples were introduced into a Q-Exactive hybrid quadrupole-Orbitrap mass spectrometer (Thermo Fisher Scientific, Germany), modified for the transmission and detection of high molecular weight ions. Positive ions were generated by static nano-ESI using gold-coated capillaries prepared in-house. The typical MS settings were spray voltage of 1.1 to 1.3 kV, source fragmentation of 50-150 V, source temperature at 50 °C, HCD collision energy turned off, and backing pressure at ca. 6*10-10 mbar. Data was processed with Xcalibur 4.1 software (Thermo Fisher Scientific, Germany) and masses were assigned manually with in-house software. Deconvolution to zero-charge spectra was performed with UniDec software.[215] Average masses were used for comparison with literature and mass photometry.

5.4.3 Mass photometry

Protein stock solutions were prepared as described previously.[155] For binding experiments, μM stock solutions were mixed and incubated for 2 hrs at RT, followed by dilution to nM concentrations and equilibration for 30 min, at ratios and concentrations shown in Figure 5.5. Mass photometry analysis was performed as described previously.[155]

Chapter 6

Glycoprotein Interactions in SARS-CoV-2

This project was started following the COVID-19 outbreak and overcame several COVID-19 related hurdles, especially significantly reduced access to laboratories over several months. Different people contributed to the specific results presented in this section as following: Experiments were planned in a collaborative effort, shared between Anna Olerinyova, Fabian Soltermann, Manish Kushwah and Weston B. Struwe. Experiments in gaskets were performed by Anna Olerinyova and data analysis performed by Fabian Soltermann. Experiments with a microfluidic system for pM and low nM concentrations were performed and analyzed by Fabian Soltermann. Data analysis performed by Fabian Soltermann included Gaussian fitting, K_{d} quantification with single-shot method (see Chapter 3) and "traditional" binding curve fits. Figures and text were created by Fabian Soltermann. SARS-CoV-2 S protein, mACE2 and ACE2 were kindly provided by Snezena Vasiljevic, Oxford Glycobiology Institute, Oxford and Mario Hensen, Oxford Antiviral Drug Discovery Unit, Oxford.

6.1 Introduction

SARS-CoV-2 is a novel coronavirus which sparked a global pandemic, with 1 million fatalities reported to the WHO by October 2020. Similar to other corona viruses or HIV, SARS-CoV-2 (severe acute respiratory syndrome coronavirus 2) initiates infection via binding of the spike glycoprotein (herein referred to as S protein) to the host cell, followed by viral and host membrane fusion. Due to its central role in infection the S protein became the main target for neutralizing antibodies and vaccine development. Recent efforts have focused on the expression and characterization of the pre-fusion state to understand conformational dynamics, structural details and interactions.[25,271] The pre-fusion state S protein used by Wrapp et al.[25] for their cryo-EM study (and for the herein presented MP study) was shown to be an asymmetric trimer with one out of three receptor binding domains (RBD) in the up conformation (Figure 6.1a, inset and 6.1b, top).

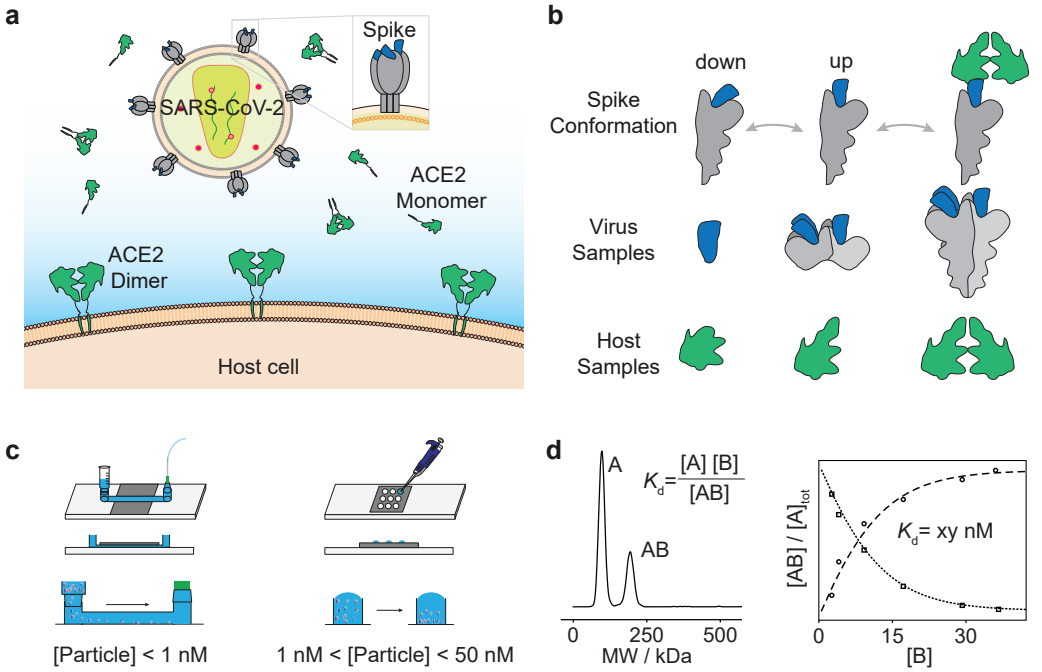


Figure 6.1: Overview of PPI studies in SARS-CoV-2 host cell entry by MP. (a) The first step in the virus entry into the host cell is the binding of the densely glycosylated S protein to the host cell receptor ACE2. (a, inset and b) The pre-fusion state of the S protein trimer protein from Wrapp et al.[25] has one of three receptor-binding domains (RBD, blue) in a receptor-accessible "up-conformation". (b, bottom) Its binding partner, ACE2, is known to be present as monomer and dimer, in solution and on the host cell membrane. (b, centre, from left to right) In order to investigate their interaction, we studied three versions of the S protein (RBD, S1 and full-length S protein) and their binding to (b, bottom, from left to right) neck-domain-free ACE2 and full-length ACE2. (c) For K_d measurements and confirmatory experiments we used a continuous flow system and a gasket-injection system on our MP setup. (d) K_d values were calculated via the single-shot-K_d method and a traditional binding curve fit to titration data.

It was suggested that only RBDs in an up conformation can bind to the host cell receptor angiotensin-converting enzyme 2 (ACE2) (Figure 6.1b). As a type 1 membrane protein, ACE2 is present on several human tissues, especially in the lung, intestines and heart.[272] Its primary physiological function is in the degradation of angiotensin II, a peptide hormone responsible for vasoconstriction and blood pressure control.[273,274] Recent literature suggests that ACE2 is present as homodimer, with dimerization primarily mediated by the neck domain.[272] Furthermore, a soluble, monomeric form of ACE2 can be released

from cell surfaces by proteolytic cleavage with ADAM17 (ADAM metallopeptidase domain 17).[275,276] This shedding of ACE2 together with high ratios of angiotensin II /angiotensin was observed to be an indicator for hypertension in cardiovascular disease.[277] In clinical studies, it was shown that intravenous infusion of recombinant ACE2 reduced the angiotensin II/angiotensin ratio and reflects its therapeutic effect.[277] Inspired by these results, it was suggested that infusion of recombinant ACE2, followed by binding to the S protein could have a protective effect against SARS-CoV-2.[275] It is expected that a better characterization of the ACE2-S-protein interaction, especially stoichiometries and binding affinities, will help to understand whether therapeutic effects of ACE2 could be expected, at least from a biophysical point of view.

The work presented in this section is focused on investigating different designs of ACE2 and S protein and their interactions, *in vitro*. Specifically, we want to employ mass photometry to reveal oligomeric states and interactions of three versions of the S protein (RBD, S1 and full-length S protein) with two versions of the ACE2 receptor (neck-domain free and full-length ACE2), herein referred to as mACE2 and ACE2 (Figure 6.1b). A combination of two injection systems (Figure 6.1c), as described in the work of Soltermann et al.[155] was used to extend the accessible concentration range to pM and confirm equilibrium conditions. The binding affinities were then calculated according to the single-shot K_d method[155] and compared to binding curve fits and literature data (Figure 6.1d).

Following observations made for HIV-1 bnAbs in chapter 4, where we suspected high binding affinity and multiple binding sites to be responsible for disappearance of certain complex peaks (e.g. via cross-linking and eventually aggregation) we were looking for similar evidence here. Specifically, dimeric ACE2 and S protein with 3 putative binding sites could potentially allow for

cross-linking.

6.2 Results and Discussion

In a first step we wanted to understand the sample quality of our pure compounds, specifically molecular weight distributions and their concentration dependence. As described in chapter 3, these experiments are crucial to interpret subsequent binding experiments.

In Figure 6.2 we show that neck-domain free ACE2 (mACE2) is purely monomeric (a) and that the complete ectodomain of ACE2 (b) is in a monomer-dimer equilibrium, as proposed previously.[273] We report here a binding affinity of 12 ± 2 nM, which is, to the best of our knowledge, the first reported binding affinity for the ACE2 monomer-dimer interaction.

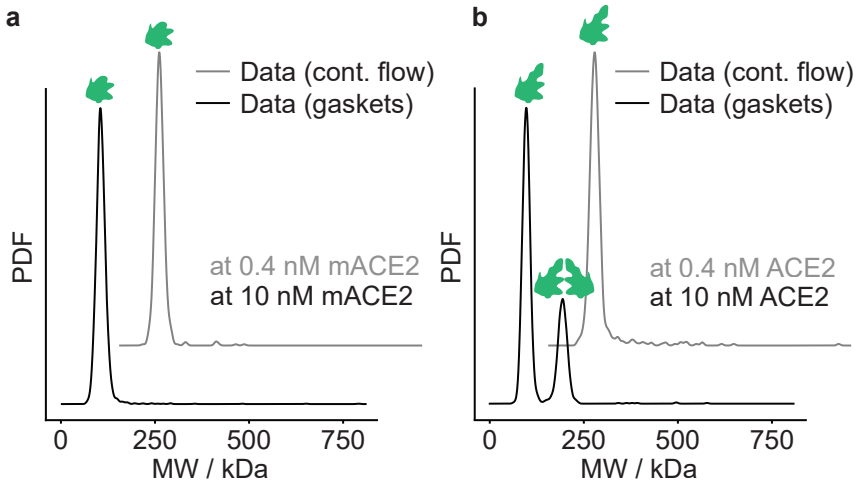


Figure 6.2: MP analysis of mACE2 and ACE2. (a) mACE2 (green) and (b) ACE2 (green) were measured at 0.4 nM (grey) and 10 nM (black). For ACE2 a monomer-dimer K_d of 12 ± 2 nM was obtained based on 4 repeats in gaskets at 10 nM. Two repeats with the continuous flow injection system were performed at 0.4 nM to confirm dissociation of the dimer upon dilution. Experiments were performed as described in Soltermann et al..[155] Data shown are representative MP measurements with 593, 2043, 555 and 1489 counts for mACE2 0.4 nM, mACE2 10 nM, ACE2 0.4 nM and ACE2 10 nM.

As highlighted previously[155], it is important to confirm equilibrium con-

ditions in K_d experiments with MP (and any other technique). In MP we achieve this by further diluting the sample to concentrations below the K_d, where we expect dissociation of the complex. Given the linear dependence of MP counts and dilution, a 10-fold dilution requires 10-fold longer measurement times, and continuous delivery of sample, as described previously.[155] In Figure 6.2b (grey line), we used the continuous flow injection system to measure ACE2 at sub-nM concentration and observed complete dissociation of complex upon dilution and equilibration. This confirmed that we are looking at non-covalently-bound species and binding affinities within the dynamic range of current MP instrumentation.

We then used the same approach to probe the RBD-ACE2 interaction. In the host cell entry process, the RBD, as part of the S protein would bind to the ACE2 receptor on the cell surface to attach the virus to the cell and initiate membrane fusion.

We started this interaction study by looking at pure RBD first. We confirmed that RBD, with an expected molecular weight of 25 kDa is below the molecular weight detection limit of MP and not present in oligomeric states (Figure 6.3a).

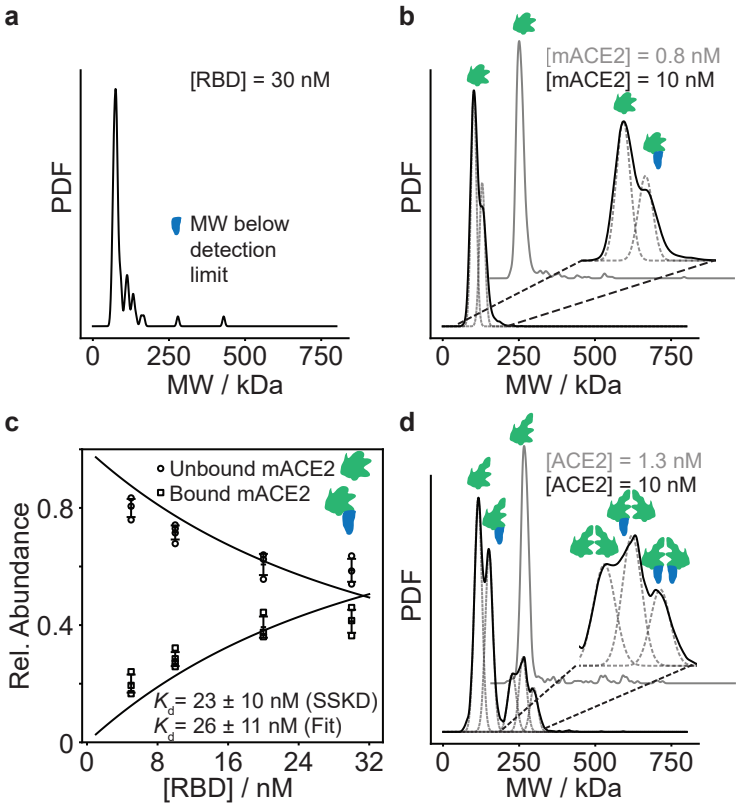


Figure 6.3: MP analysis of RBD interaction with mACE2 and ACE2. (a) The molecular weight of RBD was below the MP detection limit and no oligomers were observed. (b) Representative data of RBD (1, 5, 10, 20, 30 nM) titrated to 10 nM mACE2 with 3 repeats at each concentration (black). Control experiments at 10-fold lower concentration confirmed equilibrium conditions (grey). (c) Calculation of K_d values obtained with the single-shot K_d-method (SSKD)[155] and binding curve fits (black line) were in agreement (K_d = 23 ± 10 nM and K_d = 26 ± 11 nM). (d) Equivalent experiments were performed with ACE2. The SSKD method yielded binding affinities of 31 nM ± 2 nM for RBD-ACE2 monomer, 12 ± 3 nM for the ACE2 monomer-dimer, 18 ± 7 nM for the first RBD binding to ACE2-dimer, 40 ± 15 nM for the second RBD to ACE2-dimer (black). Control experiments at ca. 10-fold dilution confirmed equilibrium conditions (grey). Further data description: (a) black: 67 counts, 30 nM RBD, (b) black: 5913 counts, 30 nM RBD, 10 nM mACE2; grey: 521 counts, 2.4 nM RBD, 0.8 nM mACE2, (d) black: 3517 counts, 30 nM RBD, 10 nM ACE2; grey: 354 counts, 4 nM RBD, 1.3 nM ACE2. Dotted lines represent Gaussian fits to peaks used in SSKD method.

Performing a titration series with varying concentrations of RBD to mACE2 revealed an RBD-mACE2 complex with 1:1 stoichiometry (Figure 6.3b). Evaluation of the binding data, with the recently reported SSKD-method[155], yielded a K_d of 23 ± 10 nM. This was in good agreement with the obtained K_d of 26

± 11 nM from a titration binding curve fit (Figure 6.3c) and literature values (5.1 nM in recent BLI study[37]).

From the above reported ACE2 monomer-dimer equilibrium we excepted the RBD-ACE2 interaction to be more complex, which was confirmed by measurements shown in Figure 6.3d. MP revealed the previously unreported co-existence of 5 species, including a complex of 2 RBDs and ACE2-dimer with a binding affinity of 40 ± 15 nM. The binding affinity of the recently reported RBD-ACE2 complex (5.1 nM from BLI) and the K_{d} value obtained by MP (18 ± 7 nM) were in good agreement. Control experiments at 10-times lower concentrations confirmed complete dissociation of the complexes.

So far, the experiments showed, that ACE2, in its dimer form, has two available binding sites, with high affinity for the receptor binding domain of SARS-CoV-2. This suggests that ACE2 could be involved in cross-linking of species containing multiple RBDs.

In order to further investigate the possibility of cross-linking, while keeping the complexity of the virus sample minimal, we continued with a subunit of the S protein, the S1 protein. This protein is expected to be trimeric and contain 3 RBDs.

An MP analysis of the S1 protein showed that it is predominantly present as homotrimer (Figure 6.4a), with sufficient purity to continue with binding experiments. Incubation with mACE2 did not lead to any detectable complex formation (Figure 6.4a). The suspected impurity, observed in (Figure 6.4a), directly interfered with this measurement because it has a similar molecular weight as the potential S1-mACE2 complex.

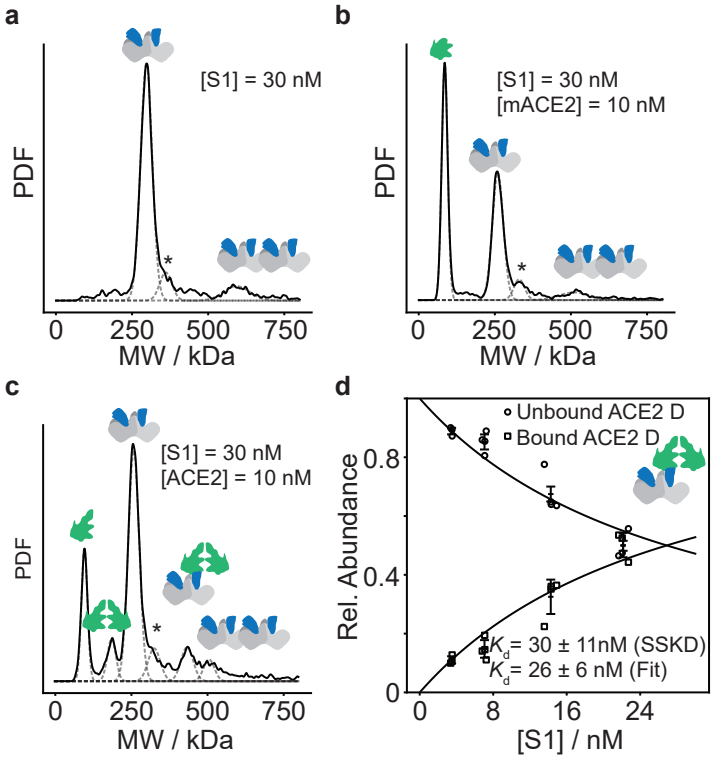


Figure 6.4: MP analysis of S1 protein interaction with mACE2 and ACE2. (a) S1 protein was predominantly present as homotrimer, with minor impurities over the accessible molecular weight range, including a potential, low abundant homohexamer. (b) No measurable binding affinity was observed for the mACE2-S1 interaction. (c) Representative data of S1 (1, 5, 10, 20, 30 nM) titrated to 10 nM ACE2 with 3 repeats at each concentration (black). (d) Calculation of K_d values obtained with the single-shot K_d-method (SSKD)[155] and binding curve fits (black line) were in agreement (K_d = 30 ± 11 nM and K_d = 26 ± 6 nM). Further data description: (a) black: 3584 counts, 30 nM S1 , (b) black: 5072 counts, 30 nM S1, 10 nM mACE2 (c) black: 5443 counts, 30 nM S1, 10 nM ACE2. Dotted lines represent Gaussian fits to peaks used in SSKD method. "∗" denotes an unknown impurity interfering with potential S1-mACE2 peaks.

Interestingly, the same experiment performed with ACE2 revealed formation of a low abundant complex of S1 with ACE2 dimer and a K_d of 30 ± 11 nM (SSKD) and 26 ± 6 nM (binding curve fit), shown in Figure 6.4c, d. These values are in excellent agreement with recently published BLI data (K_d = 34.6 nM)[25].

Formation of complexes with the potential S1 homohexamer were not detectable. This could be related to a lack of activity of this complex, or

could indicate that this peak is an impurity and structurally not related to S1. Looking at manufacturer information of S1, which is only purified by Protein G chromatography, the identity of S1 homohexamer should be further investigated. Alternatively, additional purification steps, such as size-exclusion or antibody-affinity chromatography, could help to remove or confirm S1 homohexamer, but would need significantly larger sample amounts.

Overall, the S1-ACE2 interaction study, showed that we could only see formation of a complex where one ACE2 bound to S1. This data supported previously published findings that only one of three RBDs may be in an accessible up-conformation.[25] Given that our construct (residues 1-674) and the construct used in the previous study (residues 319-591) may be structurally or functionally different we wanted to further investigate this.

For this purpose, we performed an interaction study with the S protein construct used in the previous work.[25] This pre-fusion state ectodomain of the S protein was expressed as described in Wrapp et al.[25], but could not be SEC-purified due to limited sample amounts.

A purity control with MP, revealed impurities over the molecular weight range from 50 to 2000 kDa (Figure 6.5a). This data suggests high abundance of S protein fragments at weights below 500 kDa, and a heterogeneous weight distribution above ca. 600 kDa, potentially related to aggregated S protein and fragments thereof. A control experiment at ca. 20-fold dilution confirmed the stability of S protein, and suggested dissociation of a species with a molecular weight similar to 2 sub-units of the S protein. Overall, these results showed that the S protein sample is of sufficient purity for MP binding affinity measurements, but could lead to difficulties in data analysis when only low abundant complexes are formed.

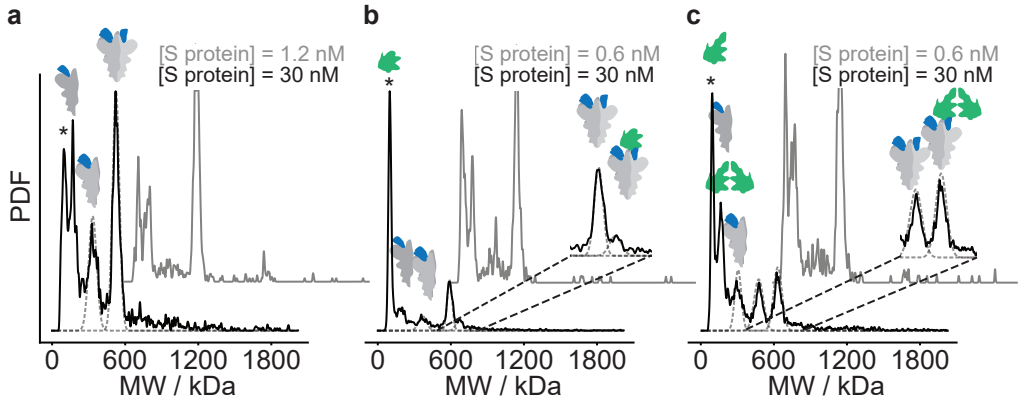


Figure 6.5: MP analysis of S protein interaction with mACE2 and ACE2. (a) S protein was mostly present as homotrimer, with significant low molecular weight impurities and low abundant impurities up to 2 MDa (black). Control experiments at ca. 20-fold lower concentration confirmed stability of S protein (grey). (b) Representative data of S protein (1, 5, 10, 20, 30 nM) titrated to 10 nM ACE2 with 3 repeats at each concentration (black). A K_d value of 23 ± 5 nM was estimated with the SSKD method, but could not be determined with high confidence due to interfering impurities. (c) Equivalent experiments were performed with S protein and ACE2. A K_d value of 0.16 ± 0.07 nM was estimated, indicating high binding affinity (black). Control experiments at ca. 50-fold dilution confirmed equilibrium conditions (grey). Further data description: (a) black: 2165 counts, 30 nM S; grey: 804 counts, 1.2 nM S, (b) black: 4201 counts, 30 nM S, 10 nM mACE2; grey: 471 counts, 0.6 nM S, 0.2 nM mACE2, (c) black: 3581 counts, 30 nM S, 10 nM ACE2; grey: 555 counts, 0.6 nM S, 0.2 nM ACE2. Dotted lines represent Gaussian fits to peaks used in SSKD method. "∗" denotes an unknown impurity interfering with mACE2 peak.

MP analysis of a titration series of S protein added in different ratios to mACE2 showed formation of a low abundant 1:1 complex, with an estimated K_d of 23 ± 5 nM (Figure 6.5b). Control experiments at ca. 50-fold lower concentration suggested dissociation of this low abundant complex upon dilution.

Further examination of relative peak intensities of mACE2 and S protein showed that we generally observe higher counts for mACE2 than for S protein. In Figure 6.5b, black line, MP data of 10 nM mACE2 and 30 nM monomeric S protein, i.e. equivalent to 10 nM of fully assembled, homotrimeric S protein was shown. From this we would expect that mACE2 and fully assembled S protein

should have similar peak intensities in MP data. When taking into account that large molecular weight species, such as the impurities in S protein, contribute more to UV absorbance in concentration measurements but only count as one molecule when detected with MP, the observed deviations from expected MP peak intensities can be partially explained. A further explanation could be small errors in sample preparation (e.g. dilution or mixing). Before investigating more complicated scenarios, such as aggregation or limited binding affinity to the microscope coverslip glass during detection with MP, it is recommended to SEC purify S protein prior to protein-protein interaction analysis with MP.

In an equivalent experiment with S protein and ACE2 we observed formation of a higher abundant 1:1 complex with an estimated $K_{\mathrm{d}} = 0.16 \pm 0.07$ nM. This is ca. 100 times stronger than recently reported in a SPR study (14.7 nM) with identical protein constructs.[25] For SPR experiments they immobilized His-tagged S protein to a Ni-NTA sensorchip and measured binding to ACE2. Incomplete or reversible immobilization as well as reduced on-rates due to steric hindrance are likely to influence the binding affinity measured in this experiment. Assuming accuracy of our experiments, the pM binding affinity could be explained by better accessibility, hence higher on rate, of S protein. MD simulations could help to further investigate if an ACE2-dimer could simultaneously bind 2 RBDs on one S protein.

Although we expected to detect formation of higher order complexes, e.g. 2 S-proteins bound to 1 ACE2-dimer, we could not find evidence for this. In agreement with observations made for mACE2-S protein data from above, we saw a deviation from expected peak intensities of ACE2 and S protein. Given that both experiments were performed in the same way we expect that expressing 10 times larger quantities of S protein, followed by SEC-purification and repetition of our experiments could help to shed light on this.

Overall, the S protein ACE2 experiment showed that a 1:1 complex is formed with high affinity, which is further supporting the findings that this S protein construct has only 1 out of 3 RBDs in an accessible up-conformation.[25] However, our MP data also suggests that there may be other processes ongoing, such as ACE2-dimer induced cross-linking of S protein, which could explain the unexpected deviation of ACE2 and S protein peak intensities in MP data.

6.3 Summary and Outlook

In this chapter, we showed that receptor binding domain containing SARS-CoV-2 proteins (RBD, S1 and S protein), involved in the first steps of host cell invasion, have pM to nM binding affinity for their target receptor on the host cell (ACE2). From a biophysical point of view, this shows that SARS-CoV-2 virus particles are able to bind with high affinity to the host cell membrane to initiate membrane fusion and host cell entry. Moreover, it suggests that recombinant ACE2 could help to neutralize viruses by blocking ACE2 binding sites on the virion before it can reach and infect the host cell.

The binding affinities and stoichiometries of the interactions measured by MP with the single-shot K_{d} method and binding curve fits were in good agreement with recently published literature values obtained by SPR and BLI.

Interestingly, MP offered various new insights. Firstly, we showed that ACE2, which contains the neck-domain, is indeed present in a monomer-dimer equilibrium and reported for the first time a binding affinity (12 $\pm$ 2 nM). Secondly, we found that ACE2-RBD from additional complexes, beyond the previously reported 1:1 interaction. With MP measurements we showed the co-existence of 5 species, all with low nM binding affinities. This suggests that ACE2 has two binding sites with which it could cross-link two S proteins. This phenomenon is expected to be more pronounced at concentrations above

the K_d value, i.e. μM. Thirdly, we found that mACE2 does not show any detectable complex formation with S1 and only a low abundant 1:1 complex with S protein. Fourthly, MP revealed that only the ACE2 dimer showed detectable binding affinity (low nM range) with S1 and S protein construct, leading to formation of a 1:1 complex. This data supports previous findings, that the S protein construct used in our study has only 1 out of 3 RBDs in an accessible up-conformation.

Although we did not observe any higher order complexes, such as 2 S proteins bound to ACE2 dimer or further cross-linking, we observed an unexpected decrease in S protein peak intensity when mixed with mACE2 and ACE2. We attributed this to experimental errors (e.g. mixing or missing dilution step) and the fact that the observe high molecular weight impurities in the S protein sample might lead to high UV absorbance during concentration measurements. Further explanations could be related to aggregation, cross-linking or even limited binding affinity to the coverslip glass surface during MP detection. Potential avenues to improve sample purity could include affinity purification with IgGs and SEC-purification. Having removed low and high molecular weight impurities in the S protein sample will help to quantitatively investigate the above proposed explanations. It is also recommended to further test these hypothesis with complementary methods, such as dynamic light scattering, SEC-MALS or AUC. Unfortunately, these would require substantially large sample amounts, which is often limited by expression capacity. Finally, including different S protein constructs in the MP analysis could show whether the "1 out of 3 RBDs in up-conformation" is an artefact of the used construct in our study, because recent studies with other constructs suggest that up to 3 ACE2 can bind the S protein.[278] Further evidence could be obtained when a different S protein construct would reveal statistically significant reduction of S protein

related peaks in MP data, similar to observations in chapter 4.

Proofing that ACE2 can induce cross-linking or aggregation of S protein remains the focus of future work on this project. This could have significant impact on the wider Covid-19 research. Specifically, it could be a starting point for the development of therapies which focus on the clearance or neutralization of virus particles. In this process, MP results could provide detailed insights into binding affinities and stoichiometries. Similarly, MP could be used to guide drug development for a variety of agents (e.g. small molecules, antibodies or peptides) to arrest host cell receptor binding and membrane fusion.[279]

6.4 Methods

6.4.1 Materials

SARS-CoV-2 S protein, mACE2 and ACE2 were kindly provided by Snezena Vasiljevic, Oxford Glycobiology Institute, Oxford and Mario Hensen, Oxford Antiviral Drug Discovery Unit, Oxford. These proteins were affinity purified against Ni-NTA, and only mACE2 and ACE2 were SEC purified. The RBD protein was a gift from Krammer Laboratory, Icahn School of Medicine, Mount Sinai, New York and the SARS-CoV-2 S1 protein (his-tagged, HEK293) was purchased from TheNativeAntigen Company, Oxford, UK. All samples were present in phosphate buffered saline (Gibco® DPBS).

6.4.2 Mass photometry

For pure compounds (Figure 6.2 a, b, Figure 6.3a, Figure 6.4a, Figure 6.5a) μM stock solutions were diluted to nM concentrations with PBS prior to MP measurements. Due to limited sample quantities mixtures for binding experiments had to be prepared at sub-μM concentrations, followed by a dilution step to low nM concentrations and ca. 15 min incubation prior to

MP data acquisition. These binding experiments (Figure 6.3a, b, Figure 6.4a, b, Figure 6.5a, b) were performed as a titration series with host cell proteins (mACE2 or ACE2) at 10 nM final concentration and varying amounts of viral proteins as binding partner, with final concentrations of 1, 5, 10, 20 and 30 nM. Titration experiments were performed in gaskets as described previously, with 1 min data acquistion.[155] Binding affinity control experiments were performed at sub-nM concentration with a simple microfluidic flow system, with 4 min data acquisition at a flow-rate of 80 μl/min, as described previously.[155] For data acquisition and image processing a custom made instrument[4] and a commercially available OneMP instrument in combination with DiscoverMP software from Refeyn, Oxford was used. Briefly, laser power, AOD frequency (ca. 800 mV and 300 mV for x and y coordinate resp.) and focus were adjusted until a Gaussian illumination profile was obtained and image standard deviation was maximized. Frames were pre-binned 5-fold and pixels 6-fold during data acquisition, followed by 5-fold frame binning in Discover MP with threshold of 1.5 and 0.25 in event finding settings. Gaussian peak fitting in histograms and K_{d} calculation with the single-shot K_{d} method was performed with an in-house Python software analogously to previous experiments.[155] For binding curve fitting of mACE2-RBD and the ACE2-S1 interactions (Figures 6.3c and 6.4d) the built-in fitting model LMFIT in Python was used to fit a 1:1 binding model to experimental data.

Chapter 7

Summary and Outlook

The principal outcome of this work was the development, bench-marking and application of mass photometry based methods to measure purity, stoichiometry, binding affinities and kinetics of protein complexes in a label-free fashion *in-vitro*. Applications focused on protein interaction measurements of biotherapeutical proteins and glycoproteins in cancer, autoimmune disease, HIV and SARS-CoV-2 research.

First, we reviewed the field of established and emerging optical methods for binding affinity measurements of protein protein interactions and presented MP in this context. Broadly, this review revealed the pre-dominance of SPR methods in publications. Moreover, it showed, that an "ideal" technique would be label- and immobilization free, applicable to various biomolecule classes, over several orders of magnitude in molecular weight, binding affinities and kinetics, being able to resolve oligomeric states and stoichiometries, while having low sample consumption, a high degree of automation combined with high reproducibility and ideally high throughput.

In our bench-marking in chapter 3 we found that MP performs well in many of the above listed criteria. More specifically, we showed that we can access binding affinities spanning 4 orders of magnitude from 30 pM to 200 nM, with a time-resolution of 30 s and accessible kinetics from minutes to hours.

Compared to many other techniques, MP can be performed truly label- and immobilization-free in the entire concentration range, consumes only femto moles of sample and is compatible with physiological buffers. Additionally, MP measures the size distributions of the sample with a dynamic range from 40 kDa to several MDa with roughly 2 % precision and accuracy.[4] This allows us to assess oligomeric states and stoichiometries of protein-protein interactions with comparatively high resolution and provides information about the purity of compounds. Recent literature suggests that this method is also applicable to DNA[165] or even membrane proteins[166].

In this bench-marking process we also pointed out current limitations, which include the limited concentration range and time resolution. They restrain MP to binding affinities in the low pM to mid-nM range and kinetics on a timescale longer than minutes. In the future, lower concentrations could be achieved by wider field of views, higher concentrations by faster imaging approaches, or surface passivation. Acquiring images with higher frame rates would require higher laser intensities, which could entail photo-induced sample damage. On the other hand surface passivation requires high control and homogeneity of the passivation reaction, as well as compatibility with or rather resistance against intense laser irradiation. An alternative approach to investigate complexes with μM K_{d}s and often fast dissociation rate constants would be further improvement of microfluidic devices. Here, mixing could be performed within milli seconds, with a MP detector positioned at a certain time point after the mixing step. An efficient microfluidic device would also allow for the extension of the concentration range to the other extreme, i.e. to sub-pM, by offering low sample consumption and better compatibility with the sensitive focusing mechanism of the microscope sample-holder stage.

In chapter 4, we studied protein interactions in HIV. We showed at the

example of gp120 and SOSIP binding to bnAbs that we can differentiate binding affinities and stoichiometry for various epitopes on HIV-1-Env. This method can be used to probe the structure and presence of different states of Env with bnAbs with high specificity. Interestingly we obtained MP data which suggests bnAb induced cross-linking of SOSIP, which could be further investigated with structural methods amd molecular dynamics simulations. In future work, this assay can be used to investigate dynamics and structural changes that influence the interaction of Env (in various conformational states) with its target receptors (e.g. CD4), putative drugs or further structural probes (e.g. glycan targeting lectins). Eventually this could help to bring new inputs in the 40 years long quest for an HIV vaccine candidate and more efficient treatments.

The work on glycoproteins, presented in chapter 5 showed that MP can quantify molecular weights, oligomeric states and interactions of glycoproteins with high accuracy. In combination with endo- and exoglycosidases MP can be used to probe glycoproteins and identify types of glycans similar to well-known gel electrophoresis and mass spectrometry based assays. Additionally, we suggested that an underestimation of molecular weight in the range of a few percent should be expected when measuring heavily glycosylated proteins with MP. In the future we expect MP to become a routine analysis method for glycoprotein characterization. It will help to complement existing methods thanks to its combination of mass resolution and accuracy together with minute sample consumption, simple experimental procedures, broad buffer compatibility and ability to measure even complex glycoproteins, oligomers and their interactions.

In chapter 6 we dedicated our time and attention to rather unforeseen research. Following the worldwide COVID-19 health crisis we wanted to use

the new methods to contribute to the efforts of people around the globe to tackle this crisis. It was a huge motivator to work on a contribution to the society, beyond the aim of a classical paper publication. In this project we made a collaborative effort to help bringing new insight in the host cell entry mechanism of SARS-CoV-2. SARS-CoV-2 initiates infection via binding of the spike glycoprotein (S) to the host cell receptor Ace-2, followed by viral and host membrane fusion.

In this project we showed that receptor binding domain containing SARS-CoV-2 proteins (RBD, S1 and S protein), involved in the first steps of host cell invasion, have pM to nM binding affinity for their target receptor on the host cell (ACE2). From a biophysical point of view, this suggests that SARS-CoV-2 virus particles can bind with high affinity to the host cell membrane to initiate membrane fusion and host cell entry. Furthermore, these results support the hypothesis that recombinant ACE2 could help to neutralize viruses by blocking ACE2 binding sites on the viron before it can reach and infect the host cell. Any biological significance of these findings would first need further investigation in *in-vivo* experiments.

In more detail, MP experiments provided further insights on these protein-protein interactions. We were able to quantify a previously unknown K_{d} of ACE2 monomer-dimer equilibrium and showed that the ACE2-RBD interaction is much more complex than reported, involving 5 co-existing species. Additionally, this experiment revealed that ACE2-dimer can bind up to 2 RBDs, which suggests that ACE2 has the potential to induce cross-linking of SARS-CoV-2 S protein. Similar experiments with a S protein construct (Wrapp et al.[25]) revealed that ACE2 can indeed bind with high affinity to the S protein, but also supported previous findings, that the S protein construct used in our study is likely to have only 1 out of 3 RBDs in an accessible up-conformation. Overall,

binding affinities and stoichiometries of the interactions measured by MP with the single-shot K_d method and binding curve fits were in good agreement with recently published literature values obtained by SPR and BLI.

Investigating potential ACE2-induced cross-linking or aggregation of S protein remains the focus of future work on this project. It would be interesting to include different S protein constructs in this study and assess the observed deviation of relative peak intensities of ACE2 and S protein in a more quantitative manner. This could help to make more quantitative comments on potential aggregation. Revealing aggregation could have significant impact on the wider Covid-19 research. Specifically, it could be a starting point for the development of therapies which focus on the clearance or neutralization of virus particles. In this process, MP results will provide detailed insights into binding affinities and stoichiometries. Similarly, MP could be used to guide drug development for a variety of agents (e.g. small molecules, antibodies or peptides) to arrest host cell receptor binding and membrane fusion.[279]

Having been involved in these exciting protein-protein interaction projects presented in this thesis showed first of all that mass photometry almost every time provided new, previously inaccessible insights in simple experiments. It also showed that there are still various areas for improvement, which ensures that future PhD projects will continue to be exciting. Many aspects thereof we discussed in Chapter 3. Other areas for improvement include the limited lower molecular weight range (>40 kDa) and molecular weight resolution (FWHM ca. 5-10 % of MW). Higher laser intensities and further noise reduction are a potential avenue to lower the mass detection limit. An alternative would be the introduction of tags to artificially increase the molecular weight. Together with a more stable reference field and improved image analysis this could also help to address challenges associated to mass resolution. With increased MW

resolution protein-small molecule interactions or samples with different species of similar molecular weights would be easier to access.

Following the (justified) scepticism contained in the #1 question asked in presentations ("Is your detection efficiency the same for all proteins?") it seems reasonable to continue investing time in this topic. So far, we observed statistically significant differences in detection efficiency for proteins with large differences in molecular weight and recommend a diffusion correction ($D_{12} \propto MW^{-1/3}$), especially in continuous-flow experiments. Moreover, we expect that extreme charge states might also influence detection efficiency, but could not find any evidence so far[4], except for highly negatively charged molecules such as DNA. DNA molecules are likely to be repelled by the negatively charged coverslip glass surface and show significantly reduced number of counts in MP experiments with unfunctionalized glass surfaces.[165] Fortunately, anomalies become directly evident during MP experiments, when the detected number of counts is lower than the expected number of counts deduced from UV-VIS concentrations measurements and can be directly investigated.

As outlined above, microfluidic devices could help to extend the application range of MP to interactions with fast kinetics and low binding affinities. Advantages beyond this include enhanced time resolution because the time delay between mixing and detection could be widely and precisely varied allowing for highly resolved kinetic decay or association curves. Moreover, a robust, chip-based injection system would reduce sample consumption, increase reproducibility as well as automation, overall making it more user-friendly.

The short measurement times (< 30 s), low sample consumption and simplicity of the experiments, including automated data analysis, present an ideal basis for the implementation of high throughput. This would extend MP's application as biophysical characterization tool to a screening tool for

compound search in drug development as well as broadly applicable quality control method.

Overall, the herein presented strengths of MP show why the rapid adoption of mass photometry in laboratories worldwide is set to continue. Pushing the boundary of current limitations offers new exciting opportunities to further increase the applicability of mass photometry in biological research, drug development and beyond.

References

[1] Hartley, H. Origin of the word 'protein'. *Nature* **168**, 244–244 (1951).

[2] Berggård, T., Linse, S. & James, P. Methods for the detection and analysis of protein–protein interactions. *PROTEOMICS* **7**, 2833–2842 (2007).

[3] Cole, D., Young, G., Weigel, A., Sebesta, A. & Kukura, P. Label-free single-molecule imaging with numerical-aperture-shaped interferometric scattering microscopy. *ACS photonics* **4**, 211–216 (2017).

[4] Young, G. *et al.* Quantitative mass imaging of single biological macromolecules. *Science (New York, N.Y.)* **360**, 423–427 (2018).

[5] Phizicky, E. M. & Fields, S. Protein-protein interactions: methods for detection and analysis. *Microbiological reviews* **59**, 94–123 (1995).

[6] Fu, H. *Protein-Protein Interactions: Methods and Applications*. Methods In Molecular Biology (Humana Press, 2015), 2 edn.

[7] Hopper, J. T. S. & Robinson, C. V. Mass spectrometry quantifies protein interactions—from molecular chaperones to membrane porins. *Angewandte Chemie International Edition* **53**, 14002–14015 (2014).

[8] Pierce, M. M., Raman, C. S. & Nall, B. T. Isothermal titration calorimetry of protein–protein interactions. *Methods* **19**, 213–221 (1999).

[9] Malmqvist, M. Surface plasmon resonance for detection and measurement of antibody-antigen affinity and kinetics. *Current Opinion in Immunology* **5**, 282–286 (1993).

[10] O'Shannessy, D. J. Determination of kinetic rate and equilibrium binding constants for macromolecular interactions: a critique of the surface plasmon resonance literature. *Current Opinion in Biotechnology* **5**, 65–71 (1994).

[11] Helmerhorst, E., Chandler, D. J., Nussio, M. & Mamotte, C. D. Real-time and label-free bio-sensing of molecular interactions by surface plasmon resonance: A laboratory medicine perspective. *The Clinical Biochemist Reviews* **33**, 161–173 (2012).

[12] Homola, J. Surface plasmon resonance sensors for detection of chemical and biological species. *Chemical Reviews* **108**, 462–493 (2008).

[13] Zhou, M., Li, Q. & Wang, R. Current experimental methods for characterizing protein-protein interactions. *ChemMedChem* **11**, 738–756 (2016).

[14] Du, X. *et al.* Insights into protein-ligand interactions: Mechanisms, models, and methods. *International journal of molecular sciences* **17**, 144 (2016).

[15] Zanchetta, G., Lanfranco, R., Giavazzi, F., Bellini, T. & Buscaglia, M. Emerging applications of label-free optical biosensors. *Nanophotonics* **6**, 627 (2017).

[16] Singh, P. Spr biosensors: Historical perspectives and current challenges. *Sensors and Actuators B: Chemical* **229**, 110–130 (2016).

[17] Bocková, M., Slabý, J., Špringer, T. & Homola, J. Advances in surface plasmon resonance imaging and microscopy and their biological applications. *Annual Review of Analytical Chemistry* **12**, 151–176 (2019).

[18] Wang, D. *et al.* Recent advances in surface plasmon resonance imaging sensors. *Sensors* **19**, 1266 (2019).

[19] Liu, C., Hu, F., Yang, W., Xu, J. & Chen, Y. A critical review of advances in surface plasmon resonance imaging sensitivity. *TrAC Trends in Analytical Chemistry* **97**, 354–362 (2017).

[20] Zeng, Y. *et al.* Recent advances in surface plasmon resonance imaging: detection speed, sensitivity, and portability. *Nanophotonics* **6**, 1017 (2017).

[21] Kamat, V., Rafique, A., Huang, T., Olsen, O. & Olson, W. The impact of different human igg capture molecules on the kinetics analysis of antibody-antigen interaction. *Analytical Biochemistry* **593**, 113580 (2020).

[22] Yang, H. M. *et al.* Label-free analysis of multivalent protein binding using bioresponsive nanogels and surface plasmon resonance (spr). *Acs Applied Materials and Interfaces* **12**, 5413–5419 (2020).

[23] Errington, W. J., Bruncsics, B. & Sarkar, C. A. Mechanisms of noncanonical binding dynamics in multivalent protein–protein interactions. *Proceedings of the National Academy of Sciences* **116**, 25659–25667 (2019).

[24] Mamer, S. B. *et al.* The convergence of cell-based surface plasmon resonance and biomaterials: The future of quantifying bio-molecular interactions—a review. *Annals of Biomedical Engineering* **48**, 2078–2089 (2020).

[25] Wrapp, D. *et al.* Cryo-em structure of the 2019-ncov spike in the prefusion conformation. *Science* **367**, 1260–1263 (2020).

[26] Ridley, C. *et al.* The c-terminal dimerization domain of the respiratory mucin muc5b functions in mucin stability and intracellular packaging before secretion. *Journal of Biological Chemistry* **294**, 17105–17116 (2019).

[27] Huang, R. Y. C. *et al.* Integrated approach for characterizing bispecific antibody/antigens complexes and mapping binding epitopes with sec/mals, native mass spectrometry, and protein footprinting. *Analytical Chemistry* **92**, 10709–10716 (2020).

[28] Petersen, R. L. Strategies using bio-layer interferometry biosensor technology for vaccine research and development. *Biosensors* **7**, 49 (2017).

[29] Kumaraswamy, S. & Tobias, R. *Label-Free Kinetic Analysis of an Antibody–Antigen Interaction Using Biolayer Interferometry*, 165–182 (Springer New York, New York, NY, 2015).

[30] Weeramange, C. J., Fairlamb, M. S., Singh, D., Fenton, A. W. & Swint-Kruse, L. The strengths and limitations of using biolayer interferometry to monitor equilibrium titrations of biomolecules. *Protein Science* **29**, 1018–1034 (2020).

[31] Sultana, A. & Lee, J. E. Measuring protein-protein and protein-nucleic acid interactions by biolayer interferometry. *Current Protocols in Protein Science* **79**, 19.25.1–19.25.26 (2015).

[32] Yang, D., Singh, A., Wu, H. & Kroe-Barrett, R. Comparison of biosensor platforms in the evaluation of high affinity antibody-antigen binding kinetics. *Analytical Biochemistry* **508**, 78–96 (2016).

[33] Abdiche, Y., Malashock, D., Pinkerton, A. & Pons, J. Determining kinetics and affinities of protein interactions using a parallel real-time label-free biosensor, the octet. *Analytical Biochemistry* **377**, 209–217 (2008).

[34] Kamat, V. & Rafique, A. Designing binding kinetic assay on the bio-layer interferometry (bli) biosensor to characterize antibody-antigen interactions. *Analytical Biochemistry* **536**, 16–31 (2017).

[35] Wallner, J., Kühleitner, M., Brunner, N., Lhota, G. & Vorauer-Uhl, K. Application of the log-normal model for long term high affinity antibody/antigen interactions using bio-layer interferometry. *Journal of Mathematical Chemistry* **52**, 575–587 (2014).

[36] Forssén, P., Samuelsson, J., Lacki, K. & Fornstedt, T. Advanced analysis of biosensor data for sars-cov-2 rbd and ace2 interactions. *Analytical Chemistry* 11520–11524 (2020).

[37] Yi, C. *et al.* Key residues of the receptor binding motif in the spike protein of sars-cov-2 that interact with ace2 and neutralizing antibodies. *Cellular and Molecular Immunology* **17**, 621–630 (2020).

[38] Walls, A. C. *et al.* Unexpected receptor functional mimicry elucidates activation of coronavirus fusion. *Cell* **176**, 1026–1039.e15 (2019).

[39] Zhou, H. *et al.* Structural definition of a neutralization epitope on the n-terminal domain of mers-cov spike glycoprotein. *Nature Communications* **10**, 3068 (2019).

[40] Yuan, M. *et al.* A highly conserved cryptic epitope in the receptor binding domains of sars-cov-2 and sars-cov. *Science* **368**, 630–633 (2020).

[41] Walls, A. C. *et al.* Structure, function, and antigenicity of the sars-cov-2 spike glycoprotein. *Cell* **181**, 281–292.e6 (2020).

[42] Tian, X. *et al.* Potent binding of 2019 novel coronavirus spike protein by a sars coronavirus-specific human monoclonal antibody. *Emerging Microbes and Infections* **9**, 382–385 (2020).

[43] Widjaja, I. *et al.* Towards a solution to mers: protective human monoclonal antibodies targeting different domains and functions of the mers-coronavirus spike glycoprotein. *Emerging Microbes and Infections* **8**, 516–530 (2019).

[44] Wang, C. *et al.* A human monoclonal antibody blocking sars-cov-2 infection. *Nature Communications* **11**, 2251 (2020).

[45] Dang, H. V. *et al.* An antibody against the f glycoprotein inhibits nipah and hendra virus infections. *Nature Structural and Molecular Biology* **26**, 980–987 (2019).

[46] Li, X. *et al.* Integration of high-throughput analytics and cell imaging enables direct early productivity and product quality assessment during chinese hamster ovary cell line development for a complex multi-subunit vaccine antigen. *Biotechnology Progress* **36**, e2914 (2020).

[47] Wallner, J. *et al.* Lectin bio-layer interferometry for assessing product quality of fc- glycosylated immunoglobulin g. *Biotechnology Progress* **35**, e2864 (2019).

[48] Loomis, R. J. *et al.* Structure-based design of nipah virus vaccines: A generalizable approach to paramyxovirus immunogen development. *Frontiers in Immunology* **11**, 842 (2020).

[49] Rant, U. *et al.* Detection and size analysis of proteins with switchable dna layers. *Nano Letters* **9**, 1290–1295 (2009).

[50] Rant, U. Sensing with electro-switchable biosurfaces. *Bioanalytical Reviews* **4**, 97–114 (2012).

[51] Langer, A. *et al.* Protein analysis by time-resolved measurements with an electro-switchable dna chip. *Nature Communications* **4**, 2099 (2013).

[52] Knezevic, J. *et al.* Quantitation of affinity, avidity, and binding kinetics of protein analytes with a dynamically switchable biosurface. *Journal of the American Chemical Society* **134**, 15225–15228 (2012).

[53] Schiedel, M., Daub, H., Itzen, A. & Jung, M. Validation of the slow off-kinetics of sirtuin-rearranging ligands (sirreals) by means of label-free electrically switchable nanolever technology. *ChemBioChem* **21**, 1161–1166 (2020).

[54] Franz-Oberdorf, K. *et al.* Physical interaction between the strawberry allergen fra a 1 and an associated partner faap: Interaction of fra a 1 proteins and faap. *Proteins: Structure, Function, and Bioinformatics* **85**, 1891–1901 (2017).

[55] Crowe, J. S. *et al.* Preclinical development of a novel, orally-administered anti-tumour necrosis factor domain antibody for the treatment of inflammatory bowel disease. *Scientific Reports* **8**, 4941 (2018).

[56] Daub, H. *et al.* The trimer to monomer transition of tumor necrosis factor-alpha is a dynamic process that is significantly altered by therapeutic antibodies. *Scientific Reports* **10**, 9265 (2020).

[57] Ouimet, C. M., D'amico, C. I. & Kennedy, R. T. Advances in capillary electrophoresis and the implications for drug discovery. *Expert Opinion on Drug Discovery* **12**, 213–224 (2017).

[58] Moser, A. C., Trenhaile, S. & Frankenberg, K. Studies of antibody-antigen interactions by capillary electrophoresis: A review. *Methods* **146**, 66–75 (2018).

[59] Domínguez-Vega, E. *et al.* Development of a surface plasmon resonance sensor for coupling to capillary electrophoresis allowing affinity assessment of protein mixture components. *Sensors and Actuators B: Chemical* **254**, 1040–1047 (2018).

[60] Heegaard, N. H. H., Nilsson, S. & Guzman, N. A. Affinity capillary electrophoresis: important application areas and some recent developments. *Journal of Chromatography B: Biomedical Sciences and Applications* **715**, 29–54 (1998).

[61] Rauch, J. N., Nie, J., Buchholz, T. J., Gestwicki, J. E. & Kennedy, R. T. Development of a capillary electrophoresis platform for identifying inhibitors of protein–protein interactions. *Analytical Chemistry* **85**, 9824–9831 (2013).

[62] Pedersen, J. T., Østergaard, J., Houen, G. & Heegaard, N. H. H. Affinity capillary electrophoresis for identification and investigation of human gc-globulin (vitamin d-binding protein) and its isoforms interacting with g-actin. *ELECTROPHORESIS* **29**, 1723–1733 (2008).

[63] Shimura, K. *et al.* Analysis of protein–protein interactions with a multi-capillary electrophoresis instrument. *ELECTROPHORESIS* **27**, 1886–1894 (2006).

[64] Lassen, K. S., Bradbury, A. R. M., Rehfeld, J. F. & Heegaard, N. H. H. Microscale characterization of the binding specificity and affinity of a monoclonal antisulfotyrosyl igg antibody. *ELECTROPHORESIS* **29**, 2557–2564 (2008).

[65] Yu, F., Zhao, Q., Zhang, D., Yuan, Z. & Wang, H. Affinity interactions by capillary electrophoresis: Binding, separation, and detection. *Analytical Chemistry* **91**, 372–387 (2019).

[66] Vergnon, A. L. & Chu, Y.-H. Electrophoretic methods for studying protein–protein interactions. *Methods* **19**, 270–277 (1999).

[67] Ouimet, C. M. *et al.* Protein cross-linking capillary electrophoresis for protein–protein interaction analysis. *Analytical Chemistry* **88**, 8272–8278 (2016).

[68] Ouimet, C. M. *et al.* Protein cross-linking capillary electrophoresis at increased throughput for a range of protein–protein interactions. *Analyst* **143**, 1805–1812 (2018).

[69] Chen, X. & Flynn, G. C. A high throughput dimer screening assay for monoclonal antibodies using chemical cross-linking and microchip electrophoresis. *Journal of Chromatography B* **877**, 3012–3018 (2009).

[70] Ouimet, C. M., D'Amico, C. I. & Kennedy, R. T. Droplet sample introduction to microchip gel and zone electrophoresis for rapid analysis of protein-protein complexes and enzymatic reactions. *Analytical and Bioanalytical Chemistry* **411**, 6155–6163 (2019).

[71] Arter, W. E., Levin, A., Krainer, G. & Knowles, T. P. J. Microfluidic approaches for the analysis of protein-protein interactions in solution. *Biophysical reviews* **12**, 575–585 (2020).

[72] Zhang, C. *et al.* Clinical and pharmaceutical applications of affinity ligands in capillary electrophoresis: A review. *Journal of Pharmaceutical and Biomedical Analysis* **177**, 112882 (2020).

[73] Farcaş, E., Pochet, L., Crommen, J., Servais, A.-C. & Fillet, M. Capillary electrophoresis in the context of drug discovery. *Journal of Pharmaceutical and Biomedical Analysis* **144**, 195–212 (2017).

[74] Lebowitz, J., Lewis, M. S. & Schuck, P. Modern analytical ultracentrifugation in protein science: a tutorial review. *Protein science : a publication of the Protein Society* **11**, 2067–2079 (2002).

[75] Berkowitz, S. A., Engen, J. R., Mazzeo, J. R. & Jones, G. B. Analytical tools for characterizing biopharmaceuticals and the implications for biosimilars. *Nature Reviews Drug Discovery* **11**, 527–540 (2012).

[76] Liu, J., Andya, J. D. & Shire, S. J. A critical review of analytical ultracentrifugation and field flow fractionation methods for measuring protein aggregation. *The AAPS journal* **8**, E580–E589 (2006).

[77] Stafford, W. F. *Protein–Protein and Ligand–Protein Interactions Studied by Analytical Ultracentrifugation*, 83–113 (Humana Press, Totowa, NJ, 2009).

[78] Schuck, P. Analytical ultracentrifugation as a tool for studying protein interactions. *Biophysical reviews* **5**, 159–171 (2013).

[79] Schuck, A. B. & Peter. *Analytical Ultracentrifugation in the Study of Protein Self-association and Heterogeneous Protein-Protein Interactions*, book section 253 (Cold Spring Harbor Laboratory Press., 2005), second edn.

[80] Zhao, H., Mayer, M. L. & Schuck, P. Analysis of protein interactions with picomolar binding affinity by fluorescence-detected sedimentation velocity. *Analytical Chemistry* **86**, 3181–3187 (2014).

[81] Zhao, H., Lomash, S., Glasser, C., Mayer, M. L. & Schuck, P. Analysis of high affinity self-association by fluorescence optical sedimentation velocity analytical ultracentrifugation of labeled proteins: Opportunities and limitations. *PLOS ONE* **8**, e83439 (2013).

[82] Chaturvedi, S. K., Ma, J., Zhao, H. & Schuck, P. Use of fluorescence-detected sedimentation velocity to study high-affinity protein interactions. *Nature Protocols* **12**, 1777–1791 (2017).

[83] Harding, S. & Rowe, A. Insight into protein–protein interactions from analytical ultracentrifugation. *Biochemical Society Transactions* **38**, 901–907 (2010).

[84] Chaturvedi, S. K., Ma, J., Brown, P. H., Zhao, H. & Schuck, P. Measuring macromolecular size distributions and interactions at high concentrations by sedimentation velocity. *Nature Communications* **9**, 4415 (2018).

[85] Chaturvedi, S. K., Sagar, V., Zhao, H., Wistow, G. & Schuck, P. Measuring ultra-weak protein self-association by non-ideal sedimentation velocity. *Journal of the American Chemical Society* **141**, 2990–2996 (2019).

[86] Zhao, H. *et al.* Quantitative analysis of protein self-association by sedimentation velocity. *Current Protocols in Protein Science* **101**, e109 (2020).

[87] Zhao, H. *et al.* Preferential assembly of heteromeric kainate and ampa receptor amino terminal domains. *eLife* **6**, e32056 (2017).

[88] Sherekar, M. *et al.* Biochemical and structural analyses reveal that the tumor suppressor neurofibromin (nf1) forms a high-affinity dimer. *Journal of Biological Chemistry* **295**, 1105–1119 (2020).

[89] Some, D. Light-scattering-based analysis of biomolecular interactions. *Biophysical Reviews* **5**, 147–158 (2013).

[90] Sahin, E. & Roberts, C. J. *Size-Exclusion Chromatography with Multi-angle Light Scattering for Elucidating Protein Aggregation Mechanisms*, 403–423 (Humana Press, Totowa, NJ, 2012).

[91] Hong, P., Koza, S. & Bouvier, E. S. P. A review size-exclusion chromatography for the analysis of protein biotherapeutics and their aggregates. *Journal of Liquid Chromatography and Related Technologies* **35**, 2923–2950 (2012).

[92] De Benedetto, G., Cescutti, P., Giannelli, C., Rizzo, R. & Micoli, F. Multiple techniques for size determination of generalized modules for membrane antigens from salmonella typhimurium and salmonella enteritidis. *ACS Omega* **2**, 8282–8289 (2017).

[93] Boyd, D. *et al.* Isolation and characterization of a monoclonal antibody containing an extra heavy-light chain fab arm. *mAbs* **10**, 346–353 (2018).

[94] Stetefeld, J., McKenna, S. A. & Patel, T. R. Dynamic light scattering: a practical guide and applications in biomedical sciences. *Biophysical Reviews* **8**, 409–427 (2016).

[95] Minton, A. P. Recent applications of light scattering measurement in the biological and biopharmaceutical sciences. *Analytical Biochemistry* **501**, 4–22 (2016).

[96] Murphy, R. M. Static and dynamic light scattering of biological macromolecules: what can we learn? *Current Opinion in Biotechnology* **8**, 25–30 (1997).

[97] Wyatt, P. J. Light scattering and the absolute characterization of macromolecules. *Analytica Chimica Acta* **272**, 1–40 (1993).

[98] Zhou, T. *et al.* Structural definition of a conserved neutralization epitope on hiv-1 gp120. *Nature* **445**, 732–737 (2007).

[99] Lobner, E. *et al.* Fcab-her2 interaction: a ménage à trois. lessons from x-ray and solution studies. *Structure* **25**, 878–889.e5 (2017).

[100] Burman, M. & Schön, O. Transient protein self-association determined by sec-mals. *LC GC North America* **37**, 716 (2019).

[101] Das, S., Stivison, E., Folta-Stogniew, E. & Oliver, D. Reexamination of the role of the amino terminus of seca in promoting its dimerization and functional state. *Journal of Bacteriology* **190**, 7302–7307 (2008).

[102] Kapoor, N. *et al.* Nucleobindin 1 is a calcium-regulated guanine nucleotide dissociation inhibitor of g-alpha-i1. *Journal of Biological Chemistry* **285**, 31647–31660 (2010).

[103] Hastie, K. M. *et al.* Structural basis for antibody-mediated neutralization of lassa virus. *Science* **356**, 923–928 (2017).

[104] Zhao, L. *et al.* Paracrine-endocrine fgf chimeras as potent therapeutics for metabolic diseases. *EBioMedicine* **48**, 462–477 (2019).

[105] Sun, Z., Zheng, Y. & Liu, W. Identification and characterization of a novel calmodulin binding site in drosophila trp c-terminus. *Biochemical and Biophysical Research Communications* **501**, 434–439 (2018).

[106] Wagner, A. *et al.* Inhibitor-induced dimerization of an essential oxidoreductase from african trypanosomes. *Angewandte Chemie International Edition* **58**, 3640–3644 (2019).

[107] Sereikaite, V. *et al.* Targeting the gamma-aminobutyric acid type b (gabab) receptor complex: Development of inhibitors targeting the k+ channel tetramerization domain (kctd) containing proteins/gabab receptor protein–protein interaction. *Journal of Medicinal Chemistry* **62**, 8819–8830 (2019).

[108] Legewie, L. *et al.* Biochemical and structural characterization of murine gbp7, a guanylate binding protein with an elongated c-terminal tail. *Biochemical Journal* **476**, 3161–3182 (2019).

[109] Lobner, E. *et al.* Getting cd19 into shape: Expression of natively folded "difficult-to- express" cd19 for staining and stimulation of car-t cells. *Frontiers in Bioengineering and Biotechnology* **8**, 49 (2020).

[110] Hastie, K. M. *et al.* Convergent structures illuminate features for germline antibody binding and pan-lassa virus neutralization. *Cell* **178**, 1004–1015.e14 (2019).

[111] Hanlon, A. D., Larkin, M. I. & Reddick, R. M. Free-solution, label-free protein-protein interactions characterized by dynamic light scattering. *Biophysical Journal* **98**, 297–304 (2010).

[112] Corbett, D., Bye, J. W. & Curtis, R. A. *Measuring Nonspecific Protein–Protein Interactions by Dynamic Light Scattering*, 3–21 (Springer New York, New York, NY, 2019).

[113] Some, D. *Composition-Gradient Multiangle Light Scattering*, 336–343 (Springer Berlin Heidelberg, Berlin, Heidelberg, 2013).

[114] Hung, J. J. *et al.* Protein–protein interactions of highly concentrated monoclonal antibody solutions via static light scattering and influence on the viscosity. *The Journal of Physical Chemistry B* **123**, 739–755 (2019).

[115] Some, D., Pollastrini, J. & Cao, S. Characterizing reversible protein association at moderately high concentration via composition-gradient static light scattering. *Journal of Pharmaceutical Sciences* **105**, 2310–2318 (2016).

[116] Cui, Y., Cui, P., Chen, B., Li, S. & Guan, H. Monoclonal antibodies: formulations of marketed products and recent advances in novel delivery system. *Drug Development and Industrial Pharmacy* **43**, 519–530 (2017).

[117] Esfandiary, R., Parupudi, A., Casas-Finet, J., Gadre, D. & Sathish, H. Mechanism of reversible self-association of a monoclonal antibody: Role of electrostatic and hydrophobic interactions. *Journal of Pharmaceutical Sciences* **104**, 577–586 (2015).

[118] Arora, J. *et al.* Charge-mediated fab-fc interactions in an igg1 antibody induce reversible self-association, cluster formation, and elevated viscosity. *mAbs* **8**, 1561–1574 (2016).

[119] Pallesen, J. *et al.* Structures of ebola virus gp and sgp in complex with therapeutic antibodies. *Nature Microbiology* **1**, 16128 (2016).

[120] Jerabek-Willemsen, M. *et al.* Microscale thermophoresis: Interaction analysis and beyond. *Journal of Molecular Structure* **1077**, 101–113 (2014).

[121] Sparks, R. P. & Fratti, R. *Use of Microscale Thermophoresis (MST) to Measure Binding Affinities of Components of the Fusion Machinery*, 191–198 (Springer New York, New York, NY, 2019).

[122] Wienken, C. J., Baaske, P., Rothbauer, U., Braun, D. & Duhr, S. Protein-binding assays in biological liquids using microscale thermophoresis. *Nature Communications* **1**, 100 (2010).

[123] Scheuermann, T. H., Padrick, S. B., Gardner, K. H. & Brautigam, C. A. On the acquisition and analysis of microscale thermophoresis data. *Analytical Biochemistry* **496**, 79–93 (2016).

[124] Magnez, R. *et al.* Pd-1/pd-l1 binding studies using microscale thermophoresis. *Scientific Reports* **7**, 17623 (2017).

[125] Liberelle, M. *et al.* Muc4-erbb2 oncogenic complex: Binding studies using microscale thermophoresis. *Scientific Reports* **9**, 16678 (2019).

[126] Asmari, M., Ratih, R., Alhazmi, H. A. & El Deeb, S. Thermophoresis for characterizing biomolecular interaction. *Methods* **146**, 107–119 (2018).

[127] Cohen-Khait, R., Dym, O., Hamer-Rogotner, S. & Schreiber, G. Promiscuous protein binding as a function of protein stability. *Structure* **25**, 1867–1874.e3 (2017).

[128] Topf, A., Franz, P. & Tsiavaliaris, G. Microscale thermophoresis (mst) for studying actin polymerization kinetics. *BioTechniques* **63**, 187–190 (2017).

[129] Hörnschemeyer, P., Liss, V., Heermann, R., Jung, K. & Hunke, S. Interaction analysis of a two-component system using nanodiscs. *PLOS ONE* **11**, e0149187 (2016).

[130] Xie, D. *et al.* First anti-tocv activity evaluation of glucopyranoside derivatives containing a dithioacetal moiety through a novel tocvcp-

oriented screening method. *Journal of Agricultural and Food Chemistry* **67**, 7243–7248 (2019).

[131] Zhao, B. *et al.* Direct label-free methods for identification of target proteins in agrochemicals. *International Journal of Biological Macromolecules* **164**, 1475–1483 (2020).

[132] Liu, S. *et al.* Rapid and sensitive detection of prostate-specific antigen via label-free frequency shift raman of sensing graphene. *Biosensors and Bioelectronics* **158**, 112184 (2020).

[133] Adhav, A. S., Kokane, S. R. & Joshi, R. S. Functional characterization of helicoverpa armigera trehalase and investigation of physiological effects caused due to its inhibition by validamycin a formulation. *International Journal of Biological Macromolecules* **112**, 638–647 (2018).

[134] Alfieri, A. *et al.* The structural bases for agonist diversity in an arabidopsis thaliana glutamate receptor-like channel. *Proceedings of the National Academy of Sciences* **117**, 752–760 (2020).

[135] Bartoschik, T. *et al.* Near-native, site-specific and purification-free protein labeling for quantitative protein interaction analysis by microscale thermophoresis. *Scientific Reports* **8**, 4977 (2018).

[136] Huang, M. *et al.* Homogeneous, low-volume, efficient, and sensitive quantitation of circulating exosomal pd-l1 for cancer diagnosis and immunotherapy response prediction. *Angewandte Chemie International Edition* **59**, 4800–4805 (2020).

[137] Lampugnani, E. R., Wink, R. H., Persson, S. & Somssich, M. The toolbox to study protein–protein interactions in plants. *Critical Reviews in Plant Sciences* **37**, 308–334 (2018).

[138] Ma, L. *et al.* Real-time process quality control of ramulus cinnamomi by critical quality attribute using microscale thermophoresis and on-line nir. *Spectrochimica Acta Part A: Molecular and Biomolecular Spectroscopy* **224**, 117463 (2020).

[139] Mueller, A. M. *et al. MicroScale Thermophoresis: A Rapid and Precise Method to Quantify Protein–Nucleic Acid Interactions in Solution*, 151–164 (Springer New York, New York, NY, 2017).

[140] Rainard, J. M., Pandarakalam, G. C. & McElroy, S. P. Using microscale thermophoresis to characterize hits from high-throughput screening: A european lead factory perspective. *SLAS DISCOVERY: Advancing the Science of Drug Discovery* **23**, 225–241 (2018).

[141] Seidel, S. A. I. *et al.* Label-free microscale thermophoresis discriminates sites and affinity of protein–ligand binding. *Angewandte Chemie International Edition* **51**, 10656–10659 (2012).

[142] Seidel, S. A. I. *et al.* Microscale thermophoresis quantifies biomolecular interactions under previously challenging conditions. *Methods* **59**, 301–315 (2013).

[143] Grudnik, P. *et al.* Structural basis for adp-dependent glucokinase inhibition by 8-bromo–substituted adenosine nucleotide. *Journal of Biological Chemistry* **293**, 11088–11099 (2018).

[144] Kaan, H. Y. K., Sim, A. Y. L., Tan, S. K. J., Verma, C. & Song, H. Targeting yap/taz-tead protein-protein interactions using fragment-based and computational modeling approaches. *PLOS ONE* **12**, e0178381 (2017).

[145] Arosio, P. *et al.* Microfluidic diffusion analysis of the sizes and interactions of proteins under native solution conditions. *ACS Nano* **10**, 333–341 (2016).

[146] Zhang, Y. *et al.* A microfluidic strategy for the detection of membrane protein interactions. *Lab on a Chip* **20**, 3230–3238 (2020).

[147] Zhang, Y. *et al.* Protein aggregate-ligand binding assays based on microfluidic diffusional separation. *ChemBioChem* **17**, 1920–1924 (2016).

[148] Wright, M. A. *et al.* Cooperative assembly of hsp70 subdomain clusters. *Biochemistry* **57**, 3641–3649 (2018).

[149] Macikova, L. *et al.* Putative interaction site for membrane phospholipids controls activation of trpa1 channel at physiological membrane potentials. *The FEBS Journal* **286**, 3664–3683 (2019).

[150] Gang, H. *et al.* Microfluidic diffusion platform for characterizing the sizes of lipid vesicles and the thermodynamics of protein–lipid interactions. *Analytical Chemistry* **90**, 3284–3290 (2018).

[151] Scheidt, T. *et al.* Secondary nucleation and elongation occur at different sites on alzheimer's amyloid-beta aggregates. *Science Advances* **5**, eaau3112 (2019).

[152] Challa, P. K. *et al.* Real-time intrinsic fluorescence visualization and sizing of proteins and protein complexes in microfluidic devices. *Analytical Chemistry* **90**, 3849–3855 (2018).

[153] Yates, E. V. *et al.* Latent analysis of unmodified biomolecules and their complexes in solution with attomole detection sensitivity. *Nature Chemistry* **7**, 802–809 (2015).

[154] Liebel, M., Hugall, J. T. & van Hulst, N. F. Ultrasensitive label-free nanosensing and high-speed tracking of single proteins. *Nano Letters* **17**, 1277–1281 (2017).

[155] Soltermann, F. *et al.* Quantifying protein–protein interactions by molecular counting with mass photometry. *Angewandte Chemie International Edition* **59**, 10774–10779 (2020).

[156] Wu, D. & Piszczek, G. Measuring the affinity of protein-protein interactions on a single-molecule level by mass photometry. *Analytical Biochemistry* **592**, 113575 (2020).

[157] Häußermann, K., Young, G., Kukura, P. & Dietz, H. Dissecting foxp2 oligomerization and dna binding. *Angewandte Chemie (International ed. in English)* **58**, 7662–7667 (2019).

[158] Fineberg, A., Surrey, T. & Kukura, P. Quantifying the monomer-dimer equilibrium of tubulin with mass photometry. *bioRxiv* 2020.07.16.199083 (2020).

[159] Torres-Ocampo, A. P. *et al.* Characterization of camkii-alpha holoenzyme stability. *Protein Science* **29**, 1524–1534 (2020).

[160] Tamara, S., Franc, V. & Heck, A. J. R. A wealth of genotype-specific proteoforms fine-tunes hemoglobin scavenging by haptoglobin. *Proceedings of the National Academy of Sciences* **117**, 15554–15564 (2020).

[161] Hickman, A. B., Kailasan, S., Genzor, P., Haase, A. D. & Dyda, F. Casposase structure and the mechanistic link between dna transposition and spacer acquisition by crispr-cas. *eLife* **9**, e50004 (2020).

[162] Sonn-Segev, A. *et al.* Quantifying the heterogeneity of macromolecular machines by mass photometry. *Nature Communications* **11**, 1772 (2020).

[163] Satapathy, S., Dabbs, R. A. & Wilson, M. R. Rapid high-yield expression and purification of fully post-translationally modified recombinant clusterin and mutants. *Scientific Reports* **10**, 14243 (2020).

[164] Lonhienne, T. *et al.* Structures of fungal and plant acetohydroxyacid synthases. *Nature* 317–321 (2020).

[165] Li, Y., Struwe, W. B. & Kukura, P. Single molecule mass photometry of nucleic acids. *Nucleic Acids Research* **48**, e97–e97 (2020).

[166] Olerinyova, A. *et al.* Mass photometry of membrane proteins. *bioRxiv* 2020.02.28.969287 (2020).

[167] Lebedeva, M. A., Palmieri, E., Kukura, P. & Fletcher, S. P. Emergence and rearrangement of dynamic supramolecular aggregates visualized by interferometric scattering microscopy. *ACS Nano* 11160–11168 (2020).

[168] Fineberg, A. *Interferometric scattering microscopy: from bacterial dynamics to molecular assembly.* Thesis, University of Oxford (2019).

[169] Young, G. *Mass Photometry: Weighing Single Molecules with Interferometric Scattering Microscopy.* Thesis, University of Oxford (2019).

[170] Piliarik, M. & Sandoghdar, V. Direct optical sensing of single unlabelled proteins and super-resolution imaging of their binding sites. *Nature Communications* **5**, 4495 (2014).

[171] AMOS, L. A. & AMOS, W. B. The bending of sliding microtubules imaged by confocal light microscopy and negative stain electron microscopy. *Journal of Cell Science* **1991**, 95–101 (1991).

[172] Lindfors, K., Kalkbrenner, T., Stoller, P. & Sandoghdar, V. Detection and spectroscopy of gold nanoparticles using supercontinuum white light confocal microscopy. *Physical Review Letters* **93**, 037401 (2004).

[173] Young, G. & Kukura, P. Interferometric scattering microscopy. *Annual Review of Physical Chemistry* **70**, 301–322 (2019).

[174] Weigel, A., Sebesta, A. & Kukura, P. Dark field microspectroscopy with single molecule fluorescence sensitivity. *ACS Photonics* **1**, 848–856 (2014).

[175] Hu, M. *et al.* Dark-field microscopy studies of single metal nanoparticles: understanding the factors that influence the linewidth of the localized surface plasmon resonance. *Journal of Materials Chemistry* **18**, 1949–1960 (2008).

[176] Kukura, P. *et al.* High-speed nanoscopic tracking of the position and orientation of a single virus. *Nature Methods* **6**, 923–927 (2009).

[177] Jacobsen, V., Stoller, P., Brunner, C., Vogel, V. & Sandoghdar, V. Interferometric optical detection and tracking of very small gold nanoparticles at a water-glass interface. *Optics Express* **14**, 405–414 (2006).

[178] Ortega Arroyo, J. *et al.* Label-free, all-optical detection, imaging, and tracking of a single protein. *Nano Letters* **14**, 2065–2070 (2014).

[179] Kensal Edward Van Holde, P. S. H., Curits Johnson. *Principles of Physical Biochemistry* (Pearson Prentice Hall, 1998), second edn.

[180] Nick Pace, C., Scholtz, J. M. & Grimsley, G. R. Forces stabilizing proteins. *FEBS Letters* **588**, 2177–2184 (2014).

[181] Sheu, S.-Y., Yang, D.-Y., Selzle, H. L. & Schlag, E. W. Energetics of hydrogen bonds in peptides. *Proceedings of the National Academy of Sciences* **100**, 12683–12687 (2003).

[182] Kamerlin, S. C. L. & Warshel, A. On the energetics of atp hydrolysis in solution. *The Journal of Physical Chemistry B* **113**, 15692–15698 (2009).

[183] Kastritis, P. L. & Bonvin, A. M. J. J. On the binding affinity of macromolecular interactions: daring to ask why proteins interact. *Journal of The Royal Society Interface* **10**, 20120835 (2013).

[184] Siebenmorgen, T. & Zacharias, M. Computational prediction of protein–protein binding affinities. *WIREs Computational Molecular Science* **10**, e1448 (2020).

[185] Pan, A. C., Borhani, D. W., Dror, R. O. & Shaw, D. E. Molecular determinants of drug–receptor binding kinetics. *Drug Discovery Today* **18**, 667–673 (2013).

[186] Schreiber, G., Haran, G. & Zhou, H. X. Fundamental aspects of protein-protein association kinetics. *Chemical reviews* **109**, 839–860 (2009).

[187] Schreiber, G. *Protein–Protein Interactions: Kinetics*, 2098–2101 (Springer Berlin Heidelberg, Berlin, Heidelberg, 2013).

[188] Calarese, D. A. *et al.* Antibody domain exchange is an immunological solution to carbohydrate cluster recognition. *Science* **300**, 2065–2071 (2003).

[189] Lee, H., Lee, S. & Heo, Y.-S. Molecular interactions of antibody drugs targeting pd-1, pd-l1, and ctla-4 in immuno-oncology. *Molecules* **24**, 1190–1190 (2019).

[190] Peng, H.-P., Lee, K. H., Jian, J.-W. & Yang, A.-S. Origins of specificity and affinity in antibody-protein interactions. *Proceedings of the National Academy of Sciences of the United States of America* **111**, E2656–E2665 (2014).

[191] Petry, S. Mechanisms of mitotic spindle assembly. *Annual review of biochemistry* **85**, 659–683 (2016).

[192] Heald, R. *et al.* Self-organization of microtubules into bipolar spindles around artificial chromosomes in xenopus egg extracts. *Nature* **382**, 420–425 (1996).

[193] Michaels, T. C. *et al.* Chemical kinetics for bridging molecular mechanisms and macroscopic measurements of amyloid fibril formation. *Annual Review of Physical Chemistry* **69**, 273–298 (2018).

[194] Ozorowski, G. *et al.* Open and closed structures reveal allostery and pliability in the hiv-1 envelope spike. *Nature* **547**, 360–363 (2017).

[195] Doitsh, G. & Greene, W. C. Dissecting how cd4-t cells are lost during hiv infection. *Cell Host and Microbe* **19**, 280–291 (2016).

[196] Stanton, R. A., Gernert, K. M., Nettles, J. H. & Aneja, R. Drugs that target dynamic microtubules: a new molecular perspective. *Medicinal research reviews* **31**, 443–481 (2011).

[197] Modell, A. E., Blosser, S. L. & Arora, P. S. Systematic targeting of protein-protein interactions. *Trends in pharmacological sciences* **37**, 702–713 (2016).

[198] Andrei, S. A. *et al.* Stabilization of protein-protein interactions in drug discovery. *Expert Opinion on Drug Discovery* **12**, 925–940 (2017).

[199] Enderlein, J., Gregor, I., Patra, D., Dertinger, T. & Kaupp, U. B. Performance of fluorescence correlation spectroscopy for measuring diffusion and concentration. *ChemPhysChem* **6**, 2324–2336 (2005).

[200] Goldschen-Ohm, M. P., White, D. S., Klenchin, V. A., Chanda, B. & Goldsmith, R. H. Observing single-molecule dynamics at millimolar concentrations. *Angewandte Chemie (International ed. in English)* **56**, 2399–2402 (2017).

[201] Aggarwal, V. & Ha, T. Single-molecule fluorescence microscopy of native macromolecular complexes. *Current Opinion in Structural Biology* **41**, 225–232 (2016).

[202] Schuck, P. & Zhao, H. The role of mass transport limitation and surface heterogeneity in the biophysical characterization of macromolecular binding processes by spr biosensing. *Methods in molecular biology (Clifton, N.J.)* **627**, 15–54 (2010).

[203] Sorret, L., DeWinter, M., Schwartz, D. & Randolph, T. Challenges in predicting protein-protein interactions from measurements of molecular diffusivity. *Biophysical Journal* **111**, 1831–1842 (2016).

[204] Vincent, K. J. & Zurini, M. Current strategies in antibody engineering: Fc engineering and ph-dependent antigen binding, bispecific antibodies and antibody drug conjugates. *Biotechnology Journal* **7**, 1444–1450 (2012).

[205] Goebel-Stengel, M., Stengel, A., Taché, Y. & Reeve, J. R. The importance of using the optimal plasticware and glassware in studies involving peptides. *Analytical Biochemistry* **414**, 38–46 (2011).

[206] Heyes, C. D., Groll, J., Möller, M. & Nienhaus, G. U. Synthesis, patterning and applications of star-shaped poly(ethylene glycol) biofunctionalized surfaces. *Molecular BioSystems* **3**, 419–430 (2007).

[207] Hua, B. *et al.* An improved surface passivation method for single-molecule studies. *Nature Methods* **11**, 1233 (2014).

[208] Hayes, J. M. *et al. Glycosylation and Fc Receptors*, 165–199 (Springer International Publishing, Cham, 2014).

[209] Praetor, A., Jones, R. M., Wong, W. L. & Hunziker, W. Membrane-anchored human fcrn can oligomerize in the absence of igg. *Journal of Molecular Biology* **321**, 277–284 (2002).

[210] Abdiche, Y. N. *et al.* The neonatal fc receptor (fcrn) binds independently to both sites of the igg homodimer with identical affinity. *mAbs* **7**, 331–343 (2015).

[211] Zijlstra, N. *et al.* Rapid microfluidic dilution for single-molecule spectroscopy of low-affinity biomolecular complexes. *Angewandte Chemie International Edition* **56**, 7126–7129 (2017).

[212] Watanabe, Y. *et al.* Signature of antibody domain exchange by native mass spectrometry and collision-induced unfolding. *Analytical Chemistry* **90**, 7325–7331 (2018).

[213] Wu, Y. *et al.* Structural basis for enhanced hiv-1 neutralization by a dimeric immunoglobulin g form of the glycan-recognizing antibody 2g12. *Cell Reports* **5**, 1443–1455 (2013).

[214] Nicholas, M. P., Rao, L. & Gennerich, A. Covalent immobilization of microtubules on glass surfaces for molecular motor force measurements

and other single-molecule assays. *Methods in molecular biology (Clifton, N.J.)* **1136**, 137–169 (2014).

[215] Marty, M. T. *et al.* Bayesian deconvolution of mass and ion mobility spectra: From binary interactions to polydisperse ensembles. *Analytical Chemistry* **87**, 4370–4376 (2015).

[216] World Health Organization. Hiv/aids data and statistics (2018).

[217] U.S. Department of Health and Human Services. Federal domestic hiv/aids programs and research spending (2019).

[218] Mascola, J. R. *et al.* Protection of macaques against vaginal transmission of a pathogenic hiv-1/siv chimeric virus by passive infusion of neutralizing antibodies. *AIDS* **15**, S18–S19 (2001).

[219] Trkola, A. Conformation of the native hiv-1 envelope protein raises questions for vaccine design. *Nature* **568**, 321–322 (2019).

[220] Sanders, R. W. & Moore, J. P. Native-like env trimers as a platform for hiv-1 vaccine design. *Immunological Reviews* **275**, 161–182 (2017).

[221] Lu, M. *et al.* Associating hiv-1 envelope glycoprotein structures with states on the virus observed by smfret. *Nature* **568**, 415–419 (2019).

[222] Wang, Q., Finzi, A. & Sodroski, J. The conformational states of the hiv-1 envelope glycoproteins. *Trends in Microbiology* **28**, 655–667 (2020).

[223] Sanders, R. W. *et al.* A next-generation cleaved, soluble hiv-1 env trimer, bg505 sosip.664 gp140, expresses multiple epitopes for broadly neutralizing but not non-neutralizing antibodies. *PLoS pathogens* **9**, e1003618–e1003618 (2013).

[224] Shingai, M. *et al.* Antibody-mediated immunotherapy of macaques chronically infected with shiv suppresses viraemia. *Nature* **503**, 277–280 (2013).

[225] Kaplon, H., Muralidharan, M., Schneider, Z. & Reichert, J. M. Antibodies to watch in 2020. *mAbs* **12**, 1703531 (2020).

[226] West, A. P. *et al.* Design and expression of a dimeric form of human immunodeficiency virus type 1 antibody 2g12 with increased neutralization potency. *Journal of Virology* **83**, 98–104 (2009).

[227] Julien, J.-P. *et al.* Asymmetric recognition of the hiv-1 trimer by broadly neutralizing antibody pg9. *Proceedings of the National Academy of Sciences* **110**, 4351–4356 (2013).

[228] Rathore, U. *et al.* Glycosylation of the core of the hiv-1 envelope subunit protein gp120 is not required for native trimer formation or viral infectivity. *Journal of Biological Chemistry* **292**, 10197–10219 (2017).

[229] Hoorelbeke, B. *et al.* Hiv-1 envelope trimer has similar binding characteristics for carbohydrate-binding agents as monomeric gp120. *FEBS Letters* **587**, 860–866 (2013).

[230] Kovacs, J. M. *et al.* Stable, uncleaved hiv-1 envelope glycoprotein gp140 forms a tightly folded trimer with a native-like structure. *Proceedings of the National Academy of Sciences* **111**, 18542–18547 (2014).

[231] Hoffenberg, S. *et al.* Identification of an hiv-1 clade a envelope that exhibits broad antigenicity and neutralization sensitivity and elicits antibodies targeting three distinct epitopes. *Journal of Virology* **87**, 5372–5383 (2013).

[232] Blattner, C. *et al.* Structural delineation of a quaternary, cleavage-dependent epitope at the gp41-gp120 interface on intact hiv-1 env trimers. *Immunity* **40**, 669–680 (2014).

[233] Gift, S. K. *et al.* Conformational and structural features of hiv-1 gp120 underlying the dual receptor antagonism by cross-reactive neutralizing antibody m18. *Biochemistry* **50**, 2756–2768 (2011).

[234] Ma, B.-J. *et al.* Envelope deglycosylation enhances antigenicity of hiv-1 gp41 epitopes for both broad neutralizing antibodies and their unmutated ancestor antibodies. *PLOS Pathogens* **7**, e1002200 (2011).

[235] Bricault, C. A. *et al.* Hiv-1 neutralizing antibody signatures and application to epitope-targeted vaccine design. *Cell Host and Microbe* **25**, 59–72.e8 (2019).

[236] Yasmeen, A. *et al.* Differential binding of neutralizing and non-neutralizing antibodies to native-like soluble hiv-1 env trimers, uncleaved env proteins, and monomeric subunits. *Retrovirology* **11**, 41 (2014).

[237] Pugach, P. *et al.* A native-like sosip.664 trimer based on an hiv-1 subtype b env gene. *Journal of Virology* **89**, 3380–3395 (2015).

[238] Lyumkis, D. *et al.* Cryo-em structure of a fully glycosylated soluble cleaved hiv-1 envelope trimer. *Science* **342**, 1484–1490 (2013).

[239] Lee, J. H. *et al.* A broadly neutralizing antibody targets the dynamic hiv envelope trimer apex via a long, rigidified, and anionic β-hairpin structure. *Immunity* **46**, 690–702 (2017).

[240] McCoy, L. E. & Burton, D. R. Identification and specificity of broadly neutralizing antibodies against hiv. *Immunological Reviews* **275**, 11–20 (2017).

[241] Chames, P. & Baty, D. Bispecific antibodies for cancer therapy. *mAbs* **1**, 539–547 (2009).

[242] Struwe, W. B., Stuckmann, A., Behrens, A.-J., Pagel, K. & Crispin, M. Global n-glycan site occupancy of hiv-1 gp120 by metabolic engineering and high-resolution intact mass spectrometry. *ACS chemical biology* **12**, 357–361 (2017).

[243] Struwe, W. B. *et al.* Site-specific glycosylation of virion-derived hiv-1 env is mimicked by a soluble trimeric immunogen. *Cell Reports* **24**, 1958–1966.e5 (2018).

[244] Varki, A. & Kornfeld, S. *Historical Background and Overview*, 1–18 (Cold Spring Harbor Laboratory Press Copyright 2015-2017 by The Consortium of Glycobiology Editors, La Jolla, California. All rights reserved., Cold Spring Harbor (NY), 2015).

[245] Varki, A. & Gagneux, P. *Biological Functions of Glycans*, 77–88 (Cold Spring Harbor Laboratory Press Copyright 2015-2017 by The Consortium of Glycobiology Editors, La Jolla, California. All rights reserved., Cold Spring Harbor (NY), 2015).

[246] Endo, T. & Furukawa, K. *Chapter 5 Rheumatoid arthritis and serum IgG*, vol. 30, 277–289 (Elsevier, 1996).

[247] Hakomori, S.-i. *Chapter 4 Tumor-associated carbohydrate antigens and modified blood group antigens*, vol. 30, 243–276 (Elsevier, 1996).

[248] Kobata, A. *Chapter 3 Cancer cells and metastasis: Introduction*, vol. 30, 183 (Elsevier, 1996).

[249] Kobata, A. *Chapter 3c Cancer cells and metastasis: The Warren-Glick phenomenon - a molecular basis of tumorigenesis and metastasis*, vol. 30, 211–227 (Elsevier, 1996).

[250] Kobata, A. *Chapter 3 Cancer cells and metastasis: Concluding remarks*, vol. 30, 241 (Elsevier, 1996).

[251] Matsuda, M. *Chapter 15 Glycosylation defects in blood clotting*, vol. 30, 439–444 (Elsevier, 1996).

[252] Dieckmann-Schuppert, A., Gerold, P. & Schwarz, R. T. *Chapter 2c Glycoproteins of parasites: Glycoproteins of malaria parasites*, vol. 30, 125–158 (Elsevier, 1996).

[253] Hayes, B. K. & Hart, G. W. *Chapter 2a Glycoproteins of parasites: Glycoproteins of Trypanosoma cruzi*, vol. 30, 99–111 (Elsevier, 1996).

[254] Colley, K. J., Varki, A. & Kinoshita, T. *Cellular Organization of Glycosylation*, 41–9 (Cold Spring Harbor Laboratory Press Copyright 2015-2017 by The Consortium of Glycobiology Editors, La Jolla, California. All rights reserved., Cold Spring Harbor (NY), 2015).

[255] Wohlschlager, T. *et al.* Native mass spectrometry combined with enzymatic dissection unravels glycoform heterogeneity of biopharmaceuticals. *Nature Communications* **9**, 1713 (2018).

[256] Yang, Y. *et al.* Hybrid mass spectrometry approaches in glycoprotein analysis and their usage in scoring biosimilarity. *Nature Communications* **7**, 13397 (2016).

[257] Solá, R. J. & Griebenow, K. Glycosylation of therapeutic proteins. *BioDrugs* **24**, 9–21 (2010).

[258] Varki, A., Kannagi, R., Toole, B. & Stanley, P. *Glycosylation Changes in Cancer*, 597–609 (Cold Spring Harbor Laboratory Press Copyright 2015-2017 by The Consortium of Glycobiology Editors, La Jolla, California. All rights reserved., Cold Spring Harbor (NY), 2015).

[259] Dacheux, L. *et al.* Evolutionary dynamics of the glycan shield of thehuman immunodeficiency virus envelope during natural infection andimplications for exposure of the 2g12epitope. *Journal of Virology* **78**, 12625–12637 (2004).

[260] Mulloy, B., Dell, A., Stanley, P. & J, H. P. *Structural Analysis of Glycans*, 639–52 (Cold Spring Harbor Laboratory Press Copyright 2015-2017 by The Consortium of Glycobiology Editors, La Jolla, California. All rights reserved., Cold Spring Harbor (NY), 2015).

[261] Reily, C., Stewart, T. J., Renfrow, M. B. & Novak, J. Glycosylation in health and disease. *Nature Reviews Nephrology* **15**, 346–366 (2019).

[262] Tumolo, T., Angnes, L. & Baptista, M. S. Determination of the refractive index increment (dn/dc) of molecule and macromolecule solutions by surface plasmon resonance. *Analytical Biochemistry* **333**, 273–279 (2004).

[263] Higgins, E. Carbohydrate analysis throughout the development of a protein therapeutic. *Glycoconjugate journal* **27**, 211–225 (2010).

[264] Pohl, G., Kaellstroem, M., Bergsdorf, N., Wallen, P. & Joernvall, H. Tissue plasminogen activator: peptide analyses confirm an indirectly derived amino acid sequence, identify the active site serine residue, establish

glycosylation sites, and localize variant differences. *Biochemistry* **23**, 3701–3707 (1984).

[265] Hotchkiss, A. *et al.* The influence of carbohydrate structure on the clearance of recombinant tissue-type plasminogen activator. *Thromb Haemost* **60**, 255–61 (1988).

[266] Gazi, U. & Martinez-Pomares, L. Influence of the mannose receptor in host immune responses. *Immunobiology* **214**, 554–561 (2009).

[267] Opdenakker, G., Van Damme, J., Bosman, F., Billiau, A. & De Somer, P. Influence of carbohydrate side chains on activity of tissue-type plasminogen activator. *Proceedings of the Society for Experimental Biology and Medicine* **182**, 248–257 (1986).

[268] Houel, S. *et al.* N- and o-glycosylation analysis of etanercept using liquid chromatography and quadrupole time-of-flight mass spectrometry equipped with electron-transfer dissociation functionality. *Analytical Chemistry* **86**, 576–584 (2014).

[269] Martínez, V. P. M. *et al.* Functional analysis of glycosylation in etanercept: Effects over potency and stability. *European Journal of Pharmaceutical Sciences* **153**, 105467 (2020).

[270] Tjondro, H. C. *et al.* Hyper-truncated glycans augment the activity of neutrophil granule myeloperoxidase. *bioRxiv* 2020.07.24.219956 (2020).

[271] McCallum, M., Walls, A. C., Bowen, J. E., Corti, D. & Veesler, D. Structure-guided covalent stabilization of coronavirus spike glycoprotein trimers in the closed conformation. *Nature Structural and Molecular Biology* 942–949 (2020).

[272] Turner, A. J. *Chapter 25 - ACE2 Cell Biology, Regulation, and Physiological Functions*, 185–189 (Academic Press, Boston, 2015).

[273] Yan, R. *et al.* Structural basis for the recognition of sars-cov-2 by full-length human ace2. *Science* **367**, 1444–1448 (2020).

[274] Tikellis, C. & Thomas, M. C. Angiotensin-converting enzyme 2 (ace2) is a key modulator of the renin angiotensin system in health and disease. *International Journal of Peptides* **2012**, 256294 (2012).

[275] Palau, V., Riera, M. & Soler, M. J. Adam17 inhibition may exert a protective effect on covid-19. *Nephrology Dialysis Transplantation* **35**, 1071–1072 (2020).

[276] Lambert, D. W. *et al.* Tumor necrosis factor-alpha convertase (adam17) mediates regulated ectodomain shedding of the severe-acute respiratory syndrome-coronavirus (sars-cov) receptor, angiotensin-converting enzyme-2 (ace2). *Journal of Biological Chemistry* **280**, 30113–30119 (2005).

[277] Wang, K., Gheblawi, M. & Oudit, G. Y. Angiotensin converting enzyme 2. *Circulation* **142**, 426–428 (2020).

[278] Benton, D. J. *et al.* Receptor binding and priming of the spike protein of sars-cov-2 for membrane fusion. *Nature* (2020).

[279] Tang, T., Bidon, M., Jaimes, J. A., Whittaker, G. R. & Daniel, S. Coronavirus membrane fusion mechanism offers a potential target for antiviral development. *Antiviral Research* **178**, 104792 (2020).